

Carnegie Mellon University
Carnegie Institute of Technology

THESIS

Submitted in Partial Fulfillment of the Requirements
For the Degree of Doctor of Philosophy

TITLE

**Development and Experimental Validation
of Mathematical Tools for Computerized
Monitoring of Cryosurgery**

PRESENTED BY

Chandrajit Thaokar

ACCEPTED BY THE DEPARTMENT OF MECHANICAL ENGINEERING

ADVISOR, MAJOR PROFESSOR

DATE

DEPARTMENT HEAD

DATE

APPROVED BY THE COLLEGE COUNCIL

DEAN

DATE

Development and Experimental Validation of Mathematical Tools for Computerized Monitoring of Cryosurgery

PRESENTED BY

Chandrajit Thaokar

THESIS

Submitted to the Department of Mechanical Engineering

In Partial Fulfillment of the Requirements

For the Degree of Doctor of Philosophy

THESIS COMMITTEE

Prof. Yoed Rabin (Chair)

Prof. Jeyanandh Paramesh

Prof. Yongjie Zhang

Prof. Kenji Shimada

Carnegie Mellon University

Pittsburgh, Pennsylvania

Jan 2016

ACKNOWLEDGEMENTS

First and foremost, I would like to express my deepest gratitude for my research advisor, Professor Yoed Rabin, for providing me the opportunity to pursue a Ph.D. I hold his continual guidance, his immense patience and the support he has given over the course of my studies in the highest regard. I hope I can emulate his work ethic and dedication going forward in my career.

I would also like to thank the other members of my thesis committee, Professors Yongjie Zhang, Kenji Shimada and Jeyanandh Paramesh, for the constructive suggestions and comments they have given me throughout the course of my research. I am very grateful to Dr. Michael Rossi for allowing me to make use of the exceptional experimental data produced during his thesis. I would like thank Mr. Ahmad Khairi for collaborating with me during the course of my experimental studies.

I would also like to thank the National Institute of Biomedical Imaging and Bioengineering for their generous financial support to the project.

I would like to express my gratitude to the many colleagues who I have had the pleasure to work with over the years: Dr. David Eisenberg, Dr. Robert Keelan, Dr. Justin Feig, Dr. Anjali Sehrawat, Chris Lin, Lili Ehrlich. In addition, I very grateful to the many staff members in the Mechanical Engineering department, especially Chris Hertz. He goes above and beyond call of duty to help the students in the department. He has your back every single time.

I wish to thank the many friends I have made at CMU over the course my graduate studies. I would especially like to thank Kyle Justus, Lauren Finkenauer and Rakesh Khilwani for their heartfelt support. I would like to thank Abhijeet Tirthgirikar, Sarang Dalne and Nikhil Kavadia for helping me out so I could concentrate on my research.

I want convey my heartfelt thanks to my partner, Bethanne Tucker, who has been there for me through all the ups and downs in research as well as life. I would not have finished my thesis without her constant support and encouragement.

Finally and most importantly, I'd like to thank my family for the immense sacrifices they made so that I could follow my dreams. My mother (Asmita), my father (Vivek) and my sister (Arti) have made me the person I am today. Words fall short to express my gratitude towards the sacrifices made by my parents for this thesis. I can only hope that I can repay their faith in my abilities.

This thesis is dedicated to my parents, Asmita and Vivek Thaokar. Thanks Mom and Dad.

ABSTRACT

Cryosurgery is the destruction of undesired biological tissues by freezing. Modern cryosurgery is frequently performed as a minimally-invasive procedure, where multiple hypodermic, needle-shaped cryoprobes are inserted into the target area to be treated. The aim of the cryosurgeon is to maximize cryoinjury within a target region, while minimizing damage to healthy surrounding tissues. There is an undisputed need for temperature-field reconstruction during minimally invasive cryosurgery to help the cryosurgeon achieve this aim.

The work presented in this thesis is a part of ongoing project at the Biothermal Technology Laboratory (BTTL), to develop hardware and software tools to accomplish real-time temperature field reconstruction. The goal in this project is two-fold: (i) to develop the hardware necessary for miniature, wireless, implantable temperature sensors, and (ii) to develop mathematical techniques for temperature-field reconstruction in real time, which is the focus of the work presented in this thesis. To accomplish this goal, this study proposes a computational approach for real-time temperature-field reconstruction, combining data obtained from various sensing modalities such as medical imaging, cryoprobe-embedded sensors, and miniature, wireless, implantable sensors. In practice, the proposed approach aims at solving the inverse bioheat transfer problem during cryosurgery, where spatially distributed input data is used to reconstruct the temperature field.

Three numerical methods have been developed and are evaluated in the scope of this thesis. The first is based on a quasi-steady approximation of the transient temperature field, which has been termed Temperature Field Reconstruction Method (TFRM). The second method is based on analogy between the fields of temperature and electrical potential, and is thus termed Potential Field Analogy Method (PFAM). The third method is essentially a hybrid of TFRM and PFAM, which has shown superior results. Each of these methods has been benchmarked against a full-scale finite elements analysis using the commercial code ANSYS. Benchmarking results display an average mismatch of less than 2 mm in 2D cases and less than 3 mm in 3D cases for the location of the clinically significance isotherms of -22°C and -45°C .

In an advanced stage of numerical methods evaluation, they have been validated against experimental data, previously obtained at the BTTL. Those experiments were conducted on a gelatin solution, using proprietary liquid-nitrogen cryoprobes and a cryoheater to simulate urethral warming. The design of the experiment was aimed at creating a 2D heat-transfer

problem. Validation results against experimental data suggest an average mismatch of less than 2 mm, for the hybrid of TFRM + PFAM method, which is of the order of uncertainty in estimating the freezing front location based on ultrasound imaging.

TABLE OF CONTENTS

Chapter 1: Introduction	1
1.1 History of Cryosurgery	1
1.2 Modern Prostate Cryosurgery	2
1.3 Need for Reconstruction of Temperature Field during Cryosurgery	5
1.4 Inverse Heat Transfer Problems	7
1.5 Research Objectives	9
 Chapter 2: Temperature Field Reconstruction Method (TFRM) in 2D During Cryosurgery	 10
2.1 Mathematical Formulation	10
2.2 Quasi-Steady Approximation	11
2.3 Numerical Solution	12
2.4 Results and Discussion	14
2.5 Summary	26
 Chapter 3: Potential Field Analogy Method (PFAM), Hybrid (PFAM + TFRM) and Experimental Validation in 2D	 27
3.1 Mathematical Formulation	27
3.1.1 <i>A new potential field analogy method (PFAM)</i>	27
3.1.2 <i>Application of a temperature-field reconstruction method (TFRM)</i>	29
3.1.3 <i>Integration of PFAM with TFRM</i>	32
3.2 Experimental Verification	33
3.2.1 <i>Experimental setup</i>	33
3.2.2 <i>Simulating ultrasound imaging from experimental data</i>	35
3.2.3 <i>Comparison approach of numerical results with experimental data</i>	35
3.3 Results and Discussion	36
3.3.1 <i>Experimental validation of PFAM</i>	36

3.3.2 Computer validation of the integrated PFAM+TFRM method	41
3.3.3 Experimental validation of the thermal history of the PFAM + TFRM method	44
3.4 Summary	45
Chapter 4: Extending the Hybrid (PFAM + TFRM) method to 3D	47
4.1 Problem Definition and 3D Implementation	47
4.2 Results and Discussion	49
4.2.1 Temperature Field Reconstruction Method (TFRM) in 3 Dimensions.....	49
4.2.2 Unified Application of Potential Field Analogy Method (PFAM) and Temperature Field Reconstruction Method (TFRM) in 3 Dimensions	61
4.3 Summary	64
Chapter 5: Characterization of a CMOS sensing core for ultra-miniature wireless implantable temperature sensors.....	67
5.1 Principles of sensor design and implementation.....	67
5.2 Experimental setup	69
5.3 Thermal design considerations of the experimental setup.....	70
5.4 Results and Discussion	71
5.5 Summary	72
Chapter 6: Summary and Conclusions	73
Chapter 7: Proposed Future Work	77
7.1 Porting MATLAB code to C/C++	77
7.2 Ultrasound Imaging	77
7.3 Optimization of Potential Field Analogy Method	78
7.4 Experimental Validation in 3D	78
7.4 Sensor Placement Strategies	79

LIST OF FIGURES

Figure 1.1: Schematic illustration of minimally-invasive prostate cryosurgery using Joule Thompson based cryoprobes.....	3
Figure 2.1: Flowchart illustrating the framework to validate the numerical methods developed in the current study. Solution validation is performed in by comparing the reconstructed temperature field (the solution to the simplified, inverse heat transfer problem) and the benchmark (the full-scale solution to the ordinary heat transfer problem).....	15
Figure 2.2: Temperature field regions resulted from the transient solution of Case A (the benchmark) at the point of optimal match between the freezing-front location and the prostate contour; cryoprobes are illustrated with white dots.	17
Figure 2.3: Temperature field regions for Case I: complete freezing front information from medical imaging (Case B) with no temperature sensors; cryoprobes are illustrated with white dots.....	19
Figure 2.4: Temperature fields difference, ΔT , between the benchmark solution and the solution for Case I: complete freezing front information (Case B) with no temperature sensors; cryoprobes are illustrated with black dots.....	19
Figure 2.5: Temperature fields difference, ΔT , between the benchmark solution and the solution for Case II: complete freezing front information (Case B) with six sensors implanted along the -22°C isotherm at the locations of maximum temperature difference in Fig. 2.4; cryoprobes are illustrated with black dots and sensors with white “x”	20
Figure 2.6: Temperature field regions for Case III: partial freezing front information obtained from a trans-rectal ultrasound transducer (Case C), combined with six sensors implanted along the -22°C isotherm, and six additional sensors equally distributed along the unobservable portion of the prostate contour (upper portion of the figure); α is the field of view of the trans-rectal ultrasound transducer; cryoprobes are illustrated with white dots and sensors with white “x”	21
Figure 2.7: Temperature fields difference, ΔT , between the benchmark solution and the solution for Case III: partial freezing front information obtained from a trans-rectal	

ultrasound transducer (Case C) combined with six sensors implanted along the -22°C isotherm, and six additional sensors equally distributed along the unobservable portion of the prostate contour (upper portion of the figure); cryoprobes are illustrated with black dots and sensors with white “x”	22
Figure 2.8: Temperature field reconstruction for Case IV (Case D—solely based on temperature sensors with no imaging data): twelve sensors equally distributed along the -22°C isotherm; cryoprobes are illustrated with white dots and sensors with white “x”	23
Figure 2.9: Mismatch in the areas bounded by the lethal isotherm, ΔA_{lethal} , between the benchmark (Case A) and the Case B, where complete freezing-front data is available from medical imaging, and the temperature sensor are equally distributed along predicted isotherms.	24
Figure 2.10: Mismatch in the areas bounded by the lethal isotherm, ΔA_{lethal} , between the benchmark (Case A) and the case of partial freezing-front data available from medical imaging (Case C), where the temperature sensors are equally distributed along the freezing front, and combined with temperature sensors distributed along the -22°C and -45°C isotherms.....	25
Figure 2.11: Mismatch in the area bounded by the lethal isotherm, ΔA_{lethal} , between the benchmark (Case A) and the case where no imaging data is available for the purpose of extracting the location of the freezing front (Case D), where temperature sensors are equally distributed along the -22°C and -45°C isotherms.	25
Figure 3.1: Schematic illustration of a representative cross section during prostate cryosurgery displaying: (a) the ultrasound transducer, the freezing front, and the urethral warmer; and (b) the acoustic shadow by the frozen region and the partially visible freezing front on the ultrasound (US) monitor.....	28
Figure 3.2: Integration of PFAM and TFRM for the purpose of (I) freezing front estimation in the invisible area of the US image, and (II) thermal history evaluation	32
Figure 3.3: A representative snapshot from a video recording of a simulated cryosurgery procedure, where the medium is distilled water mixed with 1.3% gelatin and blue food dye. The reconstructed frozen region is shown on the top-right corner of the image, which is the basis for the displayed freezing front contour in Fig. 3.1	34

Figure 3.4: Comparison between PFAM estimation for the 0°C isotherm (green curve) and freezing-front reconstruction from experimental results (blue curve) for Case A, where the PFAM results are only presented within the simulated acoustic shadow area (Fig. 4(a) is also presented in Figs. 3.1 and 3.3).	37
Figure 3.5: Comparison between PFAM estimation for the 0°C isotherm (green curve) and freezing-front reconstruction from experimental results (blue curve) for Case B, where the PFAM results are only presented within the simulated acoustic shadow area. TC ₁ and TC ₂ are thermocouples embedded in the freezing medium and used to validate the integration of PFAM and TFRM method in the context of Fig. 3.9	38
Figure 3.6: Comparison between PFAM estimation for the 0°C isotherm (green curve) and freezing-front reconstruction from experimental results (blue curve) for Case C, where the PFAM results are only presented within the simulated acoustic shadow area.	39
Figure 3.7: Comparison of a benchmark generated with finite-elements analysis (ANSYS) and the estimated location of the freezing front (0°C isotherm) using TFRM, with and without integration with PFAM (Case D in Table 3.2).	42
Figure 3.8: Comparison of a benchmark generated with finite-elements analysis (ANSYS) and the estimated location of the lethal-temperature isotherm, -45°C using TFRM, with and without integration with PFAM (Case D in Table 3.2).	43
Figure 3.9: Comparison of measured and estimated temperatures, using an integrated PFAM and TFRM method, where sensor locations are illustrated in Fig. 3.5.	45
Figure 4.1: Top view and front view of a representative numerical model of the prostate (gray) and volume of tissue (green) below lethal temperature (-45°C).	47
Figure 4.2: A schematic of full scale transient simulation used as a benchmark at a representative (t = 180 seconds) time interval along with observed cross sections (yellow curves).	50
Figure 4.3: Comparison between TFRM estimation and the benchmark (blue) for the -45°C isotherm for Case A when n = 30 (green), n = 15 (cyan), n = 8 (red), n = 4 (black), and n = 1 (magenta) at t = 180 s	52

Figure 4.4: Comparison between TFRM estimation and the benchmark (blue) for the -22°C isotherm for Case A when $n = 30$ (green), $n = 15$ (cyan), $n = 8$ (red), $n = 4$ (black), and $n = 1$ (magenta) at $t = 180$ s	53
Figure 4.5: Comparison between TFRM estimation for the -45°C isotherm and benchmark results for various number of cross-section datasets after 180 seconds of simulation.....	54
Figure 4.6: Comparison between TFRM estimation for the -45°C isotherm and benchmark (blue) for different number of cross-sections observed, n , after 240 seconds of simulation.....	55
Figure 4.7: Comparison between TFRM estimation for the -45°C isotherm and benchmark (blue) for different number of cross-sections observed, n , after 300 seconds of simulation.....	55
Figure 4.8: Maximum mismatch, ΔS_{\max} , between TFRM and benchmark lethal isotherm as a function of number of sampled cross-section, in a case where the entire freezing front location in the cross section is known.....	56
Figure 4.9: Average mismatch, ΔS_{avg} , between TFRM and benchmark lethal isotherm as a function of number of observed (sampled) cross-section, n , when entire freezing front location is assumed to be visible.....	57
Figure 4.10: Comparison between TFRM estimation for the -45°C isotherm and benchmark (blue) for different number of cross-sections observed, n , after 180 seconds of simulation when acoustic shadowing is taken in to account (Case B)	58
Figure 4.11: Comparison between TFRM estimation for the -45°C isotherm and benchmark (blue) for different number of cross-sections observed, n , after 240 seconds of simulation when acoustic shadowing is taken in to account (Case B)	58
Figure 4.12: Comparison between TFRM estimation for the -45°C isotherm and benchmark (blue) for different number of cross-sections observed, n , after 300 seconds of simulation when acoustic shadowing is taken in to account (Case B)	59
Figure 4.13: Maximum mismatch, ΔS_{\max} , between TFRM and benchmark lethal isotherm as a function of number of observed (sampled) cross-section, n , when only partial information about the location of freezing front in known. (Case B)	59

Figure 4.14: Average mismatch, ΔS_{avg} , between TFRM and benchmark lethal isotherm as a function of number of observed (sampled) cross-section, n , when only partial information about the location of freezing front is known(Case B).....	60
Figure 4.15: Comparison between the unified computation framework of TFRM+PFAM and the benchmark solution for the location of the -45°C isotherm, for the various cases after 180 seconds of cryosurgery simulation at a depth of 35 mm.....	61
Figure 4.16: Comparison between TFRM + PFAM estimation for the -45°C isotherm and benchmark (blue) for different number of cross-sections observed, n , combined with case A, case B, and case C after 240 seconds of simulation.....	62
Figure 4.17: Comparison between TFRM + PFAM estimation for the -45°C isotherm and benchmark (blue) for different number of cross-sections observed, n , combined with case A, case B, and case C after 300 seconds of simulation.....	62
Figure 4.18: Representative illustration of 3D freezing front reconstruction based on known freezing front location on a single plane, which could be obtained from medical imaging. Input data is considered for this problem as follows: (1) the green line represents the freezing front reconstructed from medical imaging, (2) the thermal history at the tip of the cryoprobes is known from the cryodevices, and (3) the temperature t the urethra (red) is given by the urethral warmer. The reconstructed freezing front by means of the proposed unified numerical technique is presented in violet. The quality of reconstruction is summarized in Table 4.3 and 4.4 for a variety of cases.....	64
Figure 5.1: Schematic illustration of the proposed proportional-to-absolute-temperature (PTAT) sensing core.....	68
Figure 5.2: Photograph of the fabricated sensor chip (a) and the packaged chip mounted on PCB (b)	69
Figure 5.3: Experimental setup: (a) a schematic illustration of the system, and (b) a photograph of the experimental stage.....	70
Figure 5.4: Results obtained from three representative chips in a self-biased mode (#1 and #2) and an externally biased mode (#2): (a) temperature data as a function of voltage output, and (b) average nonlinear offset, calculated as the temperature difference	

between the experimental data shown (a) and a linear curve connecting the boundary temperature values for each dataset	71
Figure 7.1: The figure shows an ultrasound snapshot of tissue before and after onset of freezing	78

LIST OF TABLES

Table 2.1: Representative thermophysical properties of soft biological tissue used in the current study.....	13
Table 2.2: A summary of five general cases explored in the current study, where Case A is a benchmark, and the location of the target isotherms for sensors placement is extracted from computerized planning of cryosurgery. Imaging of freezing front location is simulative of MRI, CT (complete contours), or ultrasound (a partial contour). The thermal history of the benchmark is used to simulate extraction of the freezing front location from medical imaging and temperature data obtained from implantable sensors.	16
Table 3.1: Representative thermophysical properties of soft biological tissue used in the current study.....	28
Table 3.2: Summary of freezing front mismatch between the PFAM, TFRM, and experimental results.	40
Table 4.1: Summary of average mismatch (ΔS_{avg}) and max mismatch (ΔS_{max}) between benchmark and TFRM predicted -45°C and -22°C isotherm at $t = 180$ s.....	51
Table 4.2: Summary of mismatch between the PFAM, TFRM for lethal isotherm (-45°C).....	63
Table 4.3: Summary of mismatch between the PFAM, TFRM for -22°C isotherm	65

Chapter1: Introduction

The work presented in this thesis aims at the development and validation of mathematical techniques for the purpose of real-time monitoring of the temperature field during minimally invasive cryosurgery. In this chapter, an overview of cryosurgery is presented, including a short history of cryosurgical procedures and an explanation of modern prostate cryosurgery. In addition, an introduction to temperature field reconstruction is presented, along with the objectives for this thesis.

1.1 History of Cryosurgery

Cryosurgery is the destruction of undesirable biological tissue by freezing. The benefits of applying cold temperatures to tissue for the treatment of injuries and inflammation have been known for a long time. However, the technique of freezing tissue to induce necrosis has relatively modern origins, with the first reported cases within the last century. An overview of the recent history of cryosurgery is presented below, including its origins in the mid 19th century up through the modern era starting in the 1960s.

The first documented uses of cryosurgery are from the mid 19th century, when a physician by the name of James Arnott [1] published reports describing the freezing of cervical and skin cancers. Towards the end of the 19th century, technological advancements allowed for the compression, liquefaction, and storage of atmospheric gases [2]. These newly available cryogens were used mainly for topical ailments to different degrees [3, 4]. Starting in the late 1930s, some clinicians began pioneering work on cryosurgical techniques for treating deep-tissue malignancies [5]. In the late 1940s and the 1950s, several experiments were performed which laid the foundation for many modern cryosurgical applications.

Cryosurgery was introduced as an invasive procedure for the first time in 1961, with the development of the cryoprobe by Cooper and Lee [6]. In 1961, they introduced a cryosurgical apparatus for producing lesions in the brain, which delivered liquid nitrogen from a pressurized source to a vacuum-insulated cryosurgical probe (cryoprobe). The cryoprobe itself was made of three concentric tubes, where the inner tube carried liquid nitrogen to the tip of the probe and the space between the inner and middle tubes served as a path to return the gaseous-nitrogen exhaust. The space between the middle and outer tubes was vacuum-insulated, so as to ensure that the freezing effect of the probe was localized along its active length (the un-insulated tip of

the probe). This new design provided surgeons with unequalled cooling power and control. In the 1970s and 1980s, a significant decline was seen cryosurgical research and applications. Most of the techniques developed in the 1960s were falling out of favor because of lack of precision associated with deep tissue cryosurgery.

The early 1990s marked a period of renewed interest in cryosurgery, as technological advancements helped improve the precision with which many cryosurgical techniques could be performed. The development of intraoperative ultrasound, as described by Onik *et al.* [7, 8], facilitates real-time monitoring of freezing tissue during invasive cryosurgical procedures, such as in cryosurgery of the liver and prostate. In addition, new vacuum-insulated cryoprobes designs were introduced, featuring smaller diameters and the use of super-cooled liquid nitrogen (-200 °C) [9, 10].

1.2 Modern Prostate Cryosurgery

Prostate cancer is the most frequently diagnosed cancer in men, as well the second leading cause of cancer-related deaths in men. In 2007, the American Cancer Society estimated that 219,000 new cases were diagnosed, in addition to 27,000 cases resulting in death. About one out of every six American men will develop prostate cancer at some time during his life.

A schematic illustration of a modern prostate cryosurgical procedure [11] is shown in Fig. 1.1. To obtain a clear view of the perineum, the patient is placed in a dorsal lithotomy position. Next, a Foley catheter is inserted into the urethra of the patient to distend the bladder. Note that the bladder is kept full during the procedure, to allow for better transrectal ultrasonography and to help keep healthy tissue away from the freezing zone [12]. The surgeon then inserts a transrectal ultrasound (TRUS) probe, to obtain images of the prostate and surrounding organs [13]. In addition, a probe-placement template (similar in design to ones used for brachytherapy [14]) is fixed against the perineum of the patient. The template consists of holes that are 5 mm apart, which correspond to an aiming grid, projected onto the ultrasound image display.

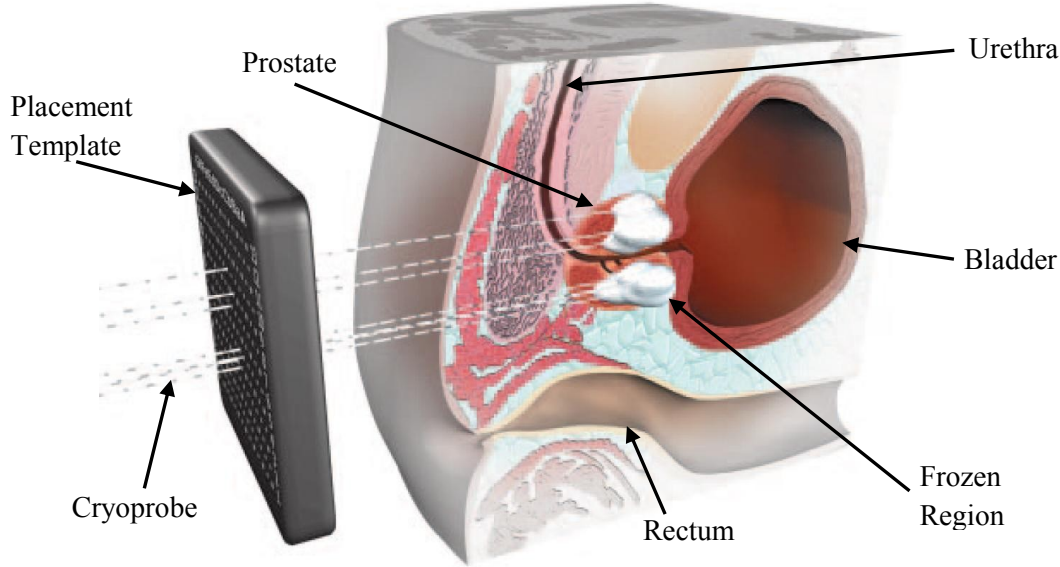


Figure 1.1: Schematic illustration of minimally-invasive prostate cryosurgery using Joule-Thompson effect-based cryoprobes [15].

Once the template is in place, the surgeon uses TRUS guidance to insert multiple, minimally-invasive cryoprobes into the perineum of the patient. The cryoprobes, which are in the shape of long hypodermic needles, are typically cooled using the Joule-Thompson effect, which is the result of the sudden relief of a pressurized gas (most modern cryoablation systems use compressed argon). The cooling effect is localized near the tip of the cryoprobe, and cryosurgeons are able to adjust the rate of cooling for individual probes via supply pressure controls. A wide variety of cryoprobe designs are currently available, and it is up to the clinician to decide what cryoprobe diameter and active length are best for a given prostate gland. Cryoprobes with diameters as small as 1.5 mm and active lengths as long as 40 mm have become commercially available (Oncura, Inc., IL). While it is rare that more than 14 cryoprobes are used, modern cryoablation systems can simultaneously operate as many as 25 cryoprobes (SeedNet®, Oncura, Inc., IL).

In addition to the cryoprobes, as many as five thermocouples (with similar shape to the cryoprobes) may be inserted into the prostate and surrounding tissue. Cryosurgeons use the temperature readings from the thermocouples during the procedure to ensure that the prostate

gland is cooled to a desired target temperature, while critical surrounding tissues and organs are uninjured. The number of thermocouples used depends upon the experience of the cryosurgeon.

In order to prevent freezing damage to the patient's urethra, the Foley catheter is replaced with a urethral warming catheter (a counter-flow heat-exchanger) [16]. A warm (~43 °C) saline solution is continuously circulated through catheter, which extends into the bladder, Fig. 1.1. The urethral warmer has been demonstrated to significantly reduce post-surgical complications associated with damage to the urethra [17, 18].

Once the probes, thermocouples, and warmer are in place, the clinician begins the freezing process. The probes in the anterior (top) region of the prostate are typically turned on first, since ultrasound signals do not penetrate frozen tissue. On the ultrasound display, frozen tissue appears as a dark region (shadowing), with a bright line at the leading edge of the frozen region (freezing front). The surgeon continues towards the posterior end of the prostate, receiving constant, real-time feedback from the ultrasound display and thermocouple readings. Due to the shadowing effect of the frozen region in the posterior portion of the prostate, the anterior freezing front cannot be monitored as the procedure continues. Therefore, the quality of the match between the edge of the target region and the freezing front in the anterior portion of the prostate is highly dependent upon the skill and experience of the surgeon. Note that while other imaging techniques such as magnetic resonance imaging [19, 20] and computerized tomography [21] could be used to better show the full extent of the frozen region, ultrasound imaging remains the preferred technique, primarily due to low cost and availability [22].

The duration of the freezing process is typically about ten minutes, and depends upon the size of the prostate, the number and type of probes used, and the technique of the surgeon. Upon completion of freezing, the surgeon allows for the prostate to thaw (passive thawing typically takes 15 to 20 minutes). Many modern Joule-Thompson cryoablation systems allow for active thawing (using compressed helium gas), which can reduce the thawing duration by about 50%. Following thawing, a second freeze-thaw cycle is typically performed, in order to increase the efficacy of the treatment (some physicians may use a third as well). Depending on the shape of the prostate and the active length of the cryoprobes, clinicians may use the "pullback" technique. For these cases, the clinician first freezes the portion of the prostate closer to the bladder and then pulls back some or all of the cryoprobes to better conform to the apex of the prostate. Due to

the cone-like shape of the prostate gland, it is common that fewer cryoprobes will be operated in the second stage of a pullback procedure.

1.3 Need for Reconstruction of Temperature Field during Cryosurgery

Since the introduction of ultrasound-guided cryosurgery in the mid-1980s, significant developments have been made in cryosurgical equipment and techniques [23]. These advancements have provided clinicians with vastly improved control over the shape and size of the frozen region, and have enabled significant reductions in post-surgical complications. However, the minimally invasive nature of the clinical procedure still poses many technical difficulties, some of which can be alleviated by means of computational tools. Those difficulties can be conveniently classified as being related to either surgical planning (how to shape the frozen region and restrict the destructive freezing effect to the target area) [13, 22] or real-time monitoring (how to correlate the developing thermal field with established criteria for cryosurgery success) [24, 25, 26, 27]. With these technical difficulties in mind, cryosurgery success is highly dependent on the skill and personal experience of the clinician. The tissue undergoing cryosurgery is monitored at present using following modalities: a) measurement of temperature at distinct locations inside the tissue during cryosurgery, b) ultrasound imaging of the tissue during the cryosurgery.

While the benefits of temperature measurements during cryosurgery are well documented and highly recommended in the literature [28, 29, 30, 11, 22, 31, 32, 33, 34], and modern cryodevice setups often offer the feature of real-time temperature sensing, temperature sensors are often not integrated into the procedure for various reasons. At the current state of cryosurgery technology, two principle means have been developed for temperature sensing as a means of monitoring and control, the cryoprobe-embedded sensor and the so-called “needle sensor”. The cryoprobe-embedded sensor approach is as old as the first invasive cryoprobe, but with a diminishing use in recent years. It is the cooling capability and not the temperature that is often controlled in modern cryoprobe. For example, the surgeon would control the flow rate of the cryogen in order to control the rate of propagation of the freezing front, all in effort to match its final location with a predetermined contour (the organ contour for example). Here, a higher flow rate in a nearby cryoprobe will drive the freezing front propagation faster, and the entire process is performed in a trial-and-error fashion, while the freezing front contour is monitored by means

of medical imaging. This mode of operation, combined with the everlasting effort to miniaturize cryoprobes, has led to abandoning temperature sensors in some modern cryoprobes altogether.

An example for the use of needle temperature sensors in cryosurgery is the placement of one or two such sensors near the rectal wall, as feedback to prevent freezing injury to it—one of the most severe complications in prostate cryosurgery [22, 32, 33]. The needle sensor is frequently a hypodermic needle in a diameter similar to that of the minimally invasive cryoprobe. The thermocouple is often the choice of practice as the measuring principle for hypodermic sensors. When incorporated, the needle sensor and the cryoprobe are localized using a similar methodology in prostate cryosurgery—inserting either into a predetermined depth through an x - y grid, which is aligned with the organ but placed outside of the body. Unfortunately, despite its advantages as a safety measure, and despite the capability of modern cryosurgical devices to integrate such temperature sensors, the needle sensor is not frequently used in cryosurgery in recent years.

On the other hand, the primary challenge with ultrasound imaging for cryosurgery is its wave reflection from solid surfaces, such as the cryoprobe shell and the freezing front. As a consequence, the frozen region appears opaque on the ultrasound monitor, while acoustic shadowing is formed behind the frozen region [26]. Using Trans-Rectal Ultrasound Transducer (TRUST), the freezing front next to the rectal wall can be clearly observed during prostate cryosurgery, but no imaging information may be obtained about the remaining portion of the freezing front. This lack of information may affect the quality of the medical treatment and lead to post-operational complications.

While the freezing front location is the controlled parameter during clinical practice, with the onset of freezing around 0°C , clinical interest extends to lower temperatures as well. It is widely accepted that a lethal temperature threshold must be surpassed in order to maximize cryoinjury, with a commonly assumed value typically in the range of -40°C and -50°C [27]. Since temperature measurements during prostate cryosurgery are rarely done (at one or a couple of locations, if at all), the location of the lethal temperature during clinical practice represents a speculation at best. The current study is further aimed at improving the prediction of the location of the lethal-temperature isotherm. The improved predictions for the location of lethal isotherm would increase the quality of outcomes of the cryosurgical procedures.

1.4 Inverse Heat Transfer Problems

Inverse Heat Transfer Problems (IHTP) represent a class problems where the thermal outcome is known, possibly in the form of a thermal history at a pre-specified location in the domain, and the challenge is to find the driving thermal process that would result in such an outcome. For example, Rabin and Shitzer have searched for a thermal history at a cryoprobe that would lead to a constant cooling rate at the freezing front [35, 36]. There, the cooling rate at the moving freezing front is the pre-specified condition, and the solution is the thermal history in the entire domain, and the problem is known as an inverse-Stefan problem (characterized by a small Stefan number as discussed in the context of Chapter 2).

Mathematically, inverse heat transfer problems may be referred to as ill-posed problems, where a solution to the problem is not unique (a number of valid solutions may exist). The concept of a well-posed problem, originally introduced by Hadamard [37], requires that its solution should satisfy the following three conditions: (1) the solution must exist; (2) the solution must be unique; and (3) the solution must be stable under small changes to the input data (the so-called stability condition).

The existence of a solution for an inverse heat transfer problem may be assured by physical reasoning. For example, if there is a change in the values of the measured temperature in a transient problem, there exists a causal characteristic, say, a boundary heat flux, to be estimated. On the other hand, the uniqueness of the solution of inverse problems can be mathematically proved only for some special cases [38]. Also, the inverse problem may be very sensitive to random errors in the measured input data, thus requiring special techniques for its solution in order to satisfy the stability condition. A successful solution of an inverse problem generally involves its reformulation as an approximated, well-posed problem. Frequently, the solution of inverse heat transfer problems are obtained in the least squares sense [39].

Conceptually, the work presented in this thesis focuses on formulating cryosurgery as an IHTP. However, dimensional analysis (presented in Chapter 2) for the effects dominating the heat transfer problem modeling cryosurgery, suggests that the ill-posed inverse problem can be approximated by a well-posed quasi-steady problem. This approximation is supported by the small Stefan numbers, which indicates that latent heat effects dominate the problem, rather than thermal inertia effects. The quasi-steady problem is associated with a unique solution.

The input data for the current study may include measurements from three potential sources available during cryoprocurement [22]: (a) temperature data collected at the tip of the cryoprobe, (b) temperature sensors embedded in the cryotreated region, and (c) ultrasound imaging. The solution to the problem is the temperature field that would result in those data measurements. Next, the temperature field is further analyzed to extract the freezing front location and the location of other isotherms of clinical significance.

Normally, cryoprobes used during cryosurgery have a thermocouple embedded in them [22, 15]. However, with the continuous trend to miniaturize cryoprobes, a tendency to abandon internal sensors to the cryoprobes emerges. The second potential source of information inside the targeted tissue during cryosurgery is the use of temperature sensors. Hypodermic thermocouples are the most commonly used temperature sensing device during cryosurgery [22]. However, as the number of cryoprobes used during the surgery has increased, number of thermocouples used has decreased and is sometimes completely abandoned. The clinicians can also use Resistance Temperature Detector (RTD) [40] or Thermistors [41] during the procedure. A new category of sensors--wireless miniature temperature sensors--is been presented in this thesis [42].

The extent of freezing during cryosurgery may be monitored using various medical imaging modalities such as Magnetic Resonance Imaging (MRI) [20], X-ray Computed Tomography (CT) [43] or Ultrasound (US) imaging. Out of those, US imaging is the most commonly utilized imaging technique for prostate cryosurgery—the model used for numerical techniques developments in the current study. Unfortunately, US imaging comes with technical hurdles associated with acoustic shadowing [22]. The numerical methods proposed in this thesis are able to achieve temperature-field reconstruction by using either complete freezing front location as an input (as would be the case for MRI), or partial freezing front for the same purpose (as would be the case for ultrasound imaging).

For a portion of the analysis presented in this study, it is assumed that the freezing front can be extracted in real time from medical imaging, which may not be the case to date. However, the technical difficulties associated with real-time freezing front reconstruction are not considered as major challenges, while the analysis results displayed in this study suggest that related technology developments maybe warranted.

1.5 Research Objectives

The goal of this research is to develop efficient and computationally inexpensive tools for real-time monitoring of cryosurgery, by reconstructing the temperature field in the targeted region during surgical operation. The following objectives have been set towards that goal:

1. To develop Temperature-Field Reconstruction Method (TFRM) in 2D during cryosurgery (Chapter 2). This efficient numerical method used input data from implantable temperature sensors and medical imaging.
2. To investigate effects of temperature sensors placement on the quality of the reconstructed 2D temperature field (Chapter 2).
3. To develop Potential Field Analogy Method (PFAM) for estimating the extent of freezing in acoustic shadow region during cryosurgery. PFAM was combined with TFRM developed for Objective 1 and the outcome of hybrid TFRM + PFAM is demonstrated in 2D.
4. To experimentally verify the hybrid technique developed in response to Objective 3 (Chapter 3). Relevant experimental data was developed in previous studies.
5. To develop the hybrid (TFRM + PFAM) for 3D prostate cryosurgery (Chapter 4).
6. To develop and experimental apparatus in order to characterize the CMOS-based sensing cores required for ultra-miniature, wireless temperature sensors (Chapter 5). This represents a collaborative effort, where sensing-core development was led by Mr. Ahmad Khairi under the supervision of Prof. Jeyanandh Paramesh, while thermal design, analysis, and experimental apparatus fabrication, are the original contributions in the current study (Chapter 5).

Chapter 2: Temperature Field Reconstruction Method (TFRM) in 2D During Cryosurgery

The objective of the study presented in this chapter is to develop a new numerical method to reconstruct the temperature field within the cryotreated region in real time, which integrates temperature data from embedded sensors with ultrasound imaging data. For the developed method, this study further includes a sensitivity analysis of the sensors layout on the quality of strategically selected temperature isotherms.

2.1 Mathematical Formulation

It is customary to assume that heat transfer during cryosurgery can be modeled with the classical bioheat equation [44]:

$$C \frac{\partial T}{\partial t} = \nabla \cdot (k \nabla T) + w_b C_b (T_b - T) + q_{met} \quad (2.1)$$

where C is the volumetric specific heat of the tissue, T is the temperature, t is the time, k is the thermal conductivity of the tissue, w_b is the blood perfusion rate, C_b is the volumetric specific heat of the blood, T_b is the blood temperature entering the thermally treated area (typically the normal body temperature), and q_{met} is the metabolic heat generation.

The physical properties used for the current study are listed in Table 1. It is assumed in the current study that the specific heat is an effective property [45] within the phase-transition temperature range of -22°C to 0°C (the tissue is first-order approximated as an NaCl solution), where a detailed discussion about the application of the effective specific heat to phase change problems is given in [7]. The metabolic heat generation is typically negligible compared to the heating effect of blood perfusion [46], and is neglected in this study. While more advanced models of bioheat transfer are available in the literature [47, 48], it is assumed in the current study that they would not guarantee greater accuracy in the cryosurgery simulation but will involve greater mathematical complications.

The blood perfusion rate in the unfrozen region (Table 2.1) and the step-like change in the blood-perfusion rate upon the onset of freezing represent the worst-case scenario in terms of transient effects. In practice, one would expect a gradual decay in blood flow with the decreasing temperature, potentially leading to a complete stasis before the freezing temperature is achieved. To the best of knowledge of the authors, the actual temperature dependency of blood perfusion in the prostate is unknown. The uncertainty in blood perfusion rate may contribute a few percent to the uncertainty in predicting the freezing front location [46]; this uncertainty is not taken into

account in the current study. A detailed discussion on the propagation of uncertainty in measurements into heat transfer simulations of cryosurgery is given in [49].

2.2 Quasi-Steady Approximation

At least two principal approaches are available in effort to provide the clinician with feedback on the developing temperature field: (i) prediction-based, by applying a real-time simulation of the procedure, and (ii) reconstruction-based, using measured data at multiple locations. In the first approach, the bioheat transfer process is simulated using Eq. (1), while temperature data obtained from the cryoprobes is used as internal boundary conditions.

The real-time simulation process is typically computationally very expensive [50, 51] and rarely is it practical as a real-time feedback. While available data from implantable sensors can be used to verify the quality of a real-time simulation, such data cannot be straightforwardly implemented to correct the simulated temperature field once a deviation between predicted and measured values is observed. Since temperature sensors do not drive any thermal effect, merely correcting a predicted temperature field to specific values at the sensor locations has no physical meaning. More appropriately, this deviation can be used to correct the model properties (i.e., thermophysical properties) by employing a parametric estimation procedure [52], after which a computer simulation can be attempted again in an effort to get a better match between computer results and experimental data. This prediction-correction process of model properties using a full-scale simulation, data measurements, and parametric estimation could continue until the convergence of property values takes place. Obviously, this process is even more computationally expensive than the cost of a single simulation, and the cost only increases as the cryoprocure progresses, since every simulation with corrected parameter values must restart from the same initial condition at the beginning of the cryosurgical procedure.

The proposed alternative approach of temperature-field reconstruction attempts to use all available data at any given instant in order to generate a current temperature field. In the absence of more detailed information, one could take all the available data at discrete points and approximate the temperature field in the domain by applying some method of interpolation. Here, the method of interpolation is the key to the quality of the reconstructed temperature field. A better-quality interpolation method means a better match between predicted and actual temperature field, while minimizing the number of required data points (i.e., sensors). A

modified Laplacian interpolation is proposed in this study, where the modification is used to account for the blood perfusion term and temperature-dependent thermophysical properties. In practice, this interpolation method implies that the bioheat transfer process is modeled as a quasi-steady problem, where further justification for this modeling approach is provided in the literature [35].

The quasi-steady solution is based on the observation that the heat transfer process during cryosurgery is characterized by a low Stefan number:

$$St_p = \frac{c_p \Delta T_p}{H} \quad (2.2)$$

where ΔT_p is the maximum temperature difference in phase p (either frozen or unfrozen) and H is the latent heat of phase change. When the Stefan number is low, it means that the heat transfer process is dominated by the effect of latent heat rather than sensible heat and, hence, the transient term in Eq. (1) may be neglected [20]. It follows that the temperature distribution in the frozen region can be approximated as a steady solution at any instant, where the transient nature of the system comes about through boundary conditions—the rate of freezing front propagation is most significantly affected by the rate of latent heat absorption or release at the freezing front [35].

2.3 Numerical Solution

Taking the quasi-steady approach to solve Eq. (2.1), the temperature field in the frozen and unfrozen regions in the current study is approximated as:

$$0 = \sum_{l,m,n} \frac{T_{l,m,n} - T_{i,j,k}}{R_{l,m,n-i,j,k}} + (w_b C_b)_{i,j,k} (T_b - T_{i,j,k}) \quad (2.3)$$

where i, j, k are spatial indices of the numerical grid representing the temperature field, l, m, n are spatial indices of the neighboring grid points, and R is the thermal resistance to heat transfer by conduction between node i, j, k and its neighbor l, m, n . For a regular Cartesian geometry, the thermal resistance to heat conduction can be presented as:

$$R_{l,m,n-i,j,k} = \left[\frac{\Delta \eta}{2kA} \right]_{l,m,n} + \left[\frac{\Delta \eta}{2kA} \right]_{i,j,k} \quad (2.4)$$

where $\Delta \eta$ is the space interval in the direction of interest, and A is the representative cross-sectional area perpendicular to the direction of heat flow. Equations (2.3)-(2.4) can be viewed as the steady-state version of the numerical method presented in [51]. Given the temperature

dependency of the thermophysical properties (Table 2.1), Eq. (2.3) is solved simultaneously using an iterative predictor-corrector technique.

Table 2.1: Representative thermophysical properties of soft biological tissue used in the current study [19]

Thermal property	Value	
Thermal conductivity, k , $\text{W m}^{-1} \text{K}^{-1}$	0.5	$273\text{K} < T$
	$15.98 - 0.56T$	$251\text{K} < T < 273\text{K}$
	$1005T^{-1.15}$	$T < 251\text{K}$
Volumetric specific heat, C , $\text{kJ m}^{-3} \text{K}^{-1}$	3,600	$273\text{K} < T$
	15,440	$251\text{K} < T < 273\text{K}$
	$3.98 T$	$T < 251\text{K}$
Blood perfusion rate, $w_b C_b$, W m^{-3}	40,000	$273\text{K} < T$
	0	$T < 273 \text{ K}$
Metabolic heat generation, q_{met} , W kg^{-1}	0.67	$273\text{K} < T$
	0	$T < 273\text{K}$

The simulated domain is assumed infinite from a heat transfer perspective, which means that a large enough domain is assumed, such that thermal information from the cryosurgically treated area would not reach the boundary of the domain during the simulated procedure. In mathematical terms, a core-body temperature (also the initial temperature) is assumed at the boundary of the numerical domain, and the solution is considered valid as long as the heat flux at the boundary remains negligible (unchanged temperature and no heat flux at the boundary of a finite domain make it indistinguishable from an infinite domain). In practice, a domain three-fold bigger than the target region can typically be considered infinite for that purpose.

2.4 Results and Discussion

Five general cases are analyzed in this study, as listed in Table 2.2, with a variable number of temperature sensors up to 12, which led to over 200 special cases. Case A is a full-scale two-dimensional transient solution in a representative cross section of the prostate, which serves as a benchmark. This solution was generated using ANSYS on a prostate contour obtained from ultrasound imaging [26], subject to the following parameters and conditions: (1) eight cryoprobes are used simultaneously; (2) the cryoprobes are cooled from 37°C to -145°C in 30 sec, simulative of Argon-based cryoprobes; (3) the cryoprobe layout is computer generated, using a planning algorithm known as “bubble packing” [53], with the match between the 0°C isotherm and the organ contour as a planning criterion; and, (4) the urethra is maintained at 37°C throughout the procedure, simulative of the commonly applied urethral warmer.

Figure 2.1 displays the basic framework used to evaluate the predictions of the proposed numerical methods (TFRM in Chapter 2 and other methods in succeeding chapters). The ANSYS-generated solution is used to prepare benchmark data for validation. The generated temperature field and the derived locations of isotherm of importance, such as freezing front (0°C), lethal isotherm (-45°C), are used as the basis of comparison.

The ANSYS-generated solution is also used to create simulated measurements used as input for the Inverse Heat Transfer Problem. Virtual imaging data in the form of freezing-front location history is extracted from the benchmark solution. Complete freezing front location data is used to simulate MRI or CT imaging. Partial freezing front location data is used to simulate ultrasound imaging where acoustic shadowing occurs, as discussed in case C. The thermal history at planned sensor locations is extracted from the benchmark solution to create virtual sensor output data. The virtual datasets are then used in conjunction with cryoprobe and urethral warmer information (thermal and spatial) to solve the IHTP. The solution of IHTP is then compared with benchmark to validate the proposed numerical methods.

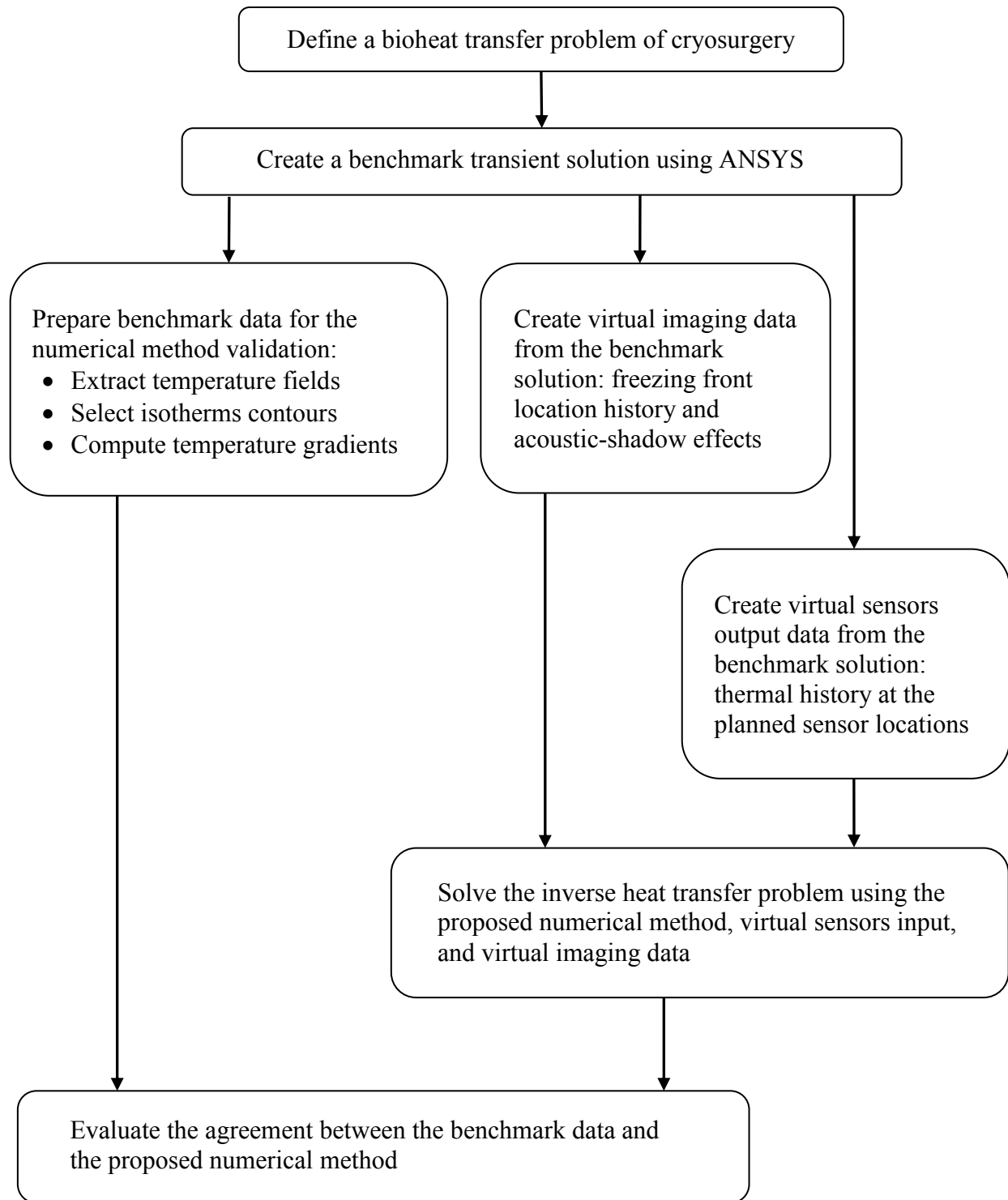


Figure 2.1: Flowchart illustrating the framework to validate the numerical methods developed in the current study. Solution validation is performed in by comparing the reconstructed temperature field (the solution to the simplified,inverse heat transfer problem) and the benchmark (the full-scale solution to the ordinary heat transfer problem).

Table 2.2: A summary of five general cases explored in the current study, where Case A is a benchmark, and the location of the target isotherms for sensors placement is extracted from computerized planning of cryosurgery. Imaging of freezing front location is simulative of MRI, CT (complete contours), or ultrasound (a partial contour). The thermal history of the benchmark is used to simulate extraction of the freezing front location from medical imaging and temperature data obtained from implantable sensors.

		Case A ^a	Case B				Case C					Case D				Case E			
			1 ^b	2 ^c	3	4	1 ^d	2	3	4	5	1	2 ^c	3	4	1	2	3	4
Target isotherm for sensors placement	Organ contour	N/A									+					+	+	+	+
	Freezing front, 0°C						+	+	+	+		+		+	+				
	-22°C isotherm			+		+		+		+	+		+		+		+		+
	Lethal temperature, -45°C				+	+			+	+	+			+	+			+	+
Imaging of freezing front location		Benchmark	Complete Contour				Partial Contour					None				None			
Method of Solution			Transient	Quasi-Steady				Quasi-Steady					Quasi-Steady				Quasi-Steady		

^a Benchmark: Fig. 2.2

^b Special Case I: Figs. 2.3-2.4

^c Special Case II: Fig. 2.5

^d Special Case III: Figs. 2.6-2.7

^e Special Case VI: Fig. 2.8

Figure 2.2 displays results from the benchmark case, while highlighting the typical isotherms of interest: 0°C is the onset of freezing, -22°C is the lower boundary of phase transition, and -45°C is the lethal temperature—a temperature threshold below which maximum destruction is assumed. Reflective of the quality of the computer-generated planning (bubble packing) is the close match between the freezing front as would be viewed by medical imaging (0°C) and the organ contour. The gray area between the onset of freezing and the lethal temperature (-45°C) represents a region where cryodestruction is gradually achieved—the shape and dimensions of this region is critical in the evaluation of the outcome of cryosurgery.

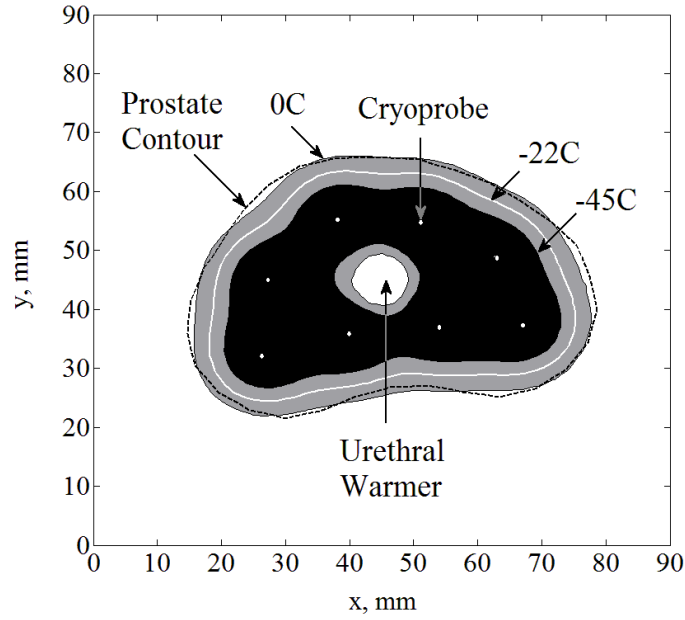


Figure 2.2: Temperature field regions resulted from the transient solution of Case A (the benchmark) at the point of optimal match between the freezing-front location and the prostate contour; cryoprobes are illustrated with white dots.

With reference to Table 2.2, solutions for the various special cases of the quasi-steady problem were obtained using MATLAB, by applying a sparse matrix format and internal solvers for efficiency in calculations. A typical quasi-steady solution was obtained within three seconds on an Intel® Quad Core™ i7 machine with 9 GB RAM, running at 3.07 GHz. Case B is simulative of extraction of the freezing front location from medical imaging such as MRI or CT scanning (not routinely done in real time). In the current study, the benchmark case (Case A) is used to simulate freezing front reconstruction from medical imaging. Since the location of the freezing front is well established in Case B, the effects of implantable sensors are explored only on sensors embedded within the frozen region. It is noted that Rubinsky and co-workers [20, 19] have already reported on a similar effort but without the application of implemented sensors (i.e. using only cryoprobe-embedded sensors and complete freezing-front location from MRI imaging).

Case C is similar to Case B with the exception that only a portion of the freezing front location can be extracted. Case C is simulative of freezing front extraction from ultrasound imaging, where only the portion of the freezing front close to the transducer can be imaged (a detailed example below). While medical imaging is a necessity in minimally invasive

cryosurgery, it is conceivable that temperature-field reconstruction would be attempted without integration with imaging data, which is the investigated scenario in Cases D and E.

Strategies for implantable sensors placement are yet to be developed, where the investigation in current study is focused on four temperature contours relevant to cryosurgery: the target region contour (prostate contour), the freezing front (0°C), the lower boundary of phase transition (-22°C), and the lethal temperature (-45°C). While the target region contour can be identified *a priori*, the location of a particular isotherm for the purpose of sensor placement can only be predicted from bioheat simulations in the process of planning; those isotherms propagate during the cryoprocure, and their location is evaluated in the current study at the point of cryoprobes deactivation. While computer simulations as a part of cryosurgery planning can be used to predict the location of those isotherms [54, 53], the benchmark solution is used for this purpose in the current study.

For the purpose of discussion, letters are used to refer to general cases in the current study (A, B, C, D, and E), and Roman numerals are used to refer to special cases of investigation. The first special case analyzed (Case I) is Case B without the implementation of sensors. Figure 2.3 displays the temperature field regions as predicted by quasi-steady approximation. Figure 2.4 displays the difference between temperature fields predicted by quasi-steady approximation and the benchmark, where the maximum temperature difference, ΔT_{max} , is found to be less than 16°C . This difference is the direct result of neglecting the time-dependent term in the bioheat equation—making the governing equation quasi-steady. The same difference is also affected by the size of the space intervals selected for the numerical grid; however, the grid-size effect is at least one order of magnitude smaller than the effect of neglecting the time-dependent term in the governing equation. In the current study, a uniform grid of 90×90 was used, with a space interval of 1 mm, which is expected to contribute a numerical uncertainty of the order of 10^{-1}°C —significantly smaller than the differences displayed in Fig. 2.4.

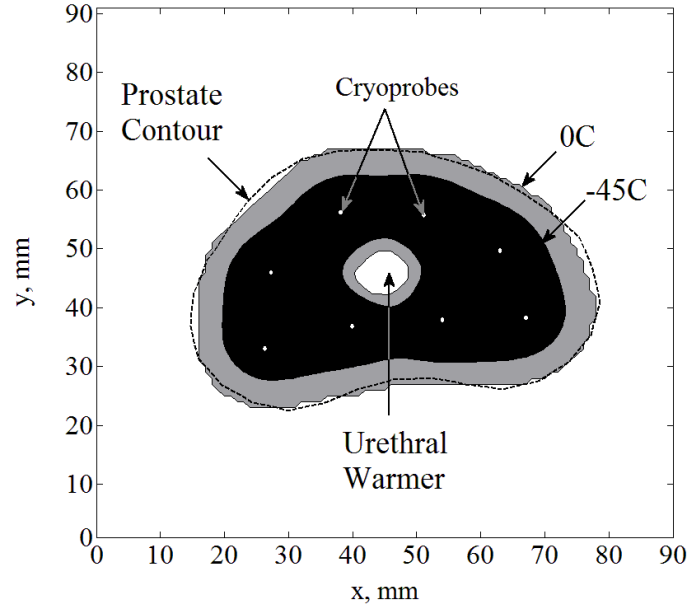


Figure 2.3: Temperature field regions for Case I: complete freezing front information from medical imaging (Case B) with no temperature sensors; cryoprobes are illustrated with white dots.

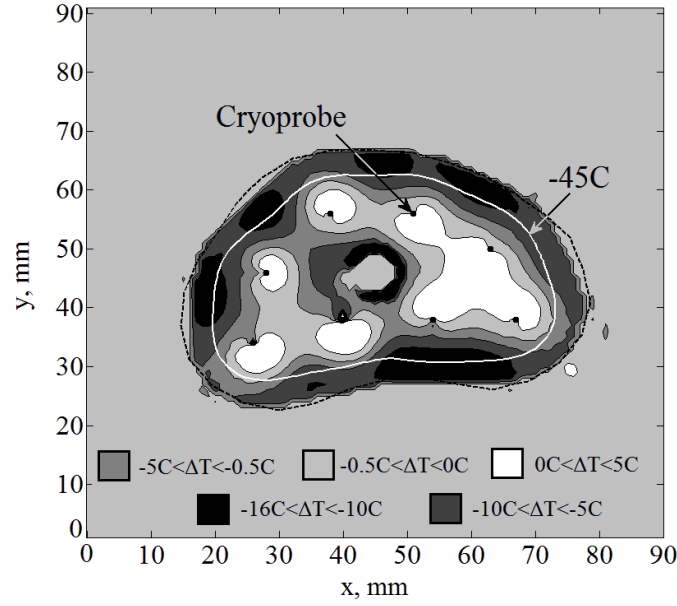


Figure 2.4: Temperature fields difference, ΔT , between the benchmark solution and the solution for Case I: complete freezing front information (Case B) with no temperature sensors; cryoprobes are illustrated with black dots.

The mismatch in the area bounded by the lethal isotherm (-45°C ; urethral warmer area excluded), ΔA_{lethal} , is 9%. It is emphasized that despite its significance, the location of the lethal

temperature isotherm can only be estimated using real-time temperature-field reconstruction, a capability that is yet to be available. Hence, clinicians often think of the lethal temperature but in practice attempt to control only the location of the freezing front. The average distance between those isotherms is defined in this study as:

$$B_{avg,lethal} = \frac{A_{a,lethal} - A_{b,lethal}}{L_{a,lethal}} \quad (2.5)$$

where $A_{a,lethal}$ and $A_{b,lethal}$ are the areas bounded by the -45°C isotherm based on the approximated and benchmark solutions, respectively, and $L_{a,lethal}$ is the length of the lethal temperature isotherm based on the approximated solution. $B_{ave,lethal}$ in the Case I is found to be 0.8 mm.

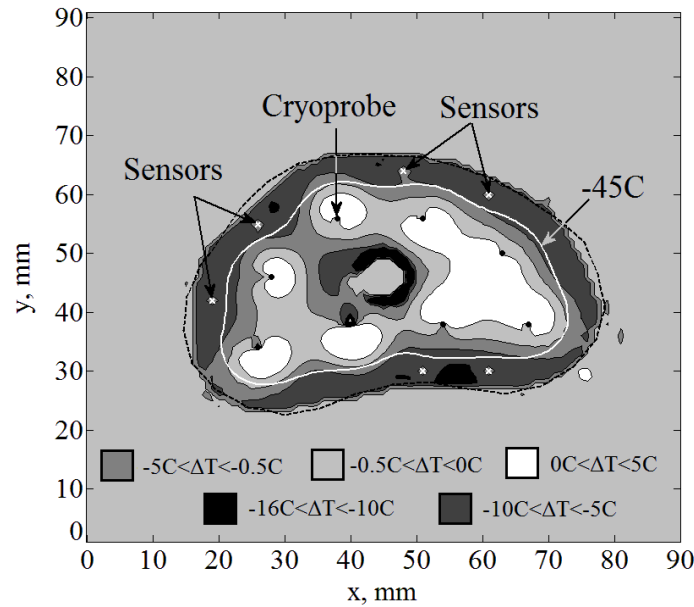


Figure 2.5: Temperature fields difference, ΔT , between the benchmark solution and the solution for Case II: complete freezing front information (Case B) with six sensors implanted along the -22°C isotherm at the locations of maximum temperature difference in Fig. 2.4; cryoprobes are illustrated with black dots and sensors with white “x”.

In effort to improve temperature-field reconstruction, special Case II is now considered, integrating six temperature sensors at the points of maximum temperature differences along the isotherm of -22°C from Case I (can be identified in Fig. 2.4). It can be seen from Fig. 2.5 that ΔT_{max} is now reduced to less than 10°C . For Case II, ΔA_{lethal} is reduced to 6% and $B_{ave,lethal}$ is reduced to 0.5 mm. A similar special case was considered where six sensors are placed along the

lethal temperature instead of the -22°C isotherm but results were worse compared to Case II in terms of the maximum temperature difference, ΔT_{max} ; further case studies showed consistent results. The reasons that the -22°C was originally chosen is that it serves as the lower boundary of phase transition. It can be concluded that the prediction of the phase-transition boundary contour is key to improve the quality of temperature-field reconstruction in terms of ΔT_{max} . However, in clinical practice, knowledge of location of the lethal isotherm (-45°C) is more important. Hence mismatch in the area bounded by the lethal isotherm, ΔA_{lethal} , is used as a metric for comparing the performance of various cases.

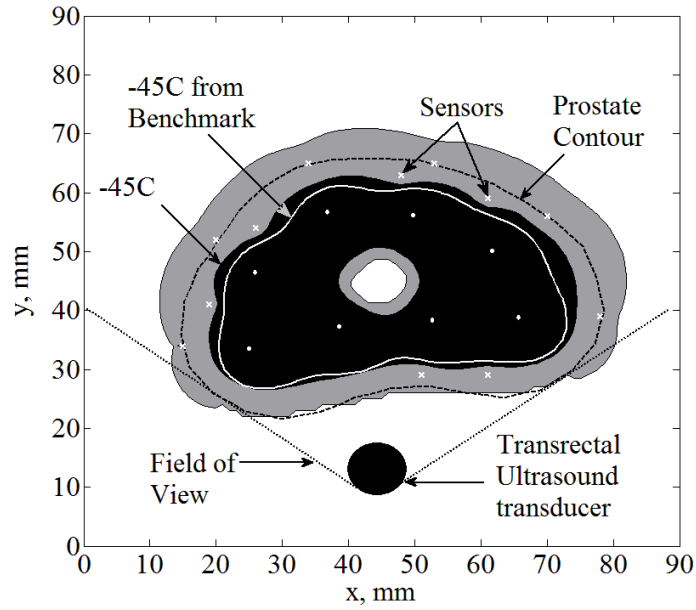


Figure 2.6: Temperature field regions for Case III: partial freezing front information obtained from a trans-rectal ultrasound transducer (Case C), combined with six sensors implanted along the -22°C isotherm, and six additional sensors equally distributed along the unobservable portion of the prostate contour (upper portion of the figure); α is the field of view of the trans-rectal ultrasound transducer; cryoprobes are illustrated with white dots and sensors with white “x”.

Case III is a special case of the more realistic scenario, where only a portion of the frozen region in the prostate is observable with a trans-rectal ultrasound transducer (TRUS, Case C). Typically, about one third of the frozen region can be identified, as shown in Fig. 2.6, where the frozen region is completely opaque to the ultrasound signals. The same six sensors used in Case II are also used in Case III. In addition, six sensors are distributed in equal distances along the unobservable portion of the prostate contour in Case III. Results in this case indicate

$\Delta T_{max}=41^{\circ}\text{C}$, $\Delta A_{lethal}=14\%$, $B_{ave,lethal}=1.4\text{mm}$, and $B_{max,lethal}=3.5\text{ mm}$, where the distribution of the temperature difference between Case III and the benchmark solution is displayed in Fig. 2.7. While a temperature-difference of 41°C may be considered significant for some purposes, comparable data from current clinical practice is literally nonexistent. When taking into account the uncertainty in ultrasound imaging in the range of 1 to 2 mm, the error in predicting the lethal temperature location is quite remarkable, especially given the temperature gradients in the frozen region (of the order of $10^{\circ}\text{C}/\text{mm}$). While the optimal number and layout of sensors remain to be explored, Case III represents a scenario where implantable sensors could only improve the outcome of clinical practice.

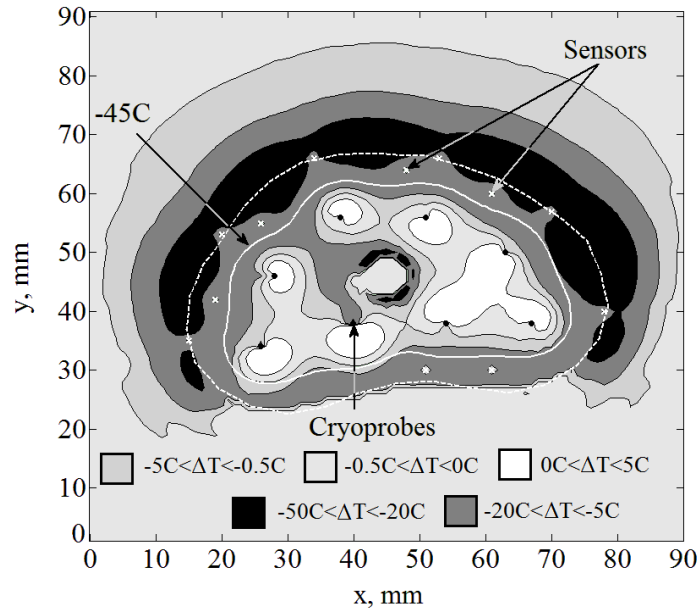


Figure 2.7: Temperature fields difference, ΔT , between the benchmark solution and the solution for Case III: partial freezing front information obtained from a trans-rectal ultrasound transducer (Case C) combined with six sensors implanted along the -22°C isotherm, and six additional sensors equally distributed along the unobservable portion of the prostate contour (upper portion of the figure); cryoprobes are illustrated with black dots and sensors with white “x”.

Case IV represents a practical case where freezing front data is not used for temperature-field reconstruction, where twelve temperature sensors are equally distributed along the -22°C isotherm. While special Case IV belongs to general Case D, if the cryoprobe layout is optimal, Case IV will essentially also be representative of general Case E (the quality of such a match is demonstrated in Fig. 2.2). The resulted temperature field for Case IV is shown in Fig. 2.8, where

$\Delta T_{max}=47^{\circ}\text{C}$, $\Delta A_{lethal}=19\%$, $B_{ave, lethal}=1.8\text{ mm}$, and $B_{max, lethal}=4\text{ mm}$. While the prediction of the location of the lethal temperature is off by 1.8 mm on average and approaches a value of 5 mm at the location of maximum disagreement, the predicted lethal temperature isotherm is still bounded by the organ contour. Hence, when the location of the lethal temperature is of high priority, the application of implantable sensors and the proposed reconstruction method can potentially improve real-time feedback on the procedure. Furthermore, the onset of freezing can be evaluated straightforwardly from medical imaging, and its integration with the information displayed here would improve the control over the destructive effects of freezing.

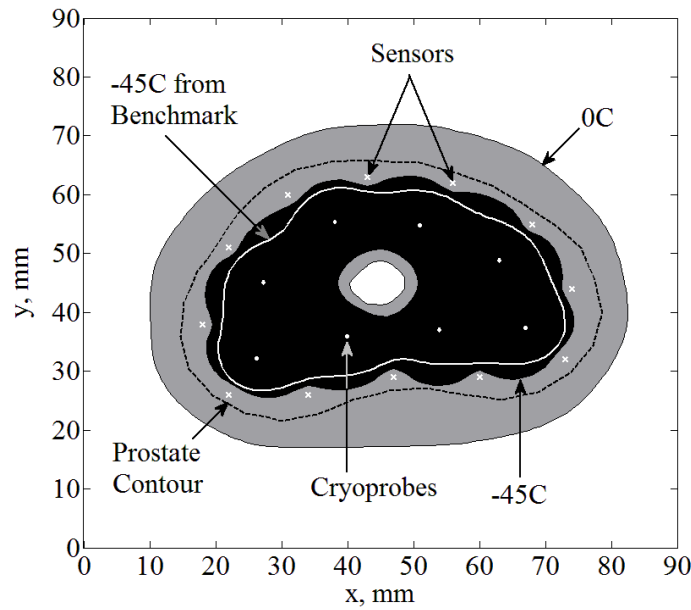


Figure 2.8 Temperature field reconstruction for Case IV (Case D—solely based on temperature sensors with no imaging data): twelve sensors equally distributed along the -22°C isotherm; cryoprobes are illustrated with white dots and sensors with white “x”.

The relationship between the number of sensors and mismatch in lethal area, ΔA_{lethal} , can be seen in Figs. 2.8, 2.9, and 2.10, for Cases B, C, and D, respectively. When sensors were equally distributed along more than one isotherm, the distance between sensors on the different isotherms was maximized. As could be expected, the increasing number of sensors always decreases ΔA_{lethal} , regardless of the particular sensor layout. For Case B (Fig. 2.9), the quality of lethal temperature reconstruction is less sensitive to the strategy of selecting the sensor layout, and ΔA_{lethal} is in the order of a percent. It is interesting to compare the results displayed in Fig. 2.9 with the results of Case II, which is based on Case B when six sensors are not equally

distributed, but strategically placed in areas where the largest mismatch is expected along the -22°C isotherm (Fig. 2.5). Results of Case II suggest that the specific sensors layout would yield better results than placing them along the -45°C isotherm. While the results displayed in Figs. 2.4 and 2.8 may appear inconsistent at first glance, one should bear in mind that the cases are not identical, and that the results are influenced by different placement strategies. This comparison illustrates that the optimal sensor layout should be evaluated on a case-by-case basis.

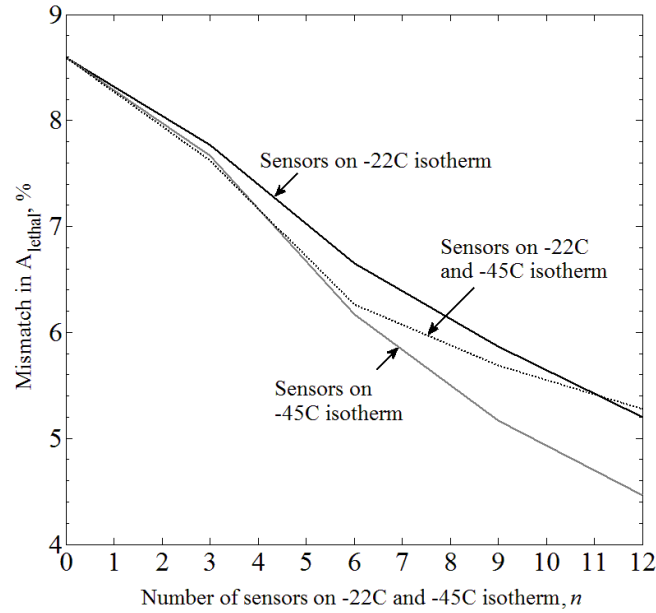


Figure 2.9: Mismatch in the areas bounded by the lethal isotherm, ΔA_{lethal} , between the benchmark (Case A) and the Case B, where complete freezing-front data is available from medical imaging, and the temperature sensor are equally distributed along predicted isotherms.

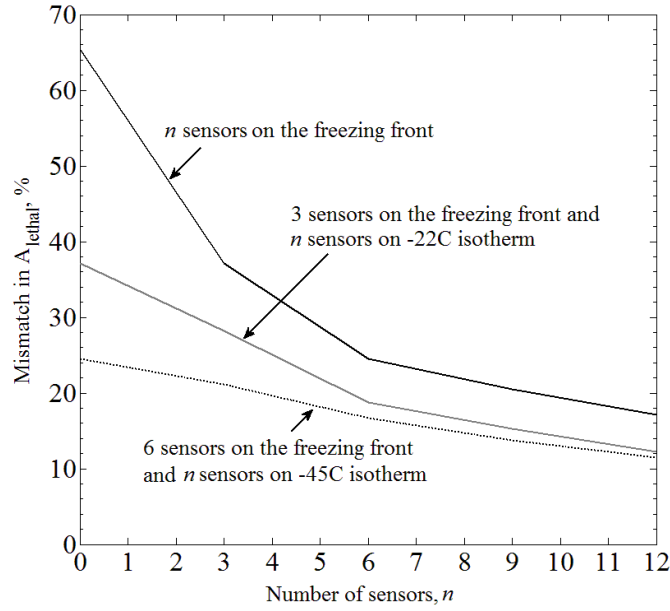


Figure 2.10: Mismatch in the areas bounded by the lethal isotherm, ΔA_{lethal} , between the benchmark (Case A) and the case of partial freezing-front data available from medical imaging (Case C), where the temperature sensors are equally distributed along the freezing front, and combined with temperature sensors distributed along the -22°C and -45°C isotherms.

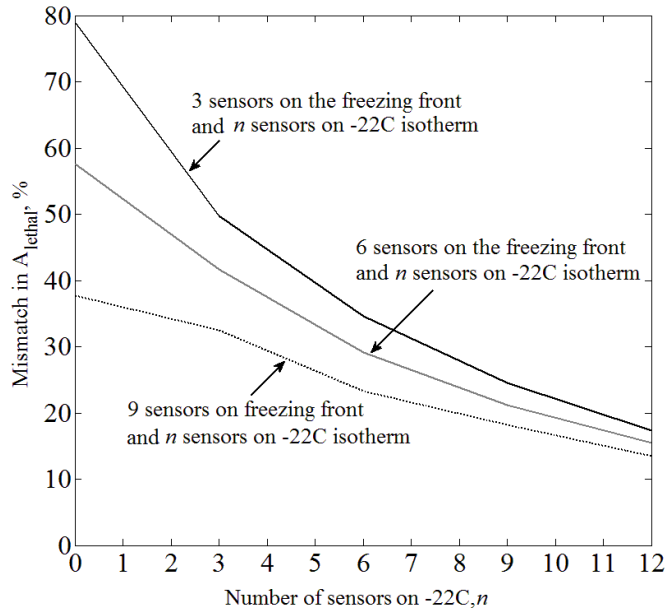


Figure 2.11: Mismatch in the area bounded by the lethal isotherm, ΔA_{lethal} , between the benchmark (Case A) and the case where no imaging data is available for the purpose of extracting the location of the freezing front (Case D), where temperature sensors are equally distributed along the -22°C and -45°C isotherms.

For Case C (Fig. 2.10), placing sensors at the predicted location of the freezing front is detrimental to the quality of lethal isotherm reconstruction. Interestingly, placing nine sensors on the freezing front, six sensors on the freezing front and three sensors on the -22°C isotherm, or three sensors on the freezing front and six sensors on the -22°C isotherm, all resulted in $\Delta A_{lethal} \approx 21\%$, for the particular prostate model and cryoprobe layout under investigation. This observation was not repeated for a larger number of sensors. While Figs. 2.9-2.11 display an expected trend of improving the quality of temperature-field reconstruction with the increasing number of sensors, rules for the optimal strategy of sensor placement remain to be explored. Given the virtually infinite number of possibilities for sensor layout, computer planning has the potential of automatically and efficiently selecting a high quality sensor layout.

2.5 Summary

The objective of this chapter is to reconstruct the temperature field in 2D. To achieve this goal, the following inputs are used to solve the approximated quasi-steady problem of heat transfer: cryoprobe location and their thermal histories, urethral warmer location and its thermal history, freezing front location extracted from medical imaging, and temperature data collected from sensors embedded in the tissue. Results of the study presented in this chapter suggest that temperature field reconstruction in 2D in real time is feasible, using TFRM and a commercially available code. The typical run time required to obtain a solution is in the range of 2 to 3 seconds for all the presented cases. When TFRM is used with only ultrasound imaging as input (Case I), the average mismatch was 0.8 mm. With the introduction of 6 temperature sensors at specific locations, average mismatch was reduced to 0.5mm (Case II). Similar results are also observed for other cases. The average mismatch predicted in all the cases is found to be less than 2mm which is of the same magnitude as the current imaging modalities. The magnitude of the mismatch reduces with increasing number of sensors. Sensitivity analysis results demonstrate the effect of sensors layout on the quality of the reconstructed isotherm, suggesting a need for developing a strategy and an optimization method for sensors placement.

Chapter 3: Potential Field Analogy Method (PFAM), Hybrid (PFAM + TFRM) and Experimental Validation in 2D

In Chapter 2, computationally inexpensive TFRM was described. The results demonstrated that it is feasible to reconstruct the temperature field inside the targeted region of the prostate in near real-time. However, as reviewed in Chapter 2, the continuous effort towards device miniaturization in cryosurgery has led to a decline and sometimes abandonment of temperature sensors in prostate cryosurgery. Ultrasound imaging is used to monitor the developing frozen region. Due to the behavior of ultrasound waves in presence of frozen tissue, the full extent of frozen region is not visible, which gives rise to an acoustic shadow. This lack of knowledge of the precise extent of freezing in the acoustic shadow is a major cause of side effects during cryosurgery [22].

In this chapter, a new mathematical model (PFAM) is presented to approximate the extent of freezing in the acoustic shadow region. Experimental data generated earlier by Dr. Michael Rossi in Biothermal Technology Laboratory [15] are used here to verify the feasibility and accuracy of PFAM. The newly developed PFAM is then integrated with TFRM to create a computationally inexpensive hybrid framework (PFAM + TFRM), which potentially alleviates the need for additional temperature sensors. The 2D model of the prostate utilized in the previous chapter is used here to perform computer validation of hybrid framework. Finally, known thermal history from experimental data is used to verify predictions of the hybrid method.

3.1 Mathematical Formulation

3.1.1 A new potential field analogy method (PFAM)

This study presents a new method to approximate the freezing front location in the acoustic shadowed area during prostate cryosurgery, as schematically illustrated in Fig. 3.1.

The proposed method is based on following principles:

- (a) The temperature field within the simulated cryosurgery domain is analogous to an electric-potential field, where isotherms are analogous to isoelectric lines.
- (b) Cryoprobes are analogous to static electric charges.
- (c) Thermal inertia effects are negligible, where the problem is essentially a quasi-steady problem [34].

- (d) The location of the cryoprobes and their thermal history are known.
- (e) The location and temperature of the urethral warmer are known.
- (f) The location of some portion of the freezing front is known, as illustrated in Fig. 3.1(b).
- (g) The problem is solved in two dimensions (2D), representing the prostate cross-section displayed on the ultrasound monitor. While no limitation exists on extending the PFAM to three dimensions (3D), the 2D formulation represents a choice of practice for method demonstration.

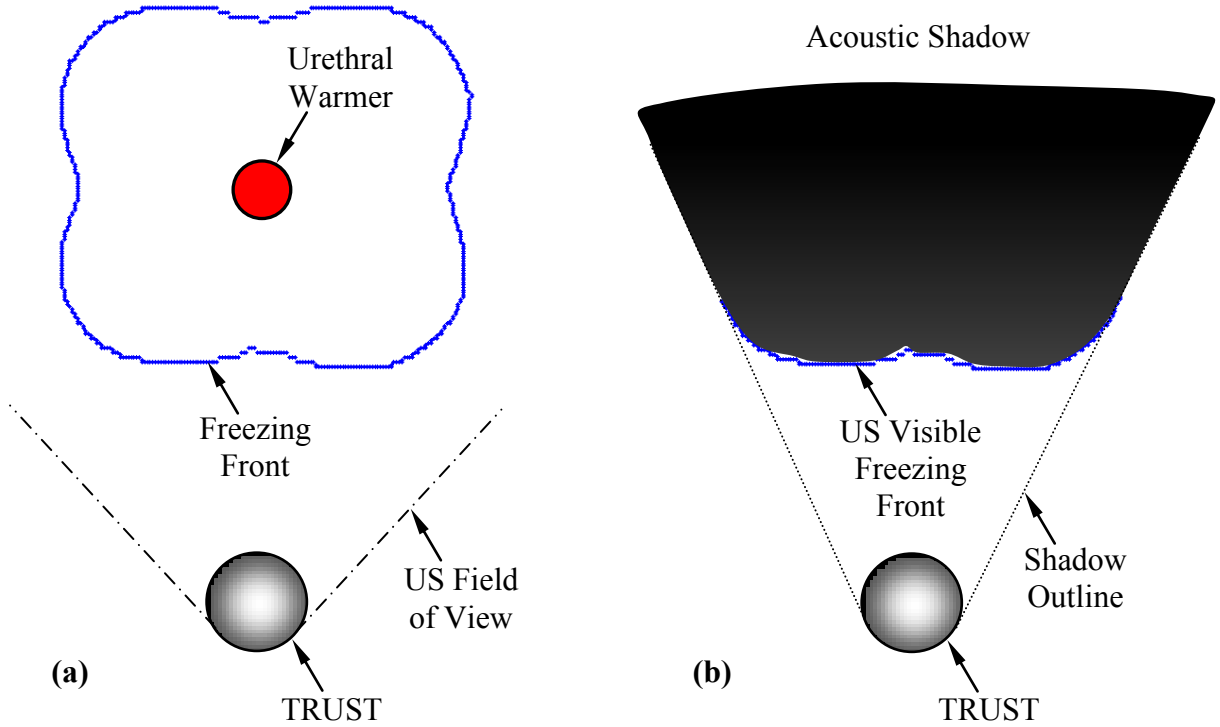


Figure 3.1: Schematic illustration of a representative cross section during prostate cryosurgery displaying: (a) the ultrasound transducer, the freezing front, and the urethral warmer; and (b) the acoustic shadow by the frozen region and the partially visible freezing front on the ultrasound (US) monitor.

The potential field in presence of a number of static electric charges is given by [55]:

$$V(x, y) = \alpha \sum_{i=1}^m \frac{q_i}{r_i} \quad (3.1)$$

where α is a field constant, q_i is magnitude of the i^{th} charge, r_i is distance from the i^{th} charge to a field point of interest (x, y) , and m is the total number of charges.

In analogy, a quasi-steady, pseudo-temperature field is modeled by:

$$\theta(x, y) = \kappa \sum_{i=1}^n \frac{c_i}{r_i} \quad (3.2)$$

where κ is a field constant, c_i is a cooling constant of the i^{th} cryoprobe, and n is the total number of cryoprobes. In principle, c_i may be time dependent, temperature dependent, cooling-rate dependent, or exhibit any other implicit behavior. Nevertheless, since Eq. (3.2) is applied on an ultrasound snapshot, and since c_i is evaluated based on data from the same snapshot, an *a priori* knowledge of the functional behavior of c_i is not needed. The strategy for evaluating the instantaneous values of c_i in the current study relies on the conditions that all cryoprobes are operated simultaneously, and that all cryoprobes have similar physical dimensions and cooling capabilities. These similarities suggest c_i values in a close range for all cryoprobes. Hence, a simplifying assumption is made in the current study that all c_i are actually identical at any given point in time, where the implications of this assumption are discussed below. For this simplified case, the pseudo-temperature field becomes:

$$\theta(x, y) = \beta \sum_{i=1}^n \frac{1}{r_i} \quad ; \quad \beta \equiv c_i \kappa \quad (3.3)$$

where the value of β is selected such that one of the isotherms of the pseudo-temperature field optimally matches the US-visible portion on the freezing front. This is essentially a minimization problem, characterized by an explicit set of algebraic equations.

3.1.2 Application of a temperature-field reconstruction method (TFRM)

In principle, the PFAM allows to estimate the freezing front location, as presented in the results and discussion section below. However, in order to gain more information about the temperature field within the frozen region, a recently developed quasi-steady temperature-field reconstruction method (TFRM) [34] can be integrated. In particular, the location of the so-called lethal temperature isotherm may be of particular interest to the clinician. While many alternatives can be chosen to reconstruct the quasi-steady temperature field, the algorithm presented in [34] is potentially suitable for real-time simulations and represents a choice of practice. This algorithm is presented here in brief only, for the completeness of presentation, while the reader may refer to [34] for more detail.

It is customary to assume that heat transfer during cryosurgery can be modeled with the classical bioheat equation [44]:

$$C_t \frac{\partial T}{\partial t} = \nabla(k \nabla T) + w_b C_b (T_b - T) + q_{met} \quad (3.4)$$

where C_t is the volumetric specific heat of the tissue, T is the temperature, t is the time, k is the thermal conductivity, w_b is the blood perfusion rate, C_b is the volumetric specific heat of the blood, T_b is the blood temperature entering the treated region, and q_{met} is the metabolic heat generation. It has been previously suggested [46] that the bioheat transfer equation is suitable for prostate cryosurgery, in the absence of major blood vessels, and that the metabolic heat generation effect is negligible during cryosurgery [46]. Typical thermo-physical properties for Eq. (3.4) are listed in Table 3.1.

The TFRM is based on the fact that the heat transfer problem during cryosurgery is characterized by a small Stefan number:

$$St = \frac{C_t \Delta T}{H} \quad (3.5)$$

where ΔT is the maximum temperature difference within the frozen region and H is the latent heat of freezing. The heat transfer process is primarily dominated by the latent heat effect when Stefan number is small and, hence, the transient term in Eq. (3.4) may be neglected [20]. This observation also supports the underlying principles of the PFAM, where inertia terms are neglected. Nevertheless, the overall transient nature of freezing process is not neglected, but introduced through boundary conditions. These boundary conditions may be external, such as at the outer surface of the domain, the cryoprobe surface, or the urethral warmer surface. These boundary conditions may also be internal such as at the imaged freezing front [34]. Data collected from tissue-embedded temperature sensors can be used for model verification but cannot be regarded as a boundary condition [34].

Table 3.1: Representative thermophysical properties of soft biological tissue used in the current study [51]

Thermal property	Value	
Thermal conductivity, k , $\text{W m}^{-1} \text{K}^{-1}$	0.5	$273\text{K} < T$
	$15.98 - 0.56T$	$251\text{K} < T < 273\text{K}$
	$1005T^{-1.15}$	$T < 251\text{K}$
Volumetric specific heat, C , $\text{kJ m}^{-3} \text{K}^{-1}$	3,600	$273\text{K} < T$
	15,440	$251\text{K} < T < 273\text{K}$
	$3.98 T$	$T < 251\text{K}$
Blood perfusion rate, $w_b C_b$, W m^{-3}	40,000	$273\text{K} < T$
	0	$T < 273 \text{ K}$
Metabolic heat generation, q_{met} , W kg^{-1}	0.67	$273\text{K} < T$
	0	$T < 273\text{K}$

The TFRM attempts to use all the available data in order to evaluate the instantaneous temperature field, using a modified Laplacian interpolation method based on the following explicit formulation [34]:

$$0 = \sum_{l,m,n} \frac{T_{l,m,n} - T_{i,j,k}}{R_{l,m,n-i,j,k}} + (w_b C_b)_{i,j,k} (T_b - T_{i,j,k}) \quad (3.6)$$

where i, j, k are spatial numerical grid indices, l, m, n are indices of the neighboring grid points, and R is the thermal resistance to heat transfer by conduction between grid point i, j, k and its neighbor l, m, n . For a regular Cartesian geometry, the thermal resistance to heat conduction can be simplified as:

$$R_{l,m,n-i,j,k} = \left[\frac{\Delta\eta}{2kA} \right]_{l,m,n} + \left[\frac{\Delta\eta}{2kA} \right]_{i,j,k} \quad (3.7)$$

where $\Delta\eta$ is the distance between the point of interest and its neighbor, and A is the representative cross-sectional area perpendicular to the direction of heat conduction. Since the thermophysical properties in the tissue are temperature dependent (Table 3.1), Eqs. (3.6)-(3.7) are solved using an iterative predictor-corrector technique.

3.1.3 Integration of PFAM with TFRM

Figure 3.2 displays a schematic illustration of a computation framework to integrate the proposed PFAM with the established TFRM. With reference to Fig. 3.2, input data may come from various sources. In a clinical procedure, partial freezing front location would come from ultrasound imaging, cryoprobe thermal histories would come from embedded temperature sensors at the cryoprobe tips, urethral warmer temperature would come from the warming device, and the layout of cryoprobes and warmer would come from preplanning or ultrasound registration. For the bench-top setup described in the next section, the partial freezing front is simulated from experimental data (discussed below), the cryoprobe thermal histories are measured similar to clinical practice, and the cryoprobe layout is set with a special placement grid.

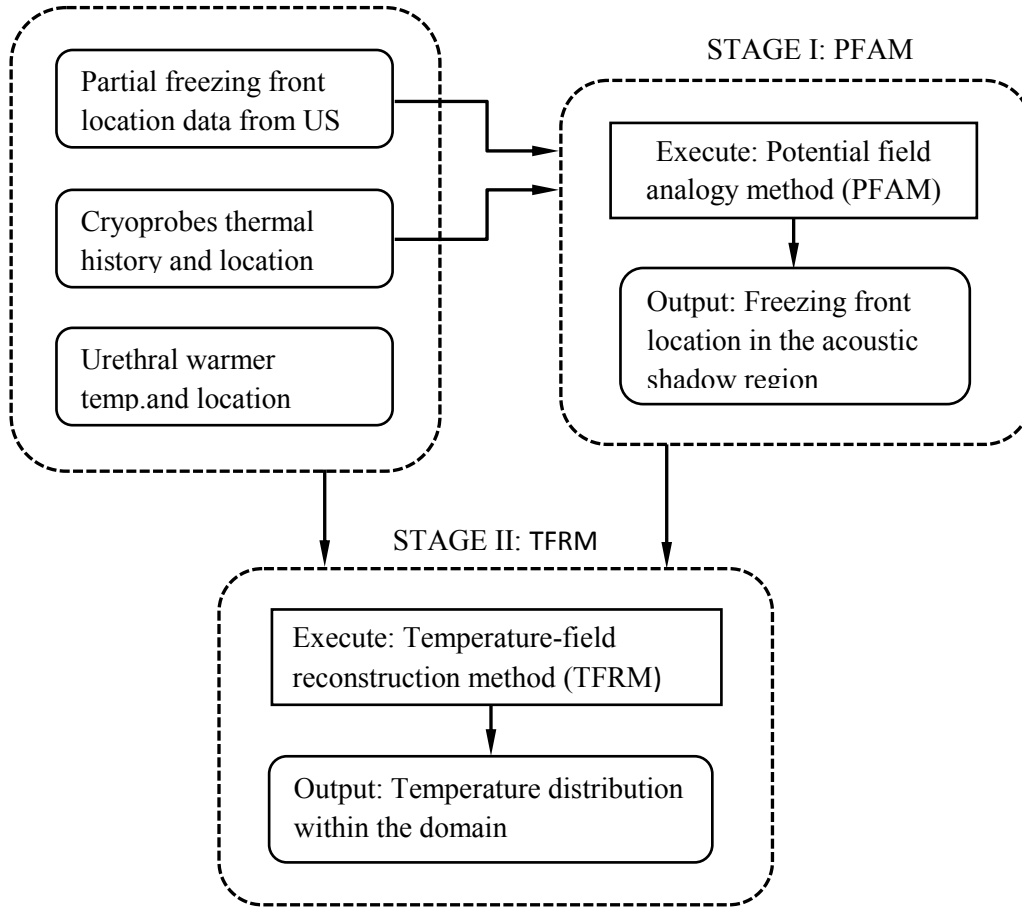


Figure 3.2: Integration of PFAM and TFRM for the purpose of (I) freezing front estimation in the invisible area of the US image, and (II) thermal history evaluation.

The framework in Fig. 3.2 is based on two stages. In the first stage, partial freezing front location and cryoprobe thermal histories are used to estimate the hidden portion of the freezing front using the PFAM. Being at the center of the frozen region, the urethral warmer data is not needed for that estimation. In the second stage, the evaluated freezing front location in the acoustic shadow region is integrated with all other input data, in order to evaluate the temperature field in the domain by means of TFRM. Note that TFRM has already been validated for a complete or partial freezing-front contour [34], while the current study focuses on the improvement of this method by creating additional data by means of PFAM.

3.2 Experimental Verification

While experimental verification with clinical results would serve as the ultimate test, no such data is available for the current study. In particular, frozen region scanning in combination with TRUST registration are major challenges in clinical practice. Instead, the experimental verification in the current study is based on a bench-top physical simulator of the procedure. This simulator has been created to validate computer simulations of the cryoprocure [15], and to verify computerized planning of prostate cryosurgery [51]. The experimental system and image analysis techniques have been presented in detail previously [15] and are overviewed here in brief, for the completeness of presentation.

3.2.1 Experimental setup

The experimental system consists of a transparent phantom material container, an array of proprietary liquid nitrogen-based cryoprobes (1.3 mm OD)[15], and a proprietary electrical urethral warmer (7 mm OD) also termed *cryoheater* [56]. A side view of the phantom-embedded cryoprobes and cryoheater is displayed in Fig. 3.3 (parallel to the cryoprobe axes). The container is made of thick Plexiglas walls (5 mm), having overall dimensions of 25 mm \times 200 mm \times 200 mm. In particular, the internal width of the container equals to the length of the active surface of the specific cryoprobes (15 mm), such that the heat transfer process is essentially 2D in a plain transverse to the cryoprobe axes (see [15] for detailed thermal analysis). The heater and cryoprobes are inserted through special holes in the container, which enable variable cryoprobe layouts. The combined heat transfer process generated by the cryoprobes and cryoheater is simulative of the largest cross-section of the prostate during cryosurgery.

The image displayed in Fig. 3.3 is a snapshot from a high-resolution movie recorded throughout the experiment. The phantom material displayed in Fig. 3.3 is distilled water mixed with 1.3% gelatin and blue food dye. Once cured, the gelatin prevents natural convection currents in the distilled water, and pure heat conduction process is created in a well characterized material. The food dye is used as a visual enhancement means, where the frozen dyed water changes color from blue to white.

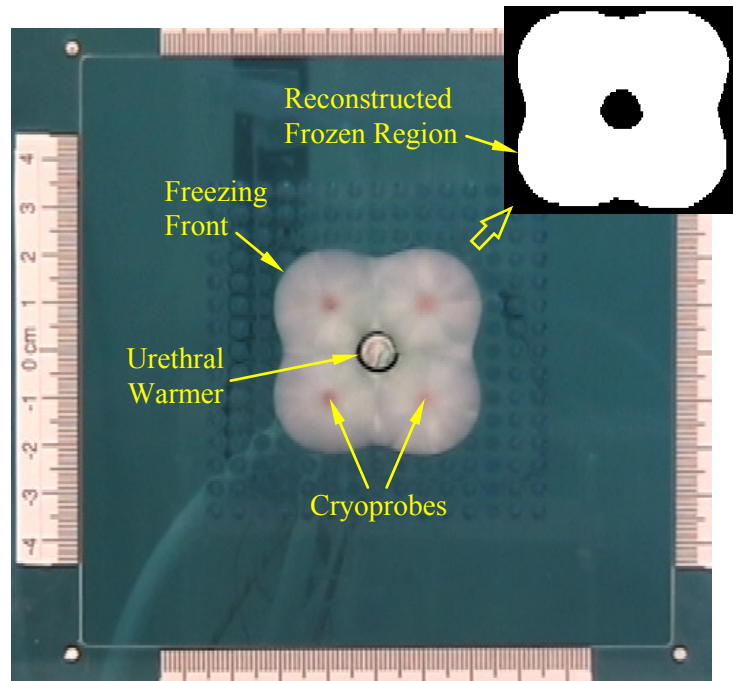


Figure 3.3: A representative snapshot from a video recording of a simulated cryosurgery procedure [15], where the medium is distilled water mixed with 1.3% gelatin and blue food dye. The reconstructed frozen region is shown on the top-right corner of the image, which is the basis for the displayed freezing front contour in Fig. 3.1.

Up to six cryoprobes can be used concurrently in the specific setup, which is fed by a portable liquid nitrogen container and powered by compressed air (30 psi)[15]. The resulting thermal history at the cryoprobes is a cooling rate of about $33^{\circ}\text{C}/\text{min}$ in the first three minutes of operation and a minimum operation temperature of about -110°C . The actual thermal history for each cryoprobe is measured during experimentation by means of thermocouples embedded at the cryoprobe-tips, and the continuous data streams are recorded with a computerized data logger. Urethral warming in the current setup is simulated with the self-controlled cryoheater set to a

constant temperature of 25°C, which equals to the initial temperature of the phantom material. In selected experiments, clinical-grade hypodermic thermocouples (type T, 1.5 mm OD) are also strategically placed within the domain, in order to measure the thermal history at specific locations for comparison with simulation results.

3.2.2 Simulating ultrasound imaging from experimental data

The current study uses previously generated frozen region reconstructions from selected experiments [15]. In brief, individual images from the recorded video of each experiment were captured and post-processed. Reconstruction of the frozen region from this image was performed in four stages: (i) manual registration by identifying the locations of each cryoprobe and the cryoheater, (ii) applying selected MATLAB filters for image enhancement, (iii) segmentation by a MATLAB implementation of a region-growing method [57, 58], and (iv) application of a dilation transformation [59] to increase the quality of the reconstruction frozen region.

Figure 3.3 displays a representative captured image from a recorded movie, where the inset on the top-right displays the reconstructed frozen region. That inset was used to extract the freezing front, previously displayed in Fig. 3.1 to discuss the acoustic shadowing effect. For the purpose of the current study, the TRUST image location was assumed such that one-third of the frozen region contour becomes ‘visible’, Fig. 3.1(b).

3.2.3 Comparison approach of numerical results with experimental data

Comparison of numerical results with experimental data is based on (i) the evolution of the frozen-region shape over time, and (ii) the thermal history at pre-selected points in space. For the comparison of the frozen-region shape, the PFAM predictions are compared with the freezing front location reconstructed from experimental data. The mismatch between those curves is quantified by the so-called Hausdorff distance, which is commonly used in medical imaging [60], curves analysis [61], and computer vision [62].

In brief, the Hausdorff distance between two curves is defined as the maximum distance from one curve to the nearest point on the other curve [63]. For two sets of points representing curves $A = \{a_1, a_2, \dots, a_p\}$ and $B = \{b_1, b_2, \dots, b_q\}$, the Hausdorff distance from A to B is given by:

$$H(A, B) = \max_{a \in A} \min_{b \in B} \|a - b\| \quad (3.8)$$

where an Euclidean norm is used to calculate $\|a-b\|$ [62]. The current study also makes use of a modified Hausdorff distance, which represent an average distance:

$$H(A,B)_{mod} = \frac{1}{|A|} \sum_{a \in A} \min_{b \in B} \|a - b\| \quad (3.9)$$

where $|A|$ is the number of points in A . The modified Hausdorff distance is also widely used in image processing applications [64]. Since the modified Hausdorff distance is an average quantity, it decreases the impact of outliers and hence it is more useful in pattern comparing applications. In this study, ΔS_{max} stands for $H(A,B)$ where A is the estimated freezing front location and B is the actual (observed) freezing front location. Consistently, ΔS_{avg} stands for the modified Hausdorff distance, $H(A,B)_{mod}$.

3.3. Results and Discussion

Validation of the proposed PFAM and its integration with the TFRM are studied in three steps representing increasing-complexity: (i) comparison of the freezing front location based on the PFAM with experimental results of simplified cases; (ii) comparison of the freezing front location based on the PFAM with simulated ANSYS results of more complex cases, and (iii) comparison of the estimated thermal history based on the integrated PFAM and TFRM method with experimental data.

3.3.1 Experimental validation of PFAM

Experimental validation of the PFAM is performed for three typical cases. Case A represents freezing process as a result of four cryoprobes symmetrically arranged around a urethral warmer, Fig. 3.4. Note that the experimental results from Fig. 3.4(a) are extracted from Fig. 3.4. Cases B and C represent similar results for six cryoprobes in an increasing layout complexity, with results displayed in Figs. 3.5 and 3.6, respectively. Table 3.2 lists mismatch values between experimental data and PFAM results for cases A-C.

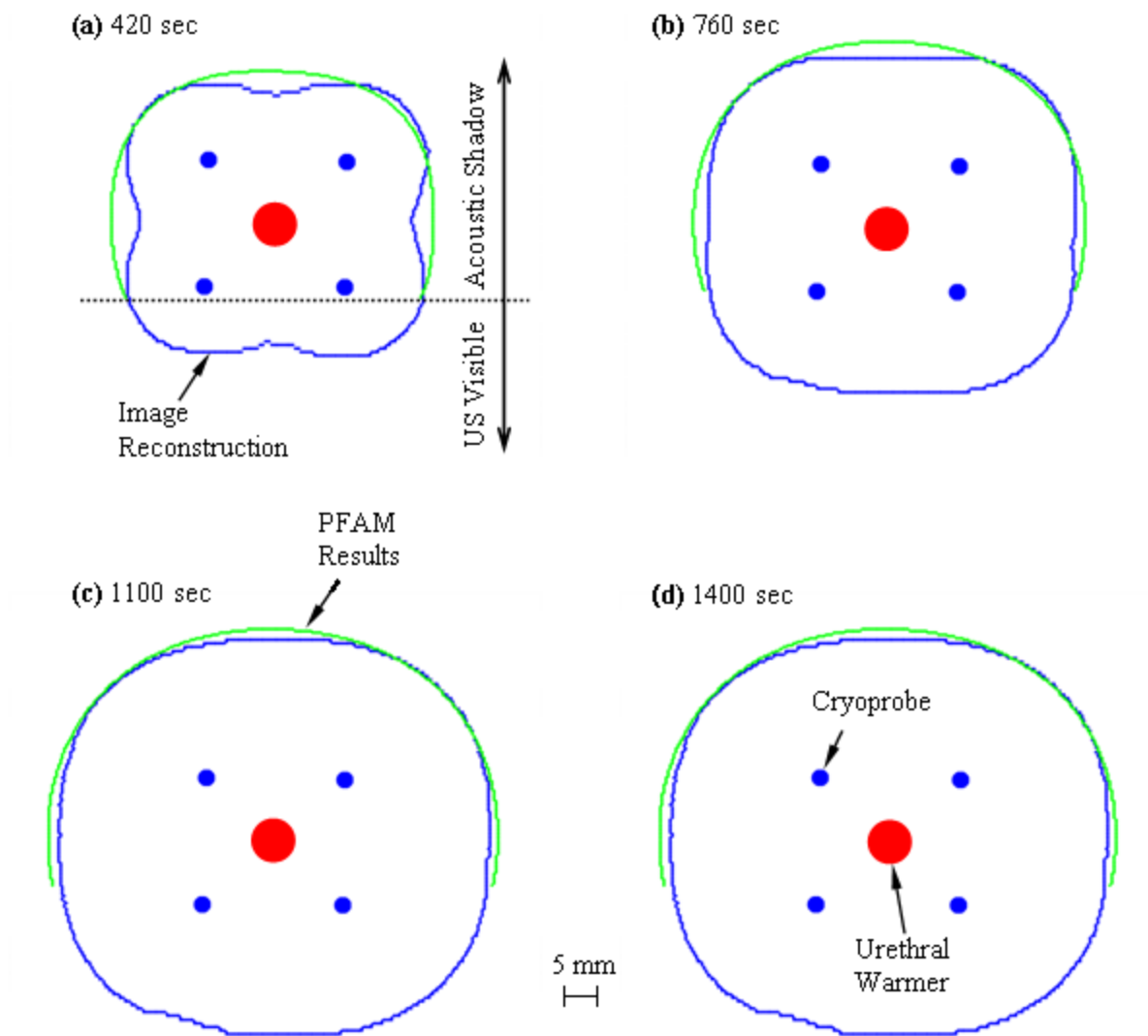


Figure 3.4: Comparison between PFAM estimation for the 0°C isotherm (green curve) and freezing-front reconstruction from experimental results (blue curve) for Case A, where the PFAM results are only presented within the simulated acoustic shadow area (Fig. 4(a) is also presented in Figs. 3.1 and 3.3).

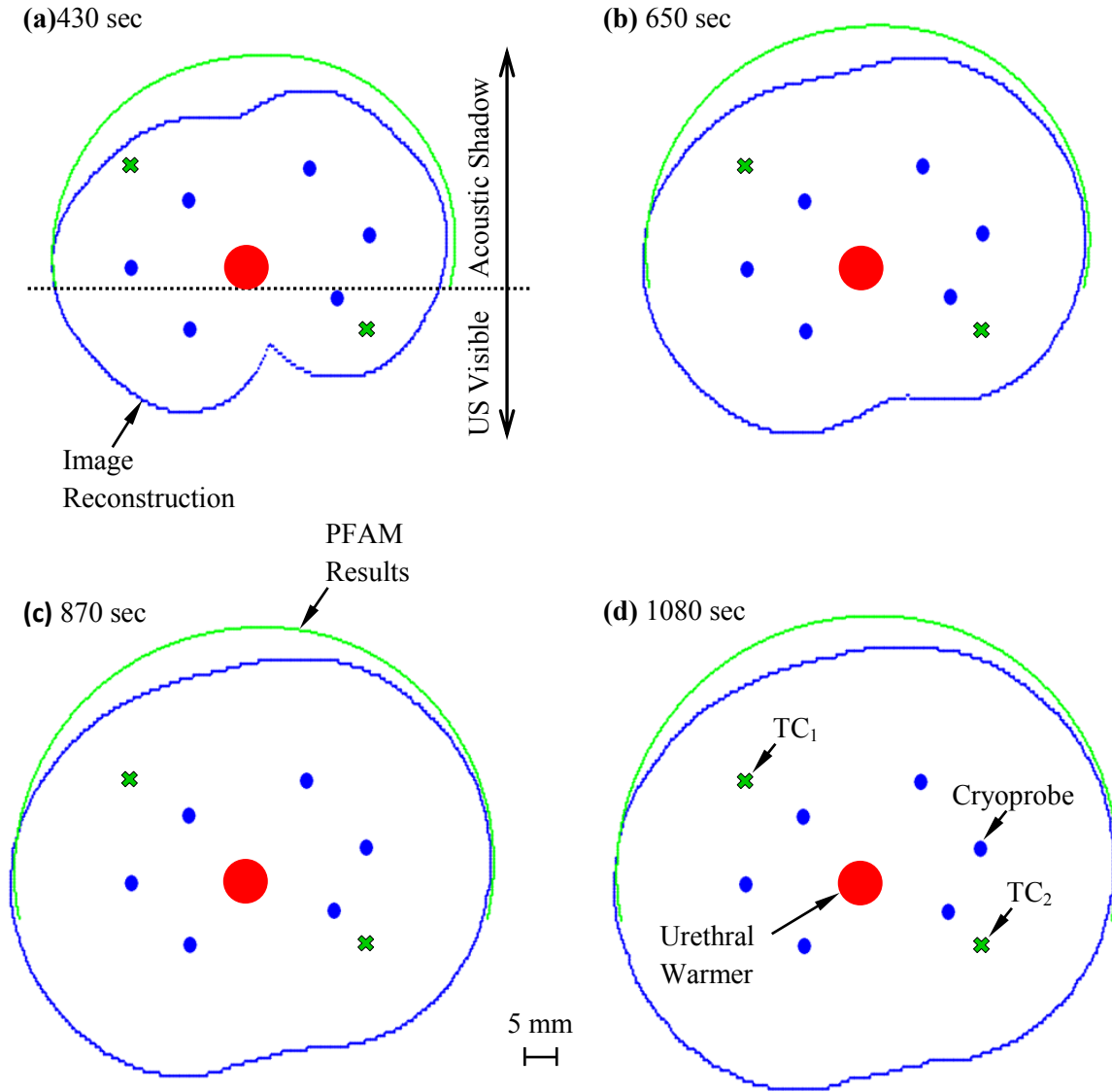


Figure 3.5: Comparison between PFAM estimation for the 0°C isotherm (green curve) and freezing-front reconstruction from experimental results (blue curve) for Case B, where the PFAM results are only presented within the simulated acoustic shadow area. TC₁ and TC₂ are thermocouples embedded in the freezing medium and used to validate the integration of PFAM and TFRM method in the context of Fig. 3.9.

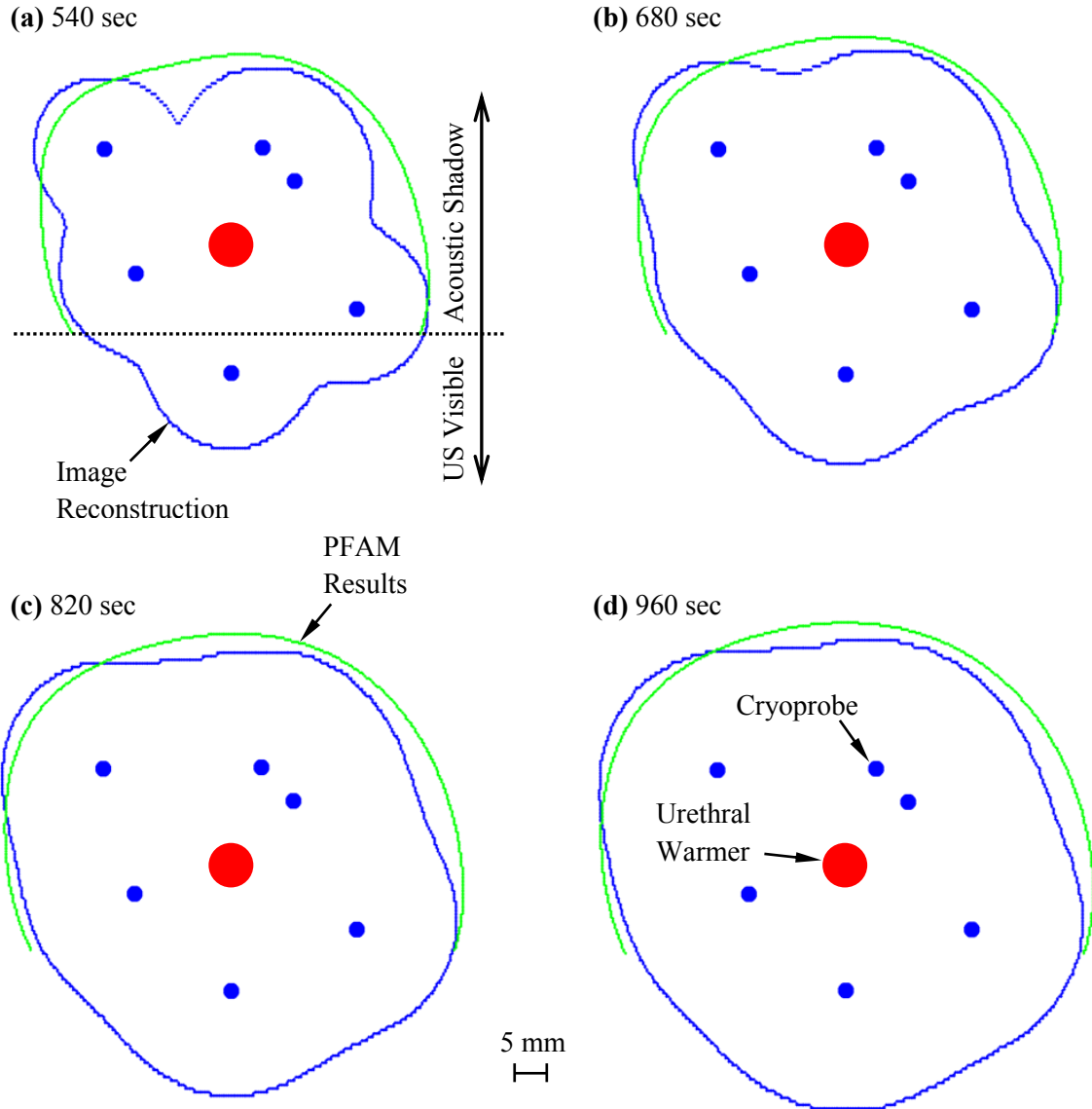


Figure 3.6: Comparison between PFAM estimation for the 0°C isotherm (green curve) and freezing-front reconstruction from experimental results (blue curve) for Case C, where the PFAM results are only presented within the simulated acoustic shadow area.

Table 3.2: Summary of freezing front mismatch between the PFAM, TFRM, and experimental results

	Analysis Method	Elapsed time, s	Hausdorff distance, mm	
			ΔS_{max} , Eq. (7)	ΔS_{avg} , Eq. (8)
Case A (Fig. 3.4)	PFAM	420	4.5	1.1
	PFAM	760	2.8	0.8
	PFAM	1100	1.9	0.5
	PFAM	1400	1.9	0.5
Case B (Fig. 3.5)	PFAM	430	8.6	1.9
	PFAM	650	6.3	1.4
	PFAM	870	5.7	1.2
	PFAM	1000	5.3	1.1
Case C (Fig. 3.6)	PFAM	540	8.8	1.6
	PFAM	680	4.5	1.1
	PFAM	820	3.6	1.0
	PFAM	960	3.0	0.9
Case D, $T=0^{\circ}\text{C}$ (Fig. 3.7)	TFRM	N/A*	15.2	8.1
	TFRM+PFAM	N/A*	2.9	0.9
Case D, $T=-45^{\circ}\text{C}$ (Fig. 3.8)	TFRM	N/A*	10.1	5.3
	TFRM+PFAM	N/A*	3.1	0.1

* Optimal planning based on computation means described in [34]

Note that the PFAM is applied only after the merge of the frozen regions around the individual cryoprobes into a continuous frozen region around the urethral warmer, which is typical in clinical practice at an advanced stage of the procedure. The planned cryoprobe layout in clinical practice is aimed at creating such a continuous region, otherwise significant areas within the prostate would be left untreated [56, 26, 27]. Further note that neither of the cryoprobe layouts is considered optimal for prostate cryosurgery, which is only selected for a proof-of-concept study. Hence, while the principles of acoustic shadowing have been maintained

consistent with clinical practice, the actual selection of the visible portion of the freezing front is somewhat arbitrary.

From the results displayed in Figs. 3.4-3.6 and Table 3.1, the following observations can be made:

- (1) The best match between PFAM results and experimental data is obtained for the symmetric Case A. As could be expected, the quality of this match degrades with the increased complexity of the cryoprobe layout.
- (2) Regardless of the specific cryoprobe layout, the match between PFAM results and experimental data improves as the freezing process progresses. This trend can be explained by the observation that the frozen region becomes smoother with less concaved regions with the progression of freezing.
- (3) Regardless of the specific configuration tested, an average Hausdorff distance of less than 2 mm is found after 400 s., and less than 1.2 mm after 1000 s. This value is equal or better than the typical uncertainty in ultrasound imaging, which suggests that the PFAM is adequate for clinical operation when a real-time application is developed.

In order to put the above observations in the right context, estimating the freezing front location in the acoustic shadowed area represents an unmet need. The PFAM represents an alternative approach to meet this need, and real-time operation appears feasible. However, reducing the PFAM to clinical practice requires further development, and the current study is aimed only at developing a low computation-cost method to meet that need. Reducing this method to practice can take advantage on a recently developed method for real-time segmentation of the visible portion of the frozen region [65].

3.3.2 Computer validation of the integrated PFAM+TFRM method

While the PFAM has shown its effectiveness in approximating the freezing-front location in areas where imaging analysis may prove ineffective, temperature-field reconstruction within the frozen region calls for additional computation measures. In particular, the location of lethal-temperature isotherm is often desired but no physical artifact can serve as its indicator, which calls for the proposed integrated method to be validated with robust bioheat transfer simulation

tools. For this purpose, ANSYS is selected to generate a benchmark case consistent with a pervious study [34] (Case D), which is based on eight cryoprobes and a urethral warmer. The simulated domain is assumed infinite from heat transfer consideration, having an initial temperature of 37°C. All cryoprobes are assumed to cool simultaneously from to -145°C in 30 s (simulative of Argon-based cryoprobes), while the urethral warmer is maintained at 37°C throughout the simulation. Thermophysical properties used in the current analysis are listed in Table 3.1.

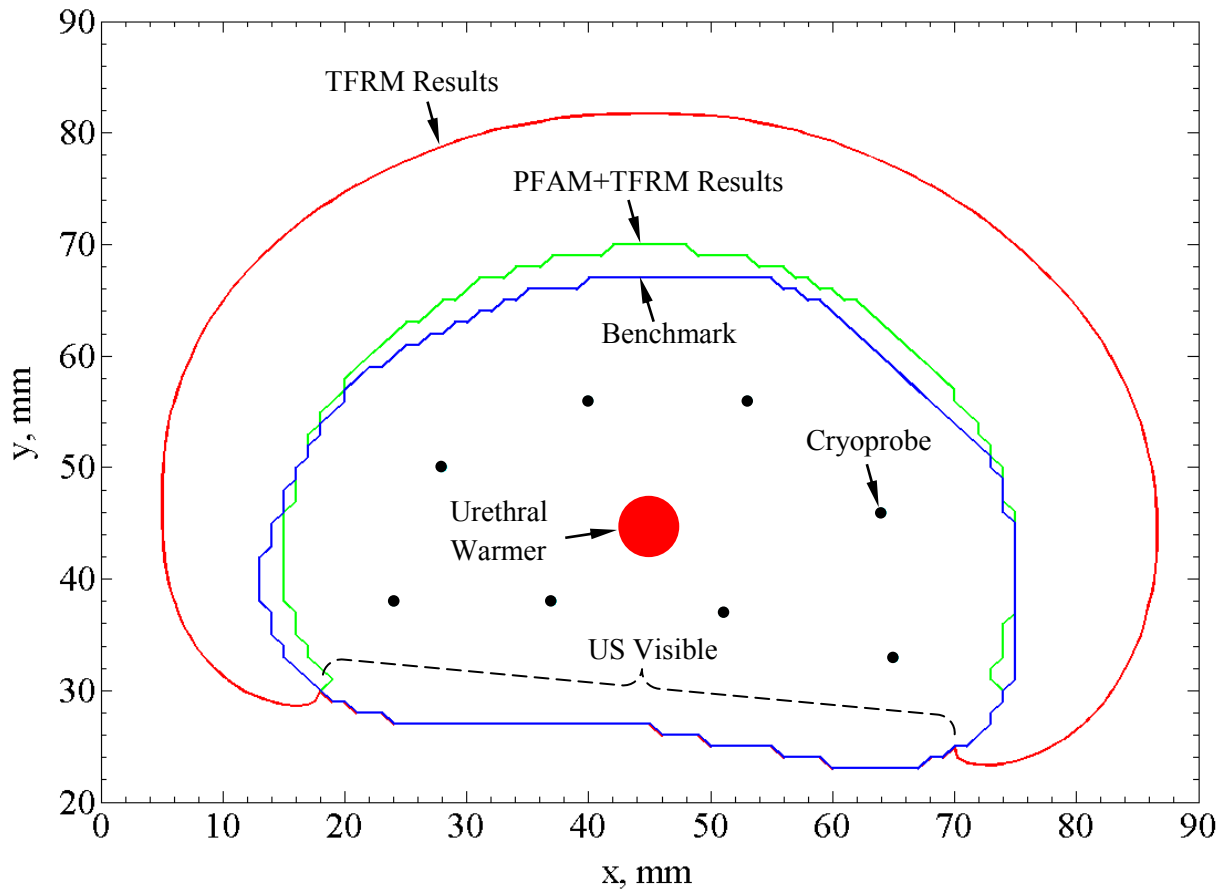


Figure 3.7: Comparison of a benchmark generated with finite-elements analysis (ANSYS) and the estimated location of the freezing front (0°C isotherm) using TFRM, with and without integration with PFAM (Case D in Table 3.2).

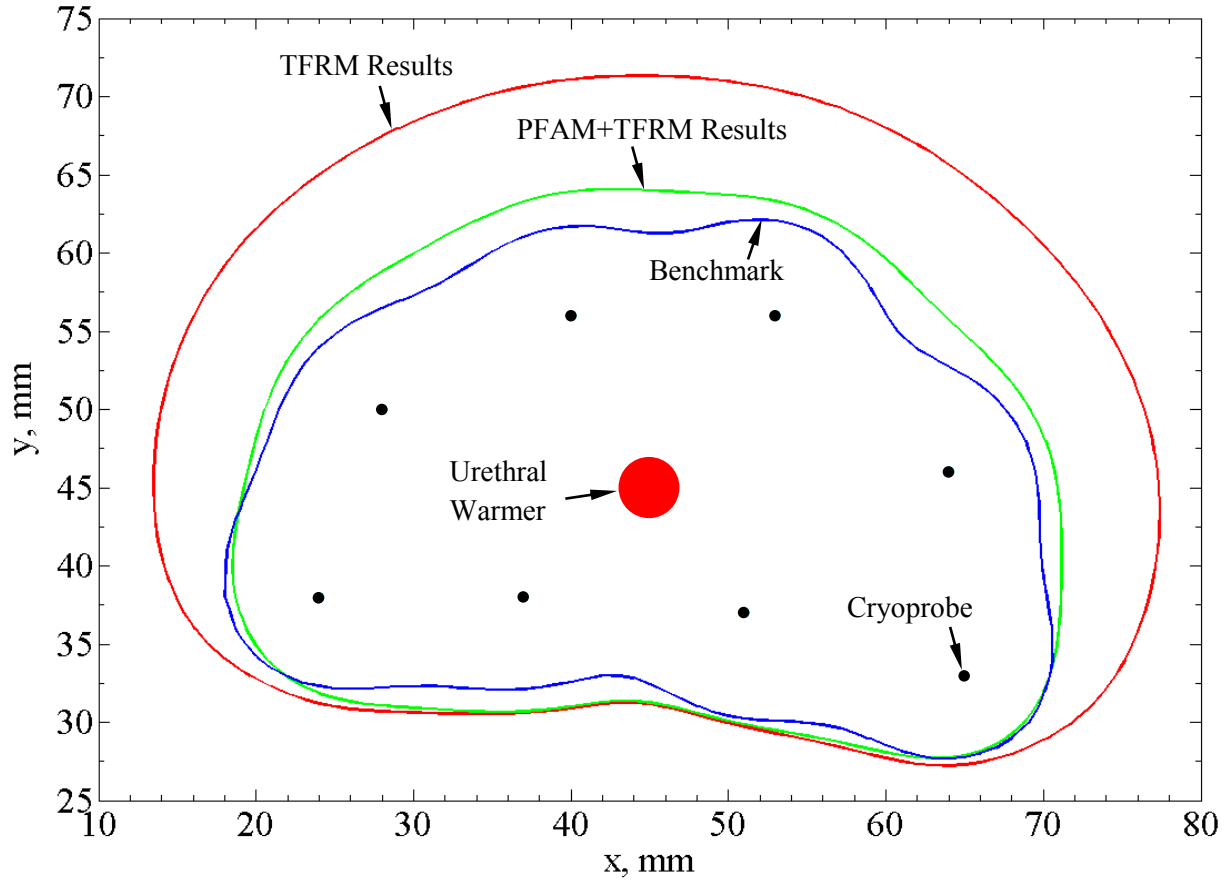


Figure 3.8: Comparison of a benchmark generated with finite-elements analysis (ANSYS) and the estimated location of the lethal-temperature isotherm, -45°C using TFRM, with and without integration with PFAM (Case D in Table 3.2).

Validation results for the integrated PFAM and TFRM method are displayed in Figs. 3.7 and 3.8, with mismatch distances summarized in Table 3.2. It can be seen from Fig. 3.7 that the PFAM dramatically improves the prediction of the freezing front location (the jagged nature of the curves is consistent with the 1 mm grid used for TFRM evaluation). The maximum and average mismatch distances for the TFRM alone are 15.2 mm and 8.1 mm, respectively. However, the maximum and average mismatch distances for the combined PFAM+TFRM are 2.9 mm and 0.9 mm, respectively. Taking into account an ultrasound analysis uncertainty of 1 mm to 2 mm, the combined PFAM+TFRM method appears to be a clinically relevant mathematical method for real-time analysis.

The maximum and average mismatch distances for the lethal temperature isotherm are 10.1 mm and 5.3 mm, respectively, when only TFRM is used solely. However, when the integrated

mathematical method is applied, these values decrease to 3.1 mm and 0.1 mm, respectively. These results appear quite relevant for the development of computer-assisted tools for cryosurgery, especially when emphasizing that they are based on only about one third of the freezing-front location (PFAM), while neglecting the inertia term in the bioheat transfer process (TFRM).

The integrated method has been solved using MATLAB on an Intel® Quad Core™ i7 machine with 9 GB RAM, running at 3.07 GHz. The PFAM is computationally inexpensive, which required less than 0.5 s for any of the cases presented above. As described in [34], the TFRM is solved by applying a sparse matrix format and internal solvers for efficiency in calculations, with a typical runtime under 3 s. These runtime numbers represent non-optimized computation frameworks, where GPU implementation is likely to reduce the overall runtime to milliseconds [66]. Hence, the integrated numerical method is relevant for clinical practice and warrants further development. For example, once a clinician marks the location of the cryoprobes and freezing front at a few points along its visible portion, a complete temperature reconstruction can be obtained in real time.

3.3.3 Experimental validation of the thermal history of the PFAM+TFRM method

Thus far, method validation has been demonstrated for the ability to predict the freezing front location based on experimental results, and for the ability to predict the lethal-temperature isotherm based on computer simulations. The discussion now turns to the ability to estimate the thermal history at preselected points in space, with Case B as a test case. Temperature measurements were obtained with T-type thermocouples ($\pm 0.5^\circ\text{C}$ uncertainty), as illustrated in Fig. 3.5. Comparison results are presented in Fig. 3.9 starting at 400s, after which the temperature sensors became embedded in the frozen region. Differences between predicted and measured temperatures for TC₁ range between 6°C at 400 s to 3.6°C at 850 s. Temperature differences for TC₂ range between 2°C at 400 s to 0.8°C at 850 s. The main reason for the lower-quality of temperature predictions for TC₁ is that it is located further than TC₂ in relation to the observed freezing front. When the magnitude of 6°C is considered, it should be noted that (i) no real temperature measurement means are available during cryosurgery in the respective areas, and (ii) the maximum temperature variation in the domain can become two orders of magnitude larger than that value.

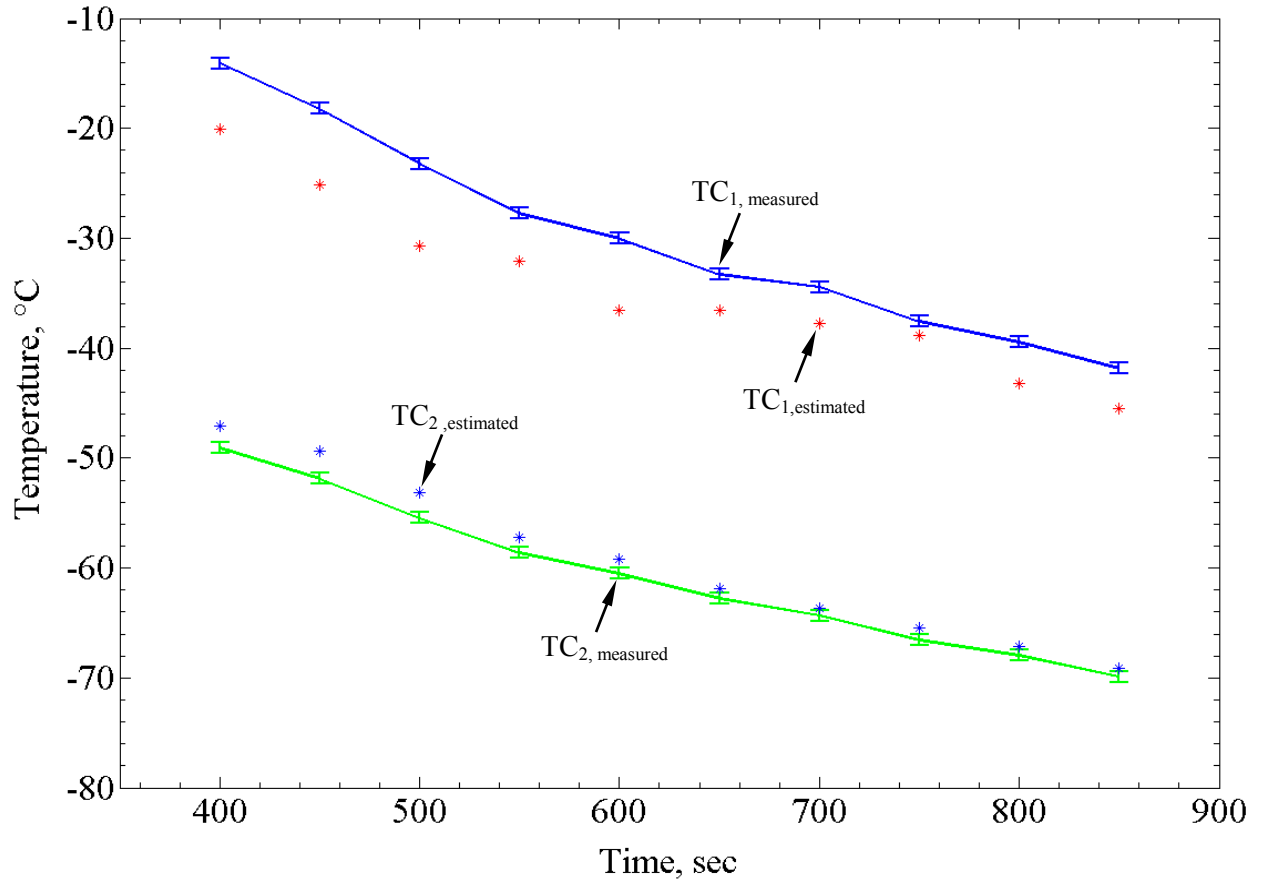


Figure 3.9: Comparison of measured and estimated temperatures, using an integrated PFAM and TFRM method, where sensor locations are illustrated in Fig. 3.5.

3.4 Summary

The objective of the study presented in this chapter is to reconstruct the temperature field during cryosurgery in the presence of an acoustic shadow, which would be created during ultrasound imaging. To achieve this goal, a new method (PFAM) has been developed. The inputs for PFAM are: partial location of freezing front extracted from medical imaging, cryoprobe location and their history. PFAM was validated against experimental data previously obtained in BTTL. The average mismatch between the predicted (approximated) location of the freezing front and the measured location of the freezing front was found to be less than 2 mm.

Another objective of this chapter is to integrate PFAM with TFRM in order to create a computationally inexpensive hybrid (PFAM + TFRM). This unified framework is then used to reconstruct the temperature field in one of case studies presented in the previous chapter. The

results show a large decrease in the mismatch between predicted temperature field and benchmark. The time required for execution of the hybrid method is shown to be almost equal to time required for TFRM alone which means computational cost of PFAM is low.

The last objective for the chapter is to experimentally verify the hybrid method in 2D by comparing estimated thermal history at pre-selected locations with thermocouple measurements. The difference between estimated and measured temperatures is found to be less than 10°C. While in Chapter 2, the mathematical basis for TFRM is presented for 2D, this chapter presents its integration into a hybrid method, which is then experimentally verified. Given the fact that no other methods are currently used to evaluate the actual temperature distribution during cryosurgery, the hybrid framework represents a very promising development in real-time monitoring.

Chapter 4: Extending the Hybrid Method (PFAM + TFRM) to 3D

The main objective for the study presented in the current chapter is extension of the work demonstrated in the previous chapter. The experimentally verified hybrid approach (PFAM + TFRM) is extended to 3 dimensions (3D) as a proof-of-concept. The temperature fields predicted by the numerical method are compared with a computerized benchmark generated using ANSYS [51, 50].

Extending the framework from 2 dimensions to 3 dimensions represents a large increase in computational complexity. To implement the hybrid (PFAM + TFRM) method in 3D using data structures and linear system solvers used for 2D cases becomes untenable because of the very large memory footprint required. To resolve these issues, the focus of this chapter is to create an efficient implementation of the hybrid method in 3D.

4.1 Problem Definition and 3D Implementation

The mathematical formulation used previously is now extended for 3D. Figure 4.1 displays a 3D representation of the prostate model for the purpose of problem illustration.

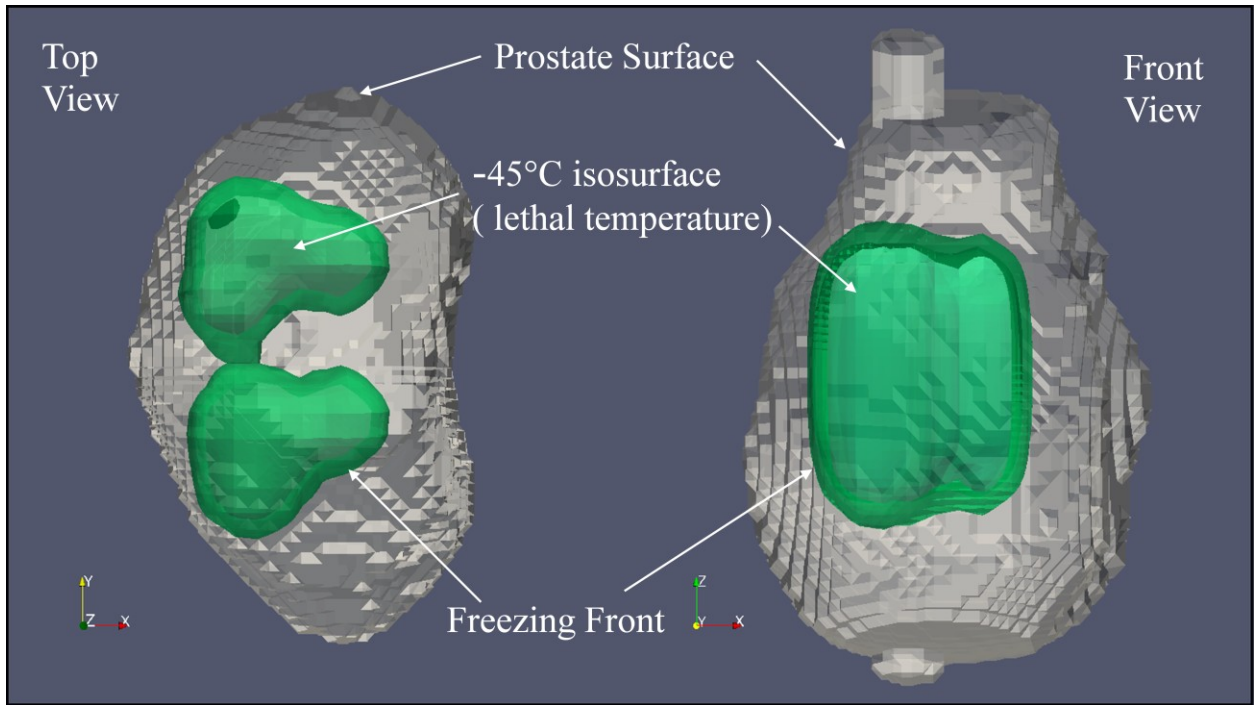


Figure 4.1: Top view and front view of a representative numerical model of the prostate (gray) and volume of tissue (green) below lethal temperature (-45°C)

The extension of the numerical method presented in the previous chapter from 2D to 3D creates a number of problems. The inputs to the problem being solved are: (i) temperature data from the cryoprobes, (ii) temperature data from the urethral warmer, and (iii) imaging data from ultrasound. The main challenge in extending the numerical method to 3D is in the dramatic increase in the size of the computational grid. The numerical method presented in the previous chapters (TFRM + PFAM) used a uniform grid of 90×90 points with a space interval of 1 mm. This meant that the computational domain consisted of 8100 grid points. The 3D case considered here consists of a uniform grid of $60 \times 60 \times 60$ points with a space interval of 1 mm. The computational grid consists of 216,000 grid points. This represents a massive increase in the size of the computational effort required to reach the solution. When Eqs. (3.6) and (3.7) are discretized using the numerical grid described above, the resulting system matrix for the linear system of equations has ~ 47 billion elements. Each element of the matrix requires at least 1 byte of memory resulting in the memory footprint of the problem is around 45 GB. This is a prohibitively large amount of memory and thus out of scope for most of the computers available today.

To solve this problem of memory footprint, a different type of data structure is used to store the system matrix. The system matrix is a banded matrix with seven diagonals with the majority of its elements being zero. This is also known as a sparse matrix. In numerical analysis, a sparse matrix is a matrix in which most of the elements are zero [67]. In the case of a sparse matrix, substantial memory requirement reductions can be realized by storing only the non-zero entries. Depending on the number and distribution of the non-zero entries, different data structures can be used and yield huge savings in memory when compared to standard approach (storing all element locations and their values). Sparse matrix systems also need special solvers. The techniques used for dense matrix systems are inefficient to solve sparse systems. The MATLAB solver used in this study automatically chooses the correct algorithm required for the system being solved [68]. As this study is a proof-of-concept, the MATLAB solver is considered sufficient for the exercise.

The 3D simulation inherently suffers from the problem of displaying the results of the temperature reconstruction on 2D media. To get around this problem, the results of the 3D simulations are presented on a cross section by cross section basis. The cross section is in the x-y plane and successive cross sections along the z-axis are displayed. The results of the numerical

method are evaluated using Eqs. (3.8) and (3.9). As the Hausdorff distance uses the Euclidean norm, the calculations for maximum mismatch (ΔS_{max}) and average mismatch (ΔS_{avg}) are similar to the distance calculations in the previous chapter. The only difference in the calculation here and the previous chapter is that in this case, the Euclidean norm is 3D instead of 2D (Chapter 3).

4.2. Results and Discussion

The 3D-extended unified numerical method (TFRM+ PFAM) is validated here against a transient benchmark case obtained with the finite elements commercial code ANSYS. This benchmark solution was obtained based on prostate contours sectioned from ultrasound imaging [33], subject to the following parameters and conditions:

- (1) Eight cryoprobes are used simultaneously;
- (2) The cryoprobes are cooled from 37°C to -145°C in 30 sec, simulative of Argon-based cryoprobes;
- (3) The cryoprobe layout is computer generated, using a planning algorithm known as “bubble packing” [25], with the match between the 0°C isotherm and the organ contour as a planning criterion; and,
- (4) The urethra is maintained at 37°C throughout the procedure, simulative of the commonly applied urethral warmer.

The cryosurgical procedure is considered complete when the mismatch between simulated frozen volume and targeted prostate volume reaches minimum value.

4.2.1. Temperature Field Reconstruction Method (TFRM) in 3D

Using the Trans-Rectal Ultra-Sound Transducer (TRUST), the extent of freezing is monitored at one cross-section at a time, while the transducer is axially moved to scan the prostate. Figure 4.2 shows the numerical benchmark along with direction of field of view of TRUST. Currently most prostate cryosurgical procedures use 2D ultrasound. This results in ultrasound imaging data being available only from one cross-section at a time. Recall that the phenomenon of acoustic shadowing further affects the imaged target region (Chapter 3). The outcome of TRUST imaging is that the extent of freezing is known only partially and only at a single cross-section at a time.

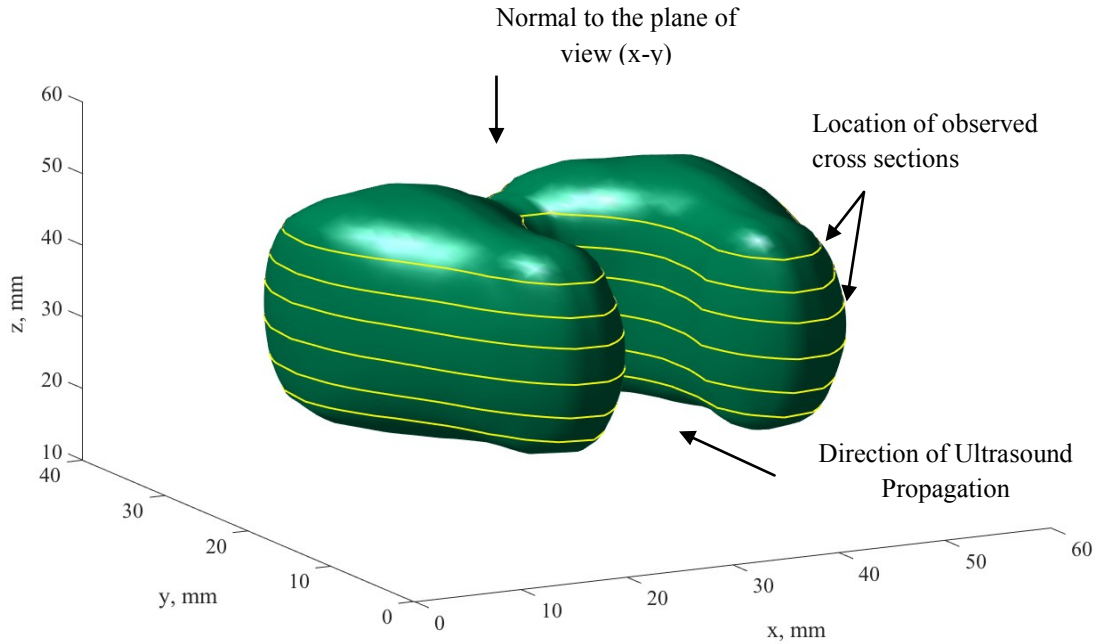


Figure 4.2: A schematic of full scale transient simulation used as a benchmark at a representative time interval ($t = 180$ seconds) along with observed cross sections (yellow curves)

The numerical experiments carried out in this study were divided into three general cases. The first general case (Case A) represents an ideal case where the location of the freezing front is assumed to be completely known (as could be extracted from MRI or CT imaging) in 3D. The location data is then used as an input to TFRM. Case A represents an ideal scenario, and is presented here to help in qualitatively understanding of the effect of decreasing knowledge of freezing front on the predictions of TFRM. Initially, the complete location of the freezing front is assumed to be 'visible' to the TRUS transducer. Practically in this study, this is achieved by sampling the freezing front at 30 cross-sections, n , along the z -axis. In the successive iteration, the freezing front is sampled only at 15, 8, 4, and 1 equidistant cross-sections along the z -axis. Thus, the series of studied cases advances towards more practical clinical scenarios.

Figure 4.3 shows the locations of the -45°C isotherm after 180 seconds of simulation at 6 different cross sections along the z -axis. The locations of these cross sections are denoted by the yellow curves in Fig. 4.2. Predicted locations of lethal isotherm are compared to the benchmark location of the lethal isotherm. Similarly, in Fig. 4.4, the predicted location of -22°C isotherm is displayed for different number of cross sections considered. Fig. 4.3 displays the location of the so-called 'lethal isotherm' which is -45°C after 180 s of simulation, for various cross section

sampling numbers. The lethal isotherm locations are shown at a depth of $z = 35$ mm in effort to be represent the overall technique performance, while similar behavior can be observed in other cross sections.

Table 4.1: Summary of average mismatch (ΔS_{avg}) and max mismatch (ΔS_{max}) between benchmark and TFRM predicted -45°C and -22°C isotherm at $t = 180$ s

CASE A (TFRM + No acoustic shadowing)	Cross- Section Observed	Hausdorff distance, mm	
		ΔS_{max}	ΔS_{avg}
T = - 45°C (Fig. 4.5)	n = 30	1.8	0.4
	n = 15	1.9	0.4
	n = 8	2.6	0.7
	n = 4	3.7	1.1
	n = 1	5.6	1.4
T = - 22°C (Fig. 4.6)	n = 30	2.2	0.3
	n = 15	2.4	0.3
	n = 8	4.0	0.8
	n = 4	5.1	1.4
	n = 1	8.4	2.8

From the results displayed in Table 4.1 and Figs. 4.3-4.4, the following observations can be made for case A:

- (1) The best match between TFRM and benchmark is when $n = 30$. As could be expected, the quality of this match degrades with the decreased proportion of observed cross sections.
- (2) Regardless of the specific configuration tested, an average Hausdorff distance of less than 2 mm is found for -45°C isotherm. Similarly, for -22°C isotherm the average mismatch is less than 3 mm for all cases

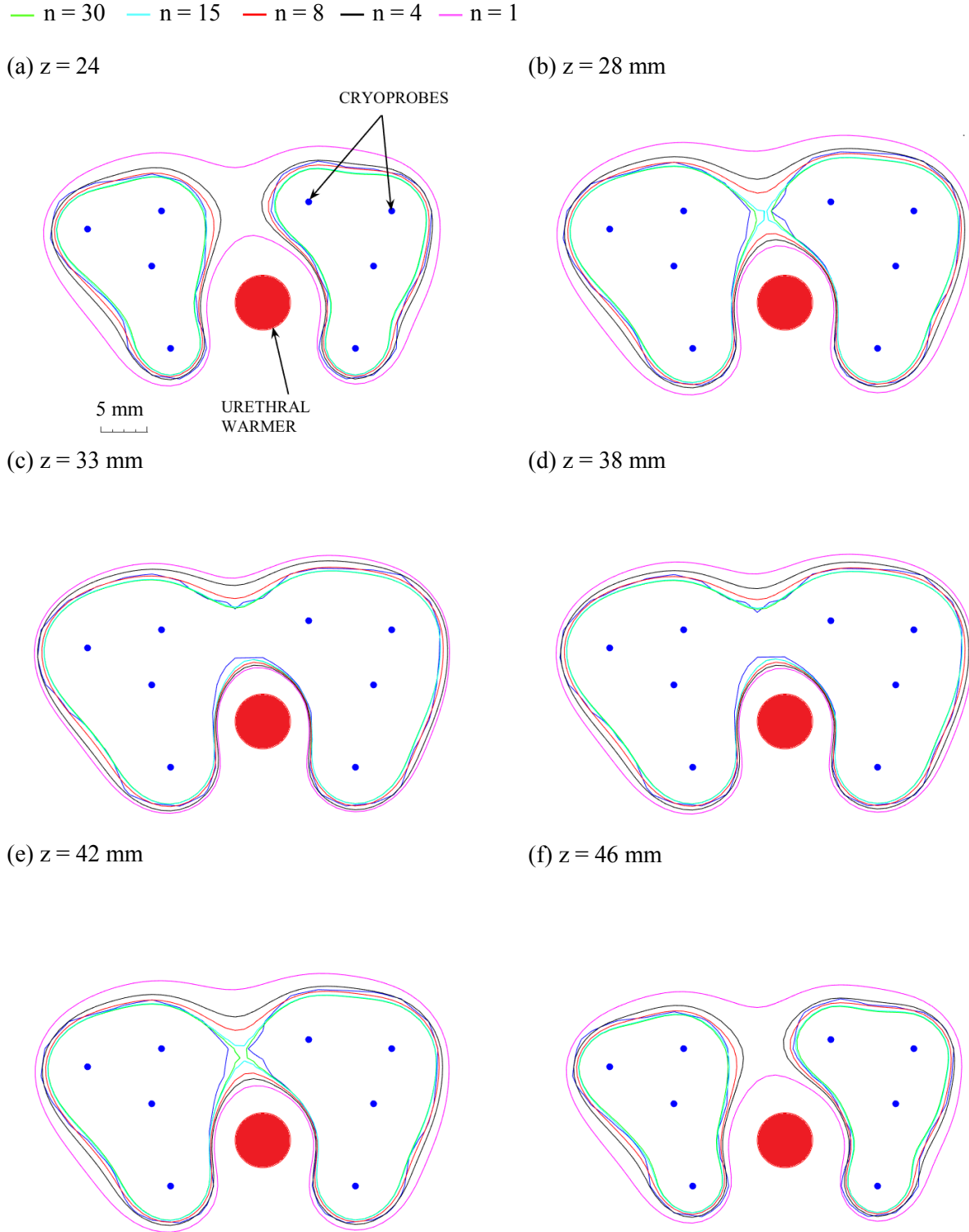


Figure 4.3: Comparison between TFRM estimation and the benchmark (blue) for the -45°C isotherm, for Case A at $t = 180$ s for $n = 30$ (green), $n = 15$ (cyan), $n = 8$ (red), $n = 4$ (black), and $n = 1$ (magenta)

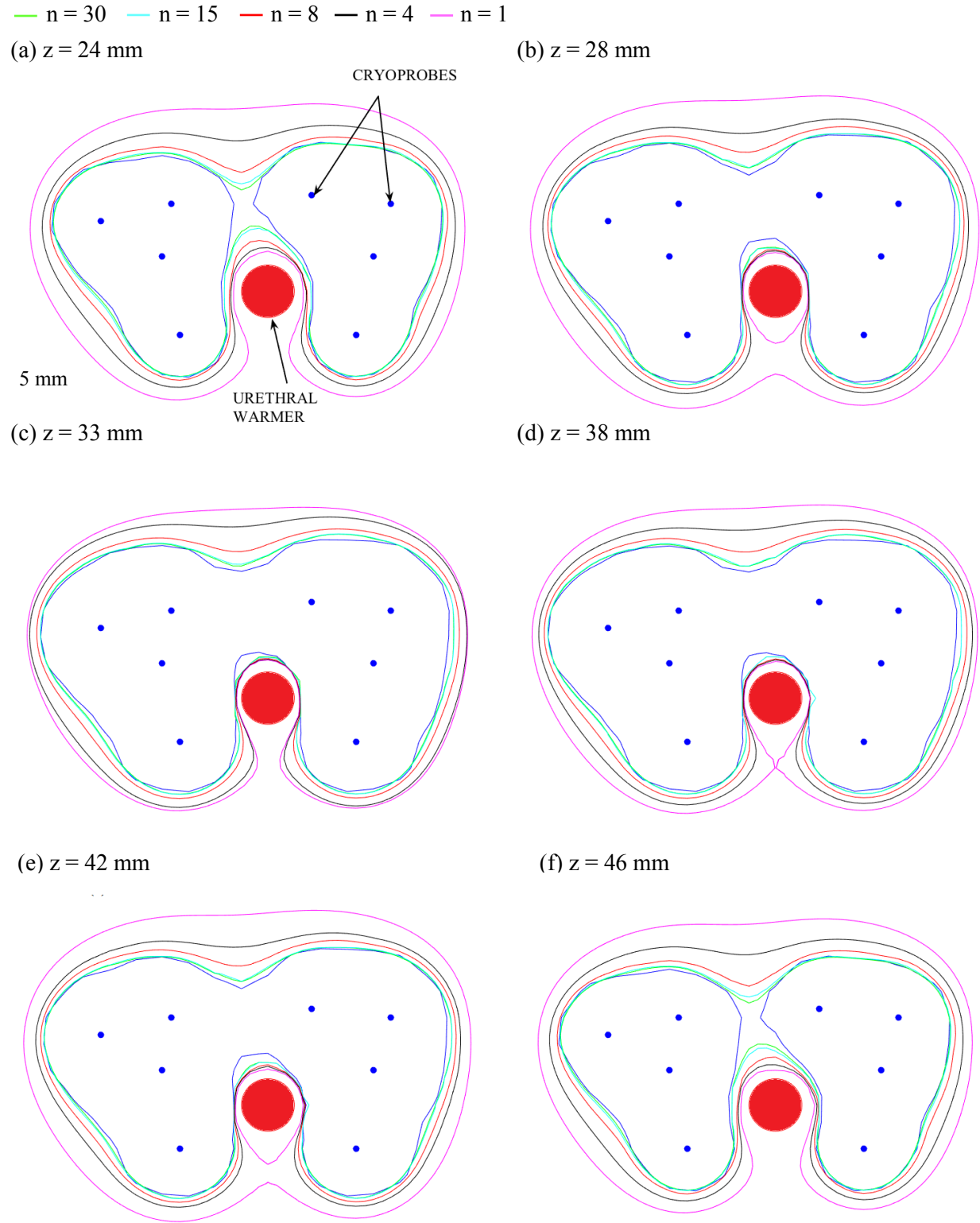


Figure 4.4: Comparison between TFRM estimation and the benchmark (blue) for the -22°C isotherm for Case A at $t = 180$ s for $n = 30$ (green), $n = 15$ (cyan), $n = 8$ (red), $n = 4$ (black), and $n = 1$ (magenta)

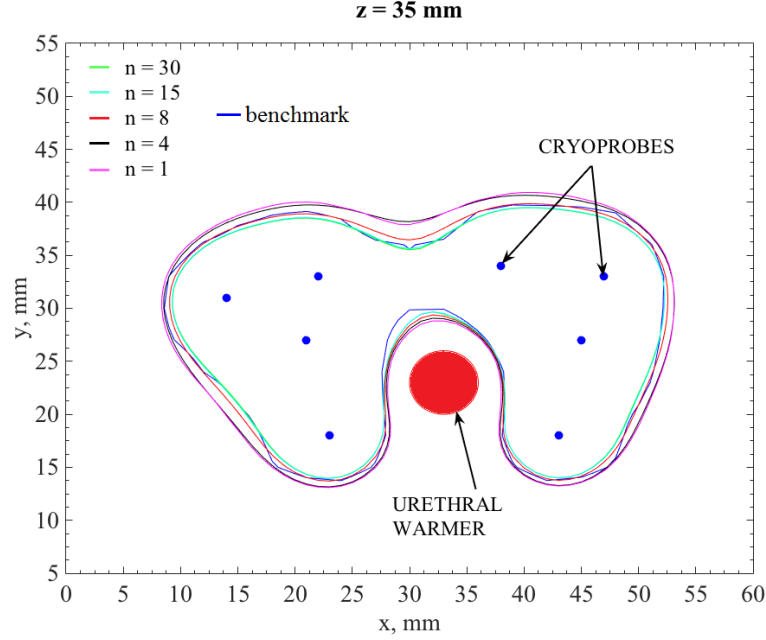


Figure 4.5: Comparison between TFRM estimation for the -45°C isotherm and benchmark results for various number of cross-section datasets after 180 seconds of simulation.

For the rest of the analysis, only the results at $z=35$ mm cross section are going to be displayed as a representative cross section. It can be seen from Fig. 4.7 that the mismatch between the benchmark lethal isotherm and the location of predicted lethal isotherms by TFRM increases with decreasing number of cross sections. The maximum distance, ΔS_{max} , between predicted and benchmark lethal isotherm locations increases from $\Delta S_{max} = 1.8$ mm for $n = 30$ to $\Delta S_{max} = 5.6$ mm for $n = 1$. Similarly, the average mismatch, ΔS_{avg} , increases from 0.4 mm to 1.4 mm, when the number of observed cross-sections decreases from $n = 30$ to $n = 1$. Figs. 4.6 and 4.7 display similar results for after 240 s and 300 s, respectively.

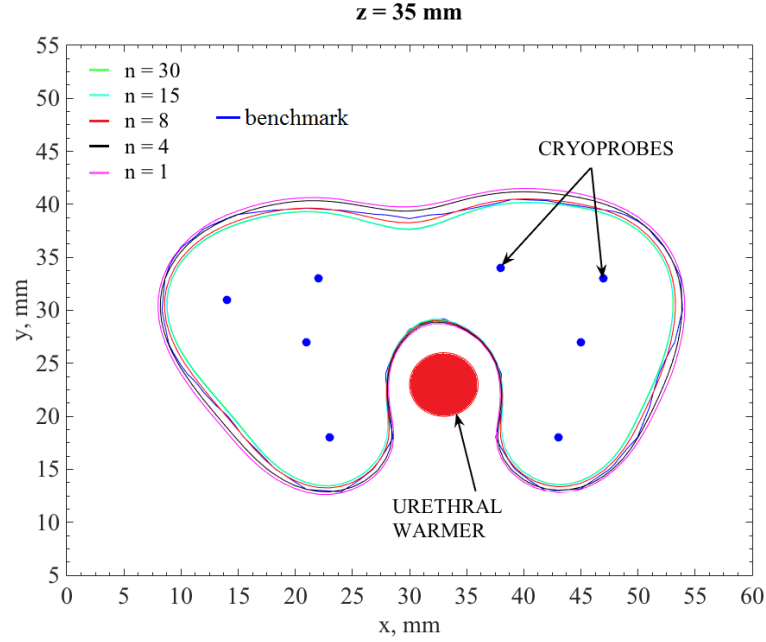


Figure 4.6: Comparison between TFRM estimation for the -45°C isotherm and benchmark (blue) for different number of cross-sections observed, n , after 240 seconds of simulation

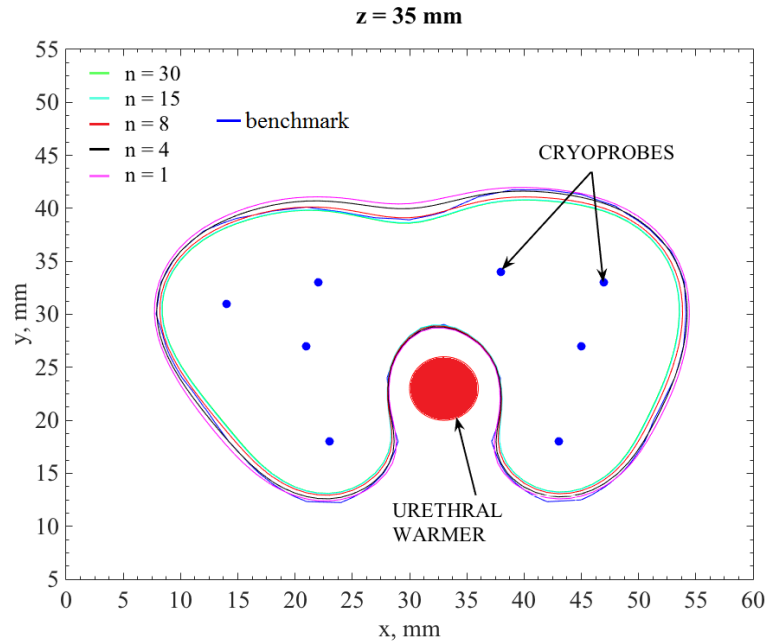


Figure 4.7: Comparison between TFRM estimation for the -45°C isotherm and benchmark (blue) for different number of cross-sections observed, n , after 300 seconds of simulation

Figure 4.6 and Fig. 4.7 illustrate the increasing match with the increased number of cross sections for three representative instants along the cryosurgery simulation.

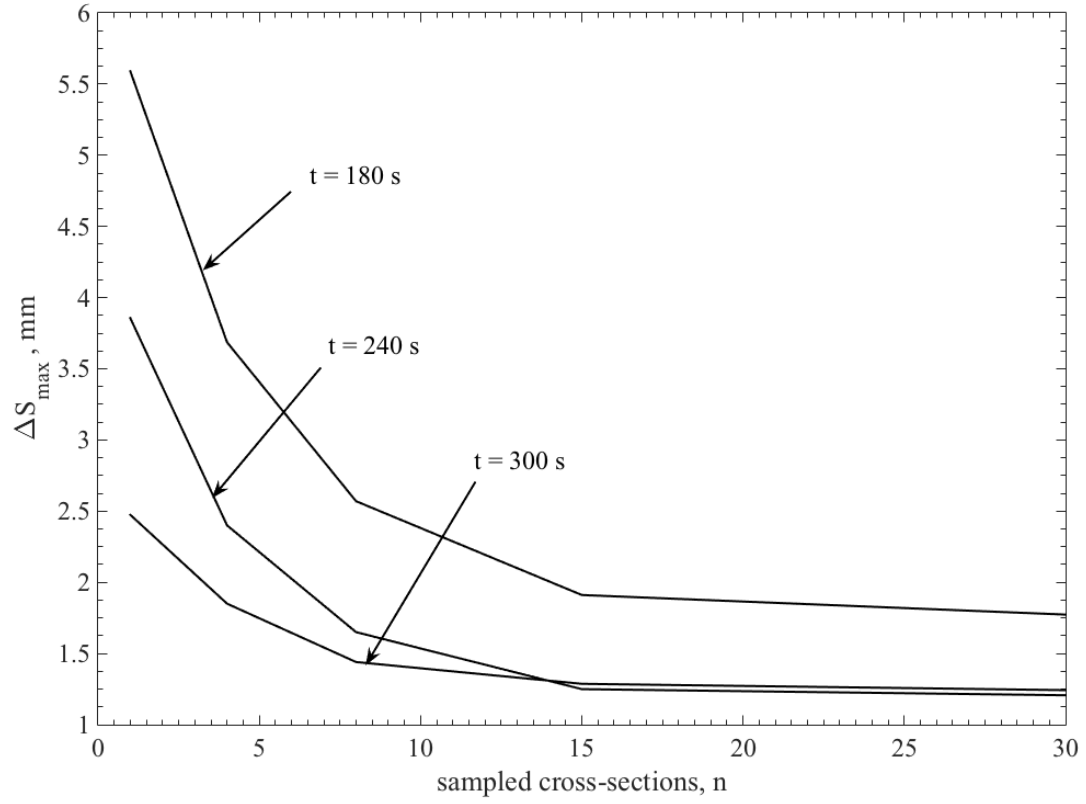


Figure 4.8: Maximum mismatch, ΔS_{\max} , between TFRM and benchmark lethal isotherm as a function of number of sampled cross-section, in a case where the entire freezing front location in the cross section is known.

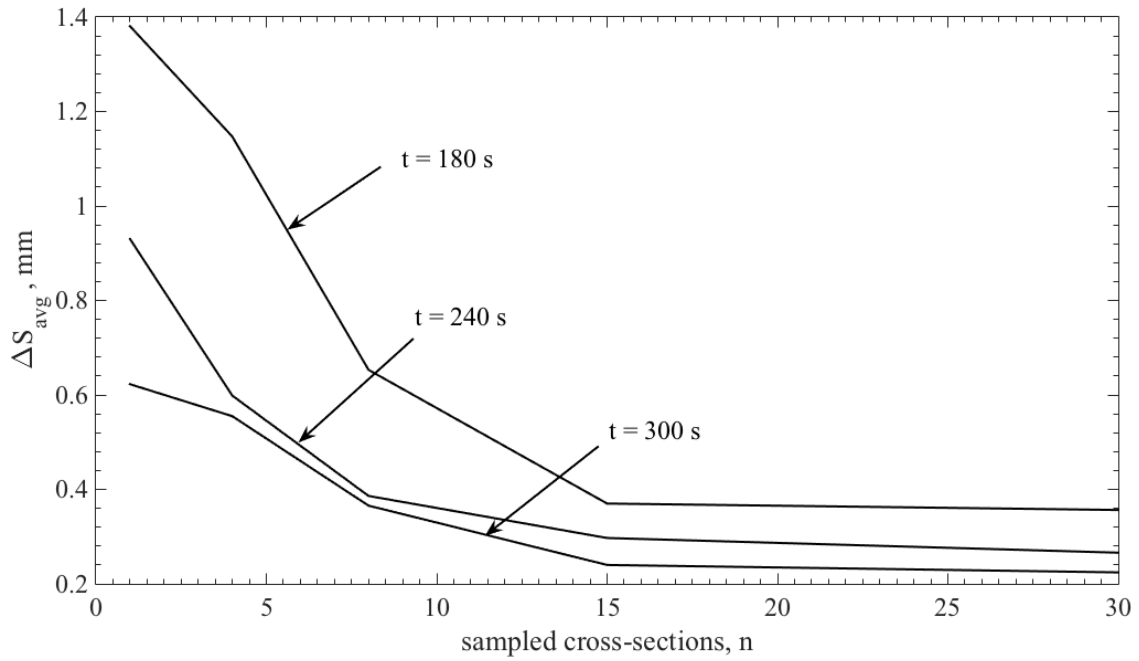


Figure 4.9: Average mismatch, ΔS_{avg} , between TFRM and benchmark lethal isotherm as a function of number of observed (sampled) cross-section, n , when entire freezing front location is assumed to be visible.

It can be seen from Figs. 4.8 and 4.9 that the maximum and average mismatches decrease with increasing number of sampled cross sections, and independently with the simulated time. These observations are consistent with observations made in the previous chapters for 2D cases.

Case B (TFRM with acoustic shadowing that would be produced in ultrasound imaging) represents a more practical scenario in which the effect of acoustic shadowing is taken into account. This means that the location of only a part of the freezing front is known by means of TRUST imaging. In Chapter 3, a procedure to computationally establish the acoustic shadowing was described and a similar approach is employed here to figure out the proportion of freezing front visible. Here, instead of just one cross section as is the case for 2D, acoustic shadowing is observed at every cross-section being sampled. This is simulative of the case when clinician moves TRUST to change the cross section being observed. Similar to Fig 4.5, Fig. 4.10 displays the locations of lethal isotherm predicted by TFRM when the freezing front location is only partially known at a depth of 35 mm.

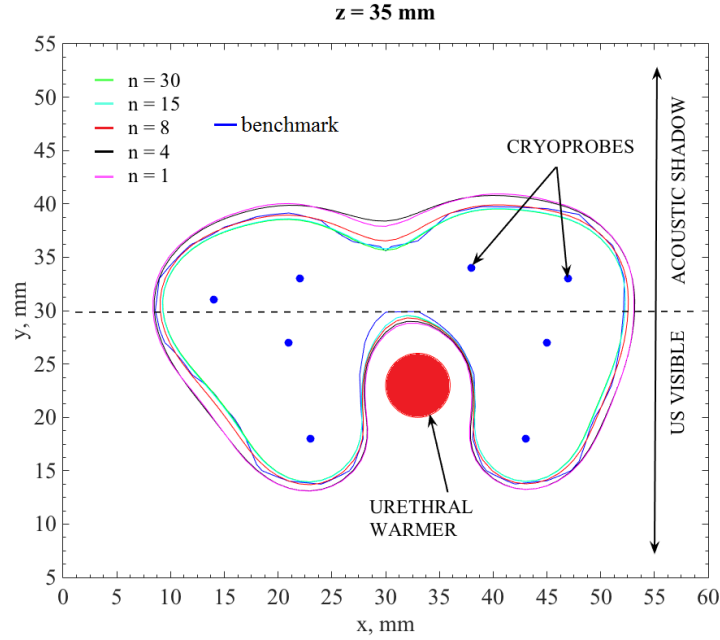


Figure 4.10: Comparison between TFRM estimation for the -45°C isotherm and benchmark (blue) for different number of cross-sections observed, n , after 180 seconds of simulation, when acoustic shadowing is taken in to account (Case B)

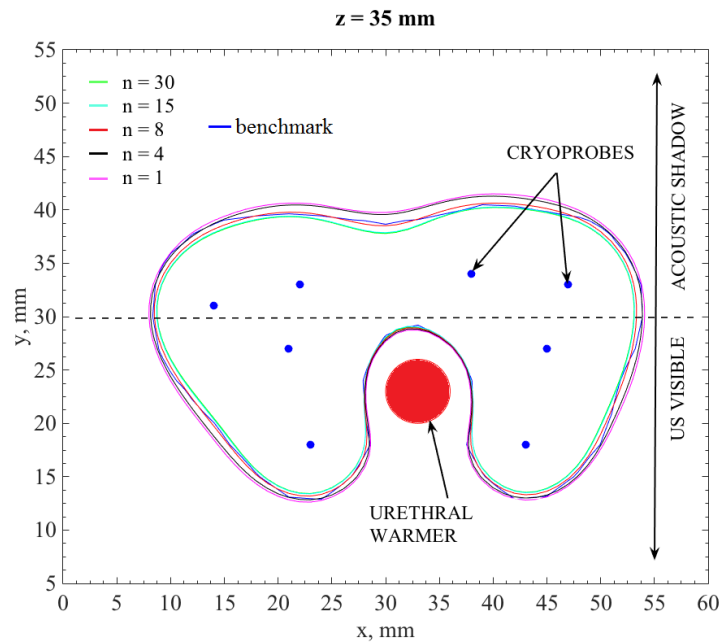


Figure 4.11: Comparison between TFRM estimation for the -45°C isotherm and benchmark (blue) for different number of cross-sections observed, n , after 240 seconds of simulation, when acoustic shadowing is taken in to account (Case B)

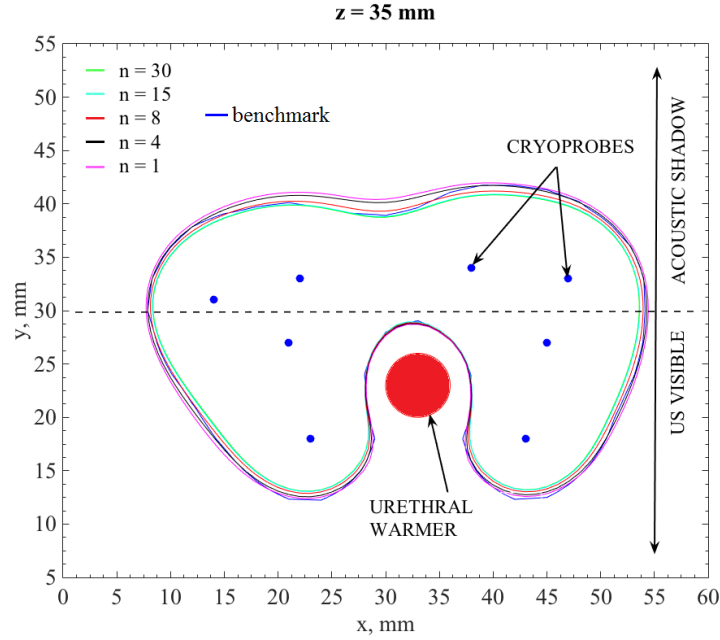


Figure 4.12: Comparison between TFRM estimation for the -45°C isotherm and benchmark (blue) for different number of cross-sections observed, n , after 300 seconds of simulation, when acoustic shadowing is taken in to account (Case B)

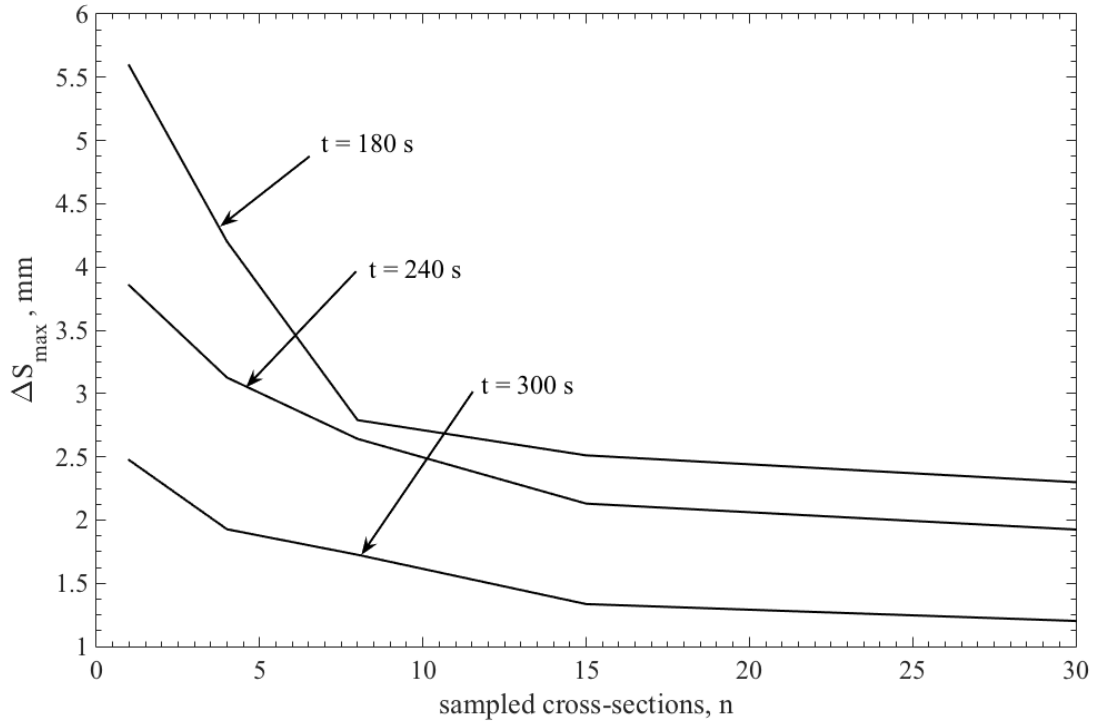


Figure 4.13: Maximum mismatch, ΔS_{max} , between TFRM and benchmark lethal isotherm as a function of number of observed (sampled) cross-section, n , when only partial information about the location of freezing front is known. (Case B)

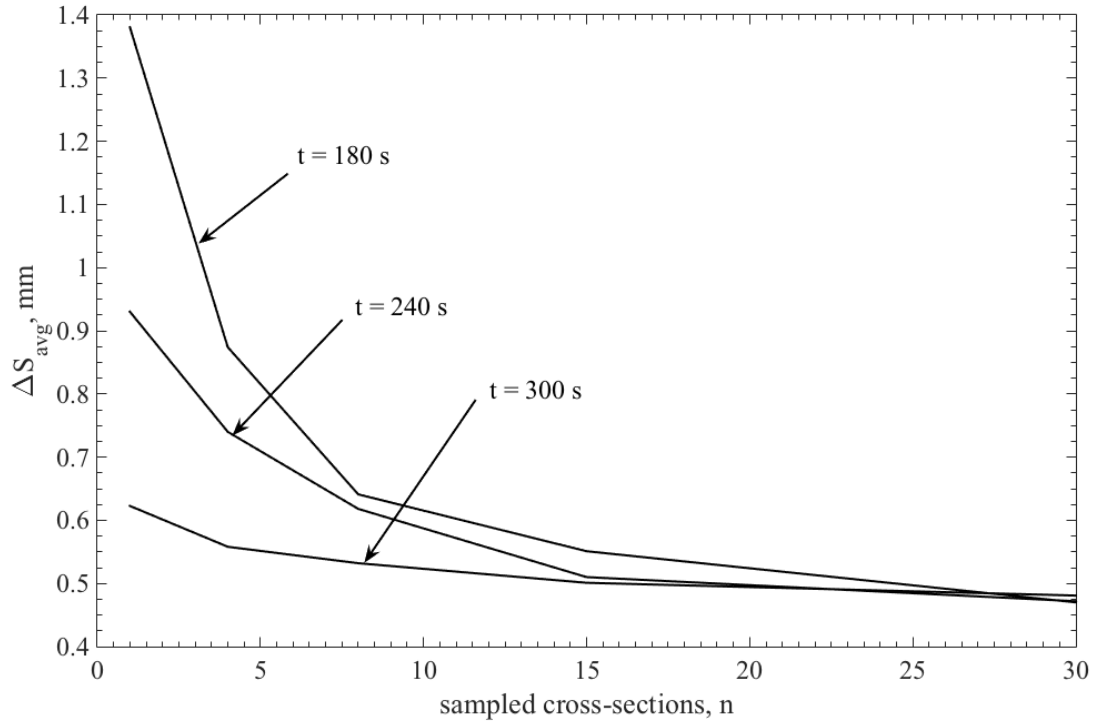


Figure 4.14: Average mismatch, ΔS_{avg} , between TFRM and benchmark lethal isotherm as a function of number of observed (sampled) cross-section, n , when only partial information about the location of freezing front is known (Case B)

Figure 4.13 displays the relationship of the maximum mismatch, ΔS_{max} , between the predicted temperature field by TFRM and the benchmark solution. The trends for the decrease in ΔS_{max} and ΔS_{avg} are similar between Cases A and B, although the actual numbers vary. The average mismatch is less than 1 mm for all cases at $t = 300$ second, at the end of the cryosurgical procedure simulation.

4.2.2. Unified Application of Potential Field Analogy Method (PFAM) and Temperature-Field Reconstruction Method (TFRM) in 3D

Case C represents a more difficult to analyze scenario, where the freezing front is supposed at a single cross-section ($n = 1$) using TRUST. Furthermore, the location of the freezing front is only partially known due the effect of acoustic shadowing. Case C is analyzed with the unified computation framework of PFAM and TFRM.

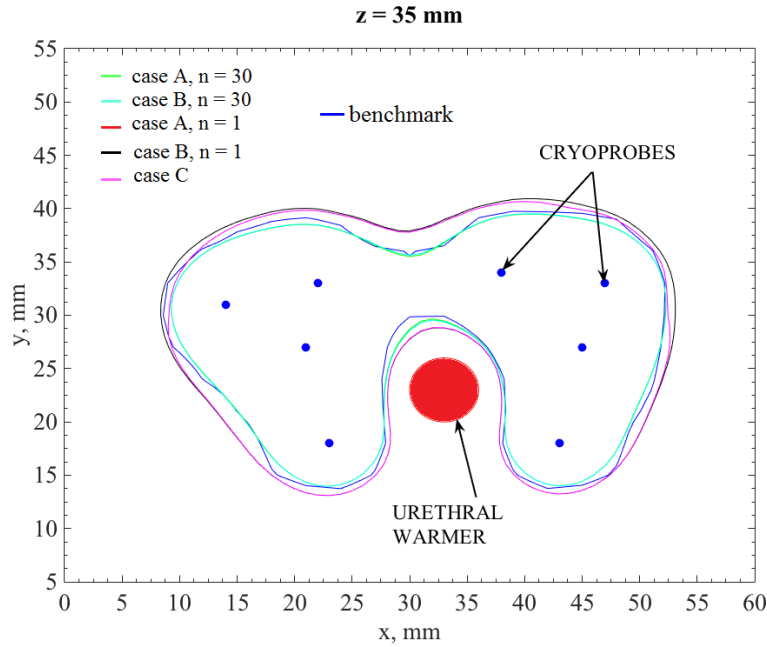


Figure 4.15: Comparison between the unified computation framework of TFRM+PFAM and the benchmark solution for the location of the -45°C isotherm, for the various cases after 180 seconds of cryosurgery simulation at a depth of 35 mm

Figure 4.15 shows the comparison between predicted lethal isotherms for Case A (TFRM), Case B (TFRM with acoustic shadowing), and Case C (TFRM with acoustic shadowing + PFAM). When TFRM is used by using the partial location of freezing front (case B, $n=1$) at time interval $t = 180$ seconds, the max mismatch, ΔS_{max} , is equal to 5.6 mm and the average mismatch, ΔS_{avg} , is equal to 1.4 mm. When PFAM is used to estimate the location of the freezing front in the acoustic shadow region the max mismatch decreases from 5.6 mm to 5.3 mm and the average mismatch decreases from 1.4 mm to 1.2 mm. This is a demonstration of the application of PFAM

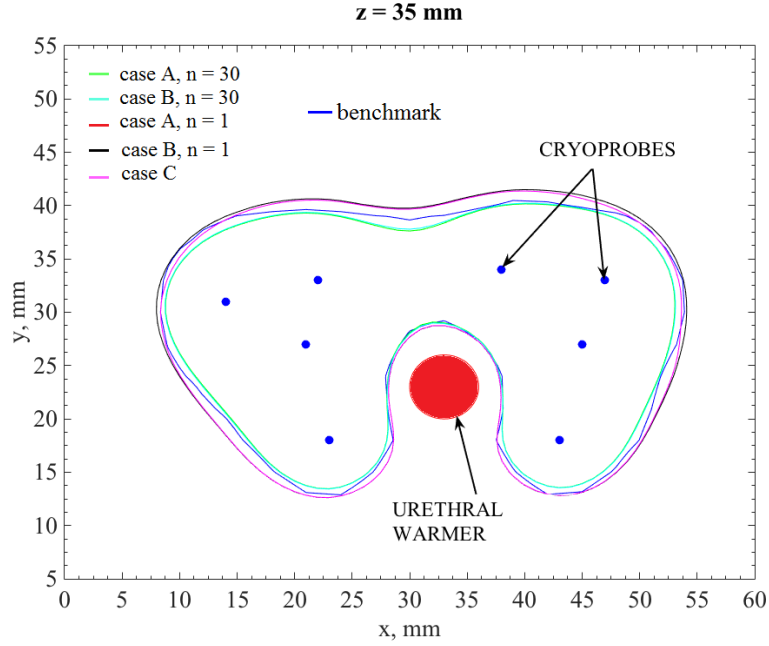


Figure 4.16: Comparison between TFRM + PFAM estimation for the -45°C isotherm and benchmark (blue) for different number of cross-sections observed, n , combined with case A, case B, and case C after 240 seconds of simulation

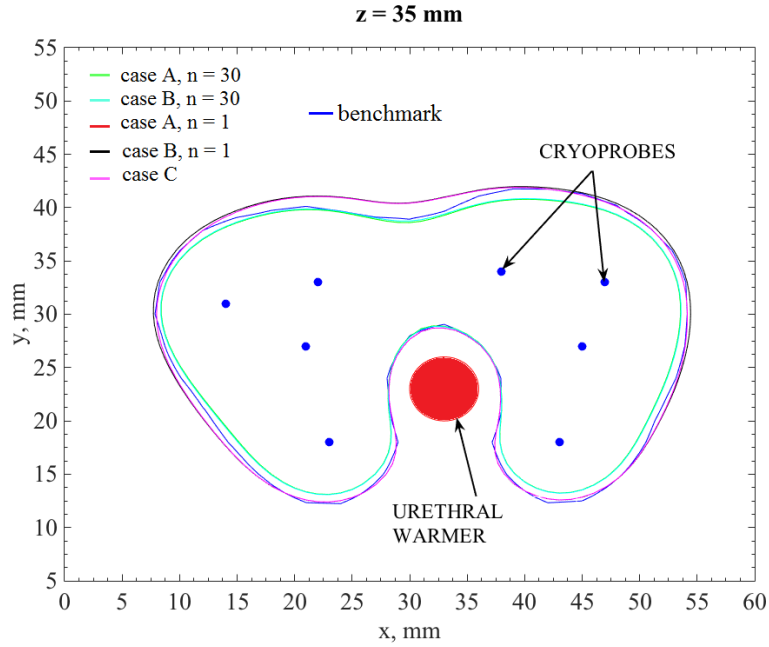


Figure 4.17: Comparison between TFRM + PFAM estimation for the -45°C isotherm and benchmark (blue) for different number of cross-sections observed, n , combined with case A, case B, and case C after 300 seconds of simulation

in improving the accuracy of temperature-field reconstruction. Figures 4.16 and 4.17 display consistent results after 240 s and 300 s of simulation, respectively. The mismatch values for all cases considered are then compiled in Table 4.2. Finally, similar calculations are also done for -22°C isotherm as it is also one of the isotherms used in planning of cryosurgery and tabulated in Table 4.3

Table 4.2: Summary of mismatch between the PFAM, TFRM for lethal isotherm (-45°C)

		Cross-Section Observed	Analysis Method	Hausdorff distance, mm	
				ΔS_{max}	ΔS_{avg}
t = 180 seconds (Fig. 4.17)	Case A	N = 30	TFRM	1.8	0.4
	Case A	N = 1	TFRM	5.6	1.4
	Case B	N = 30	TFRM	2.3	0.5
	Case B	N = 1	TFRM	5.6	1.4
	Case C	N = 1	PFAM + TFRM	5.3	1.2
t = 240 seconds (Fig. 4.18)	Case A	N = 30	TFRM	1.2	0.3
	Case A	N = 1	TFRM	3.9	0.9
	Case B	N = 30	TFRM	1.9	0.5
	Case B	N = 1	TFRM	3.9	0.9
	Case C	N = 1	PFAM + TFRM	3.9	0.9
t = 300 seconds (Fig. 4.19)	Case A	N = 30	TFRM	1.2	0.2
	Case A	N = 1	TFRM	2.5	0.6
	Case B	N = 30	TFRM	1.2	0.4
	Case B	N = 1	TFRM	2.5	0.6
	Case C	N = 1	PFAM + TFRM	2.4	0.6

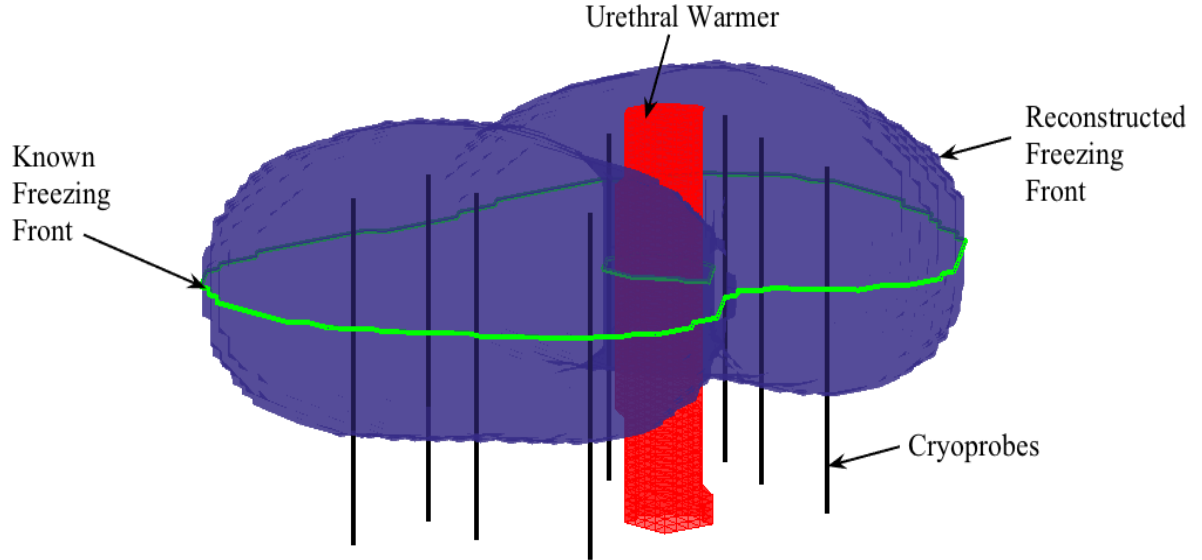


Figure 4.18: Representative illustration of 3D freezing front reconstruction based on known freezing front location on a single plane only, which could be obtained from medical imaging. Input data is considered for this problem as follows: (1) the green line represents the freezing front reconstructed from medical imaging, (2) the thermal history at the tip of the cryoprobes is known from the cryodevice, and (3) the temperature of the urethra (red) is given by the urethral warmer. The reconstructed freezing front by means of the proposed unified numerical technique is presented in violet. The quality of reconstruction is summarized in Table 4.3 and 4.4 for a variety of cases.

Figure 4.18 illustrates a scenario where the 3D freezing front location is estimated based on a known freezing front location on a single plane, with the latter simulated to be reconstructed from medical imaging. This figure signifies how the limited ultrasound data may still become instrumental in reconstructing the entire temperature field. This illustration is also representative of all three cases with $N=1$ (Figs. 4.15-4.17), where freezing front can be observed only at one cross section at a time. As shown in Table 4.2, for Case A (where full freezing front location is known using MRI or CT) and $N=1$, $\Delta S_{avg} = 1.4$ mm after simulation has run for 180 seconds. For Case C, where location of freezing front is only partially known by ultrasound means, the hybrid method (PFAM + TFRM) is used. PFAM is used to estimate freezing front location in the acoustic shadow region. The average mismatch reduces to 1.2 mm after simulation has run for 180 seconds, which demonstrates that the hybrid method leads to an improved temperature-field reconstruction. The ability of TFRM and the hybrid method to reconstruct the complete

temperature field using only a partial freezing front location at a single cross section is highly encouraging.

Table 4.3: Summary of mismatch between the PFAM, TFRM for -22°C isotherm

		Cross-Section Observed	Analysis Method	Hausdorff distance, mm	
				ΔS_{max}	ΔS_{avg}
t = 180 seconds	Case A	N = 30	TFRM	2.2	0.3
	Case A	N = 1	TFRM	8.4	2.8
	Case B	N = 30	TFRM	4.6	0.6
	Case B	N = 1	TFRM	8.4	2.8
	Case C	N = 1	PFAM + TFRM	8.3	2.7
t = 240 seconds	Case A	N = 30	TFRM	1	0.2
	Case A	N = 1	TFRM	6.6	2.3
	Case B	N = 30	TFRM	4.4	0.6
	Case B	N = 1	TFRM	6.6	2.4
	Case C	N = 1	PFAM + TFRM	6.3	2.1
t = 300 seconds	Case A	N = 30	TFRM	0.9	0.2
	Case A	N = 1	TFRM	4.8	1.8
	Case B	N = 30	TFRM	3.1	0.5
	Case B	N = 1	TFRM	4.9	1.8
	Case C	N = 1	PFAM + TFRM	4.7	1.7

4.3 Summary

In this chapter, the main objective is to extend the unified framework presented and experimentally verified in Chapter 3 to 3D. The increase in dimension of the problem causes a very large increase in computational cost and complexity. The linear system of equations for the

problem is a sparse matrix system. In a sparse matrix, most of the elements are zero. Special data structures were used in MATLAB to reduce the memory footprint of the problem. The MATLAB solver uses the appropriate sparse matrix algorithm to solve the problem. Although the typical solution time is not real-time, the study is presented as a proof-of-concept. Using a high performance compiled language such as C++ or Rust to implement the hybrid method should decrease the runtime by a wide margin.

ANSYS is used to solve the full 3D transient bio-heat transfer problem and then is used as a benchmark. Three typical cases are studied. The first case (Case A) represents an ideal scenario where the complete freezing front contour is known (as could be the case in MRI or CT imaging) and when the acoustic shadow effect is ignored. The second case (Case B) is an extension of Case A when the acoustic shadow is taken into account (as could be the case in ultrasound imaging). Both cases A and B are solved using TFRM. The outcome from both cases for the specific conditions under investigation is an average mismatch of less than 1.5 mm in the lethal isotherm location. For the third case (Case C), the previously established unified framework was used to reconstruct the temperature field. The result of comparison with benchmark clearly showed an improvement in the accuracy of the predicted temperature values. Results from Case C show an improvement from 1.4 mm to 1.2 mm in average mismatch compared with the first two cases. Thus, the unified framework of TFRM and PFAM can be used effectively to reconstruct the temperature fields in 3D. A typical runtime for a TFRM solution in 3D was ~2000 seconds on an Intel® Quad Core™ i7 machine with 9 GB RAM, running at 3.07 GHz. While this is not real time, this study is a proof-of-concept and runtime optimizations are beyond the scope of this chapter.

Chapter 5: Characterization of a CMOS sensing core for ultra-miniature wireless implantable temperature sensors

The study described in this chapter is a part of an ongoing collaborated project guided by Professors Yoed Rabin and Jeyanandh Paramesh (ECE, CMU). The current chapter focuses on the development of ultra-miniature, wireless, implementable temperature sensors that can provide input temperature data in real time for the computation tools described in Chapters 2-4. Temperature sensor development presented in this chapter has been conducted by Mr. Ahmad Khairi (ECE, CMU) under the guidance of Prof. Paramesh [69, 42] (Sections 5.1-5.2) while system characterization in cryogenic temperatures has been conducted at the BTTL, under the guidance of Prof. Rabin (Section 5.3). The design, fabrication, and operation of the cryogenic experimentation stage have been conducted as a part of the current study and are described herein.

5.1 Principles of sensor design and implementation

The proposed temperature sensing unit consists of an integrated circuit, powered by electromagnetic induction and communicated with by Wi-Fi. The integrated sensing unit is expected to operate in the temperature range applicable to cryosurgery of -196°C to 37°C , while consuming power of less than $1\mu\text{W}$, which is deemed consistent with the potential to deliver power by induction. More specifically, the current study focuses on characterization of the temperature sensing core. The proposed temperature sensing core is presented here in brief for the completeness of presentation, while the detailed analysis of the proposed system is presented by Khairi et al. [42].

A schematic illustration of the proposed design for proportional-to-absolute-temperature (PTAT) sensor is displayed in Fig. 5.1, where Q_1 and Q_2 are nominally identical PNP bipolar junction transistors (BJTs), implemented using the substrate PNP structure inherent to standard CMOS technologies. The operational amplifier (op-amp; A_{DM} Fig. 5.1) forces the drain voltages of the metal-oxide semiconductor field-effect transistors (MOSFET) M_1 and M_2 to equate by means of negative feedback. By selecting the width of M_2 to equal n_0 times the width of M_1 , the drain current of M_2 becomes n_0 times the drain current of M_1 (annotated I_0). It follows that the difference between the emitter-base voltages V_{EB1} and V_{EB2} of transistors Q_1 and Q_2 , respectively, (Fig. 5.1) can be approximated as [70]:

$$\Delta V_{EB} = V_{EB2} - V_{EB1} = \phi_T \ln\left(\frac{n_0 I_0 I_S}{I_0 I_S}\right) = \phi_T \ln(n_0) \quad (5.1)$$

where

$$\phi_T = \frac{kT}{q} \quad (5.2)$$

and where I_S is the reverse saturation current of the BJT's, ϕ_T is the thermal voltage, k is the Boltzmann constant (1.381×10^{-23} J/K), q is the electronic charge (1.6×10^{-19} C), and T is the absolute temperature. Note that the current I_0 has a PTAT characteristic since it represents the ratio of ΔV_{EB} to R_B . The natural logarithm of the current ratio n_0 in Eq. (5.1) determines the constant of proportionality between the sensor's output voltage, ΔV_{EB} , and the absolute temperature.

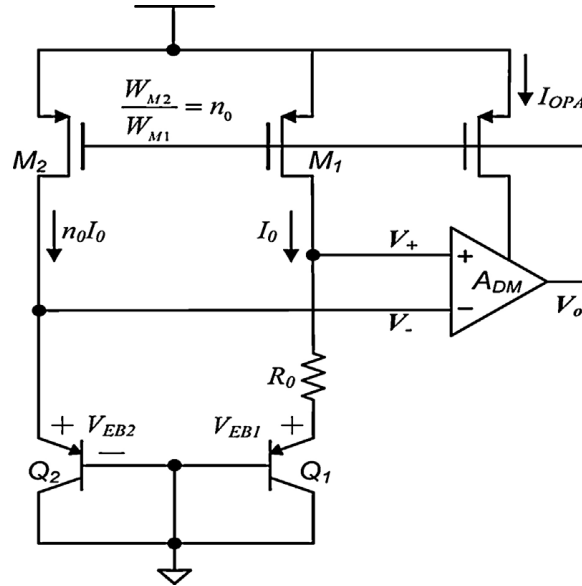


Figure. 5.1. Schematic illustration of the proposed proportional-to-absolute-temperature (PTAT) sensing core.

The primary advantage in a PTAT-based temperature sensor is that n_0 is nominally equal to the ratio of lithographically defined transistor widths, which is closely controlled in CMOS fabrication. While Eq. (5.1) provides insight into the operational principles of the temperature sensor, the model needs to be expanded to account for non-idealities which arise in a practical implementation, as described below.

5.2. Experimental setup

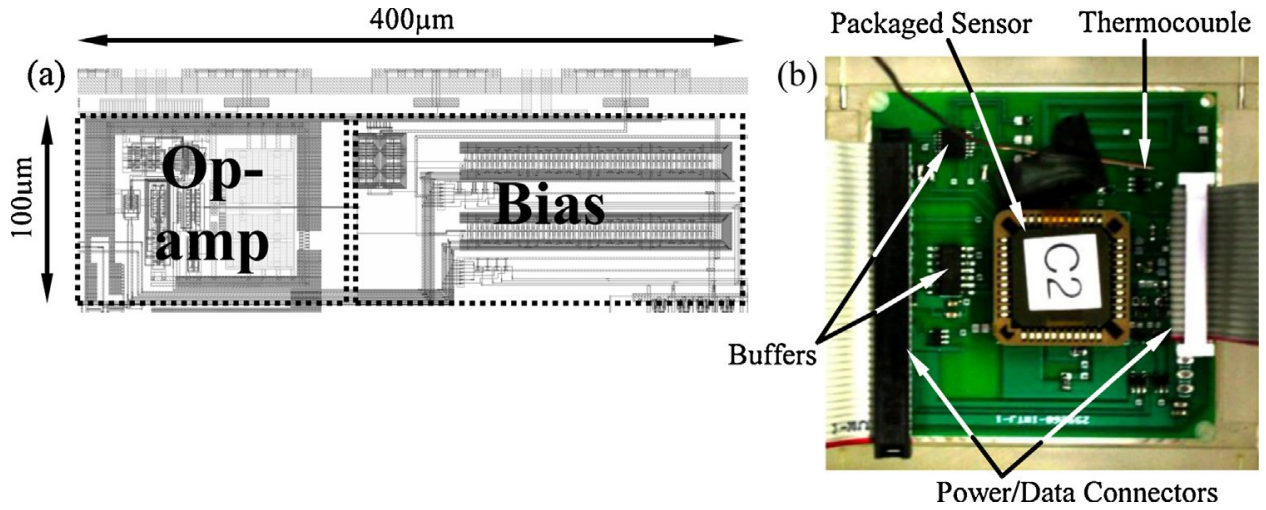


Figure. 5.2. Photograph of the fabricated sensor chip (a) and the packaged chip mounted on PCB (b).

Figure 5.2 displays a sensing core prototype, using a standard 130 nm CMOS process in a commercial foundry. The area occupied by the sensing core is $100\text{ }\mu\text{m} \times 400\text{ }\mu\text{m}$, which makes it an excellent candidate to be incorporated into an implantable sensor, and can be delivered into the body by means of a hypodermic needle. In its normal operational mode, the circuit is entirely self-biased, where the op-amp bias current is generated internally and is PTAT. The circuit can also be operated in a test mode using an external current source to provide the op-amp bias current, a case in which the bias current can be designed to have any desired dependency on temperature. Since only the sensing core of the wireless, implantable, temperature sensing device is under investigation in the current study, while wireless telemetry is the subject matter of a parallel study, the sensing core was hosted in a standard IC package. A custom printed circuit board (PCB) has been fabricated to characterize the chip. The sensor outputs, V_{EB1} and V_{EB2} , were buffered with amplifiers external to the chip (on the same PCB), in order to drive the loads of the measurement instruments. The sensor outputs were measured at a sampling rate of 0.2 Hz using a high accuracy Keithley 2400 Source Measure Unit.

5.3 Thermal design considerations of the experimental setup

Characterization of the sensor at cryogenic temperatures was performed in a controlled-rate cooler (Kryo 10–16 chamber and Kryo 10–20 controller, Planer Ltd., UK), as illustrated in Fig. 5.3. Cooling in the Kryo 10–16 chamber is achieved by circulating a mixture of nitrogen vapors and air at high velocity (up to 15 m/s). In order to protect the sensing core and the PCB board, a cryogenic holding stage was designed and constructed, as illustrated in Fig. 5.3(b). The holding stage is made of Plexiglas to avoid heat transfer from the stage to the sensing core. All side walls have holes to allow the highly turbulent air to flow through the insides of both parts of the stage. The packaged sensor shown in Fig. 5.2 is in direct contact with the circulating nitrogen vapors mixture. Thus design of the holding stage along with the highly turbulent flow ensures thermal equilibrium between nitrogen vapor stream and the sensing core. Once the system is packaged and miniaturized, the need for the current setup for sensing unit characterization will change to enable wireless communication with a transmitter/receiver strategically placed adjacent to the sensing unit. The temperature sensor was benchmarked against temperature measurements obtained with a T-type thermocouple, placed on the PCB next to the chip, in continuous data logging mode (OMB DAQ-56, Omega Engineering, Inc.). Data acquisition for the thermocouple and the new sensor was done concurrently and independently.

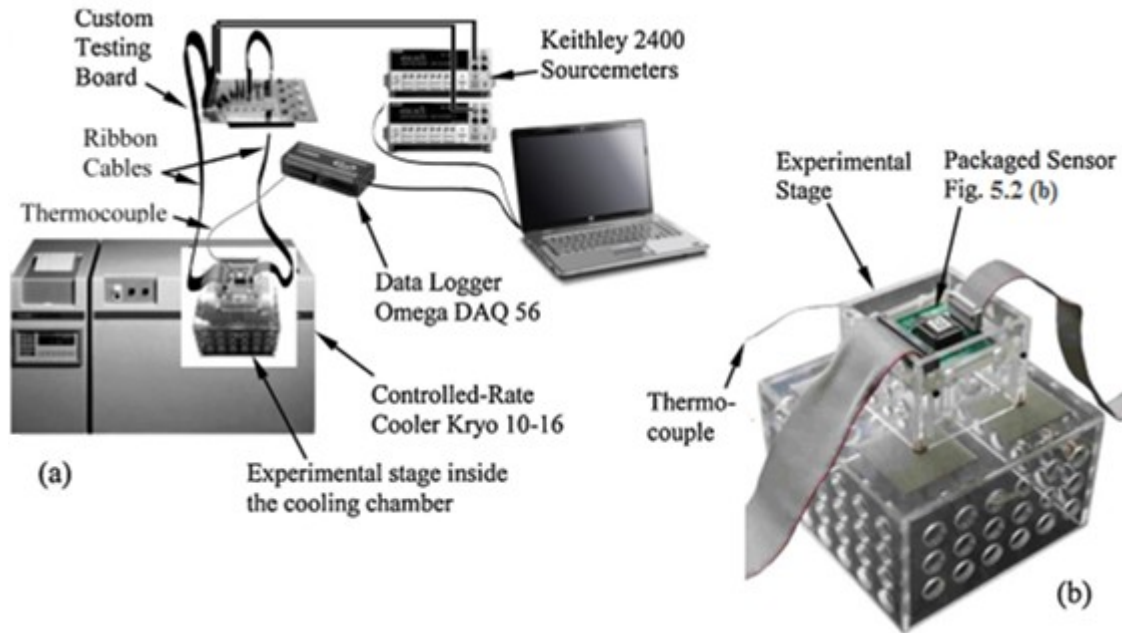


Figure. 5.3. Experimental setup: (a) a schematic illustration of the system, and (b) a photograph of the experimental stage.

5.4 Results and discussion

Figure 5.4 displays results obtained with two specimens of the sensing core at a sampling rate of 0.2 Hz; both specimens were fabricated on the same wafer. The thermal protocol included a sequence of cooling ramps, separated apart by constant-temperature holding periods, which were long enough to let the system reach steady state at each temperature level. Each temperature data point in Fig. 5.4 represents an average and standard deviation of 30 consecutive readings at steady state in order to reduce uncertainties in measurements.

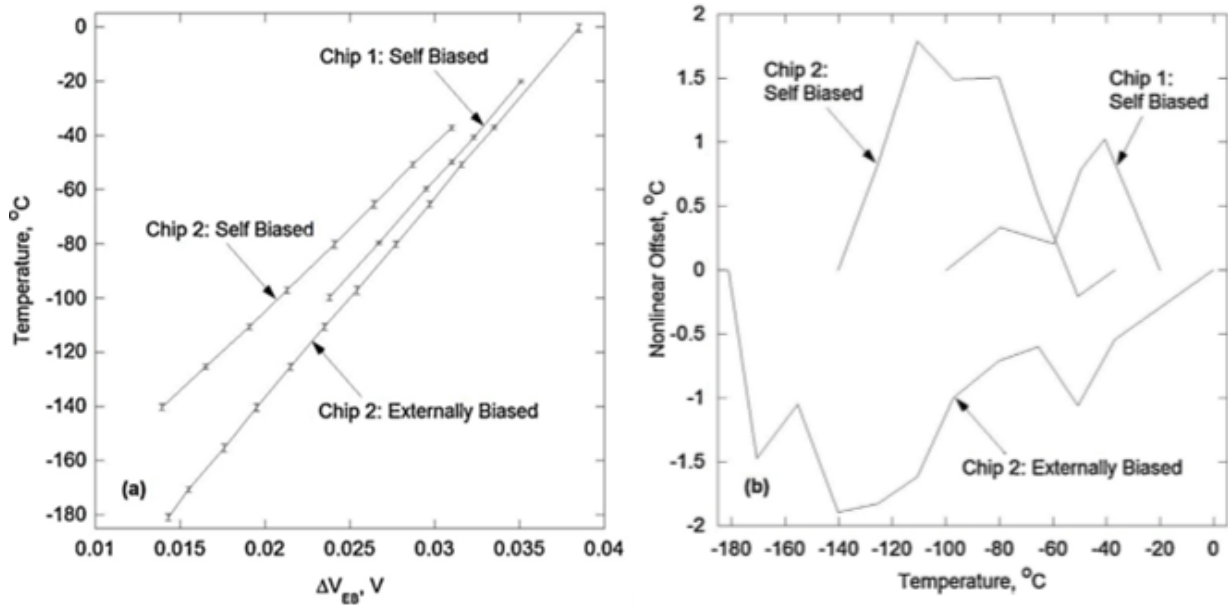


Figure. 5.4. Results obtained from three representative chips in a self-biased mode (#1 and #2) and an externally biased mode (#2): (a) temperature data as a function of voltage output, and (b) average nonlinear offset, calculated as the temperature difference between the experimental data shown (a) and a linear curve connecting the boundary temperature values for each dataset.

Experimental results demonstrate a very high linearity of the sensor output with temperature in a range of -180°C and -20°C , with maximum observed nonlinearity of 2°C of full scale (1.1%). While potential sources for nonlinearity in the proposed design have been discussed [69] no nonlinearity mitigation techniques were deemed necessary for cryosurgery applications. Reducing nonlinear effects would unnecessarily increase the power overhead associated with the corresponding mitigation mechanisms. The uncertainty range, defined by twice the standard deviation (2σ) at steady state, was found to vary with temperature, but to not exceeding 1.4°C in

all studied cases. While this range is deemed adequate for cryosurgery application, it is higher than that predicted, based on computerized design tools[69]. This difference can be partly attributed to:

- (1) Temperature variations inside the cooling chamber, where its temperature is controlled by periodic ejection of liquid nitrogen into a highly turbulent airstream;
- (2) Uncertainty in reference temperature, where the reference thermocouple is specified to have an uncertainty range of 1.4°C at -100°C ; and,
- (3) Electronic noises in off-chip buffer, cables, and multi-meter, which may be eliminated in a wireless implementation.

5.5 Summary

In this chapter, a remote sensing core of a proposed wireless miniature temperature sensor was presented. The remote sensing core was characterized in BTTL using the cryo-chamber of a commercially available controlled-rate cooler. A Plexiglas holding stage was designed and fabricated in-house. The stage designed in such a way that temperature gradient across the board were held to a minimum. This in conjunction with highly turbulent nitrogen vapor flow ensured thermal equilibrium between the airflow and core.

The observed uncertainty range was higher than modeled because of the highly turbulent airstream, reference temperature uncertainty and electronic noise. However, in the ultimate application, the heat transfer problem will be dominated by heat conduction, while the highly turbulent airflow and electronic noises will be absent. This means that the uncertainty in the designed implementation will be lower than the data presented in this chapter.

Chapter 6: Summary and Conclusions

The ultimate goal of cryosurgery is to maximize tissue destruction in the targeted region while minimizing injury to the adjacent healthy tissue. To achieve this goal, clinicians and cryosurgical device manufacturers have designed increasingly smaller cryoprobe. These small cryoprobes enable a large number of cryoprobes to be used simultaneously, which can provide a higher degree of control over the freezing process. However, due to the large number of cryoprobes involved, the complexity of the procedure has increased accordingly. The outcome of the cryoprocure is thus highly dependent on the skills and experience of the clinician.

The work presented in this thesis is a part of ongoing research at the Biothermal Technology Laboratory to develop hardware and computational tools to provide capabilities to monitor the developing temperature field in real-time. While prostate cryosurgery is used as a developmental model in the current project, the numerical methods developed in this work can be easily extended to other forms of cryosurgery.

This study investigates the potential contribution of data from three different sources for temperature-field reconstruction: implantable sensors, cryoprobe-embedded sensors, and freezing front location extracted from medical imaging. This data is used as input when solving the inverse heat transfer problem in prostate cryosurgery. A key modeling assumption for temperature-field reconstruction is that the cryosurgical process can be treated as quasi-steady, while the transient nature of the process comes about through transient boundary conditions. These transient boundary conditions are measured temperatures at the tip of cryoprobes, temperature measured by embedded sensors, and the moving freezing front extracted from medical imaging. The justification for this assumption is that Stefan number is small in a typical cryosurgery problem, which means that the cryosurgery heat transfer problem is dominated by latent heat effects. The quasi-steady approximation approach transforms the ill-posed inverse mathematical problem of bioheat transfer to a well-posed problem having a unique solution.

In chapter 2, quasi-steady approximation was used to develop a numerical method to reconstruct the temperature field during cryosurgery (TFRM). TFRM was implemented using the commercial code MATLAB in 2D. For benchmarking purposes, ANSYS was used to solve the transient 2D bioheat transfer problem of during cryosurgery. The layout of the cryoprobes used in the simulation was selected using a proprietary planning algorithm termed “bubble-packing technique”. A typical execution of TFRM in 2D using MATLAB was in the range of 2 to 3 s on

an Intel® Quad Core™ i7 machine with 9 GB RAM, running at 3.07 GHz, indicating the ability to attain near-real time performance.

Emphasis in temperature-field analysis was given to the location of the so-called lethal temperature (-45°C), which is of a clinical significance but typically not presented to the cryosurgeon in real time. When compared the benchmark solution, results indicate that TFRM can provide a good approximation for the location of the lethal temperature in many scenarios. The average mismatch when full freezing front location is assumed to be known using a medical imaging technique is less than 1 mm. This mismatch value for the lethal temperature isotherm location is comparable with the uncertainty inherent to medical imaging. When only partial of the freezing front location was assumed to be known, the average mismatch increased to 1.4 mm. This analysis also address sensors placement along the organ contour and along the predicted location of the isotherms: 0°C , -22°C , and -45°C . Further sensitivity analysis and strategies for sensor placement were investigated. Combining image analysis in real time with data from cryoprobe-embedded temperature sensors can provide an alternative approach to temperature-field reconstruction in real time. Thus, TFRM provides the means for real-time monitoring of developing temperature fields during cryosurgery.

Modern cryosurgery relies on Trans-Rectal Ultrasound Transducer (TRUST) to monitor the developing freezing front. The primary challenge in ultrasound monitoring of cryosurgery is the high absorption of the ultrasound energy by the frozen region, which leads to (i) opacity of the frozen region on the ultrasound monitor, (ii) shadow effect behind the frozen region, and (iii) clear demarcation of the freezing front in areas close to the ultrasound transducer. In Chapter 3, Potential Field Analogy Method (PFAM) was developed to approximate the location of the freezing front in areas invisible to US imaging. The technique is based on US image analysis as input, while it does not rely on the development of additional sensors or specialized instrumentation making use of currently available hardware used in the process.

PFAM represents a complete alternative approach to the previous numerical method, TFRM. The main advantage of TFRM is its ability to incorporate information from multiple sensing modalities (temperature sensors, medical imaging) while the main advantage of PFAM is very low computational cost and the lack of need for temperature sensors. TFRM was benchmarked initially against full-scale numerical simulations and then against experimental data, while PFAM was benchmarked alone only against experimental data. At an advanced stage, PFAM

was further integrated with TFRM to estimate the temperature distribution within the frozen region.

Results of the study indicate that PFAM is a viable and computationally inexpensive technique for estimating the location of freezing front in the acoustic shadow. Comparison of PFAM estimations and experimental data showed an average mismatch of less than 2 mm in freezing-front location, which is comparable with the uncertainty in ultrasound imaging. Comparison of the hybrid PFAM+TFRM method with full-scale finite elements analysis (FEA) indicates an average mismatch of 0.9 mm for the freezing front location, $T=0^{\circ}\text{C}$, and 0.1 mm for the lethal temperature isotherm, $T=-45^{\circ}\text{C}$. Comparison of the hybrid method with experimental temperature measurements show a difference in the range of 2°C and 6°C for the selected points of measurement. It can be concluded that the hybrid method is adequate to estimate the location of the freezing front, the location of the lethal temperature isotherm, and the temperature distribution in a clinical setup. Furthermore, given the associated computer runtime of 0.5 s for PFAM and 3.5 s for the hybrid method, and given the lack of cost-effective alternatives, the hybrid PFAM + TFRM approach suggests a very promising approach towards real-time monitoring during cryosurgery.

In Chapter 4, PFAM, TFRM and the hybrid PFAM + TFRM were extended from 2D to 3D. This represented a large increase in computational cost and complexity. ANSYS was again used to solve a full 3D transient bioheat transfer simulation of a cryosurgical procedure and create a benchmark for comparison. The layout of the cryoprobes was decided using 'bubble packing technique'. The average mismatch for all the considered cases using TFRM and the hybrid method was less than 2 mm. One such example is at $t = 180$ s, when the location of the freezing front is known partially at a single cross section ($z = 35$ mm), the maximum mismatch is 5.6 mm and the average mismatch is 1.4 mm. However, when PFAM is used in integrated with TFRM, the maximum mismatch reduces to 5.3 mm and the average mismatch reduces to 1.2 mm. This conclusively shows the ability of PFAM to improve the predicted temperature fields inside the target region. Similar results are also observed for other considered cases. While this study demonstrates a proof-of-concept only, the hybrid method appears to be a viable solution for the problem of reconstructing the temperatures inside the tissue. While the above runtime results were obtained using MATLAB and general-purpose subroutines, it is possible to dramatically decrease the computation time by GPU-based computation in a C++ environment.

In Chapter 5, a contribution to the development of miniature implantable sensors is overviewed, which could potentially provide input data for the numerical methods proposed in Chapters 2-4. The study presented in Chapter 5 focuses on an innovative temperature sensing core, which is one component of a three-components sensing unit, where the other two components are related to powering the sensing unit and wireless communication with it. This experimental project represents a collaborated effort between the labs of Professors Paramesh and Rabin, where the unique contribution in the current study is in the development and operation of a thermal testing stage for cryogenic temperatures. Experimental results on the temperature sensing core demonstrated a linear relationship between the temperature and sensor output in the range of -180°C and 0°C . The uncertainty in temperature measurement was found to be variable but not exceeding 1.4°C . The causes of this uncertainty were found to be highly turbulent airflow in the cryo-chamber, uncertainty in the reference temperature measurement and electronic noise. However, the sensing core in its final implementation is meant to be embedded inside the tissue. Thus, only mode of heat transfer is conduction inside the tissue. The major cause of noise is thus absent which will lead to much lower uncertainties for the sensing core.

As cryosurgical devices and techniques continue to move forward, the complexity associated with the procedure will increase. Managing this increase in complexity requires incorporation of real-time monitoring tools if minimally invasive cryosurgery is to remain a preferred treatment option. The work presented in thesis is a proof-of-concept in 2D and 3D, incorporating medical imaging and temperature sensors and appears to be beneficial for clinical application.

Chapter 7: Future Work

In this chapter, a few possible directions for future work are highlighted. The work presented in this thesis demonstrated the feasibility of real-time temperature reconstruction during cryosurgery. Real-time monitoring has a high potential to increase the quality of cryosurgical outcomes. Thus, it is likely to be highly advantageous to further develop the unified numerical framework and deploy it in a clinical setting.

7.1 Porting MATLAB code to C/C++

The numerical methods presented in this thesis are implemented in MATLAB. The decision to develop the model in MATLAB was taken because it is an excellent tool for performing rapid testing of models and algorithms. MATLAB is also mainly designed for help in solving linear systems of equations. This ensured that the model development proceeded in a rapid fashion. However, MATLAB is slow compared to other languages such as C, C++, Julia or RUST. Real time temperature reconstruction using TFRM + PFAM in 2D using MATLAB takes only a few seconds giving near real-time performance. However, when PFAM + TFRM is used in 3D case, it takes around 2000 seconds. In order to make sure that real time temperature reconstruction is feasible for 3D, it is imperative that the MATLAB code be ported to one of the higher performance compiled languages.

C++ would be a good option considering its long history and wide support it enjoys in the numerical computation community. C++ does not have a native linear algebra library. However, third party linear algebra libraries such as Armadillo, Boost, Eigen, LAPACK++ etc. all provide full support for wide range of linear algebra operations. Porting to C++ would also make it easy for the mathematical model to be implemented on a Graphics Processing Unit (GPU) platform.

7.2 Ultrasound Imaging

The numerical method presented here makes use of ultrasound imaging as one of the inputs. Ultrasound imaging is the most preferred imaging technique for minimally invasive cryosurgical procedures, primarily due to low cost and high availability. As the freezing front develops, the frozen tissue appears bright due to high reflectivity of sound waves. This also means that the shadow region behind the freezing front is very dark. This fact clearly illustrate in Fig.7.1 below.

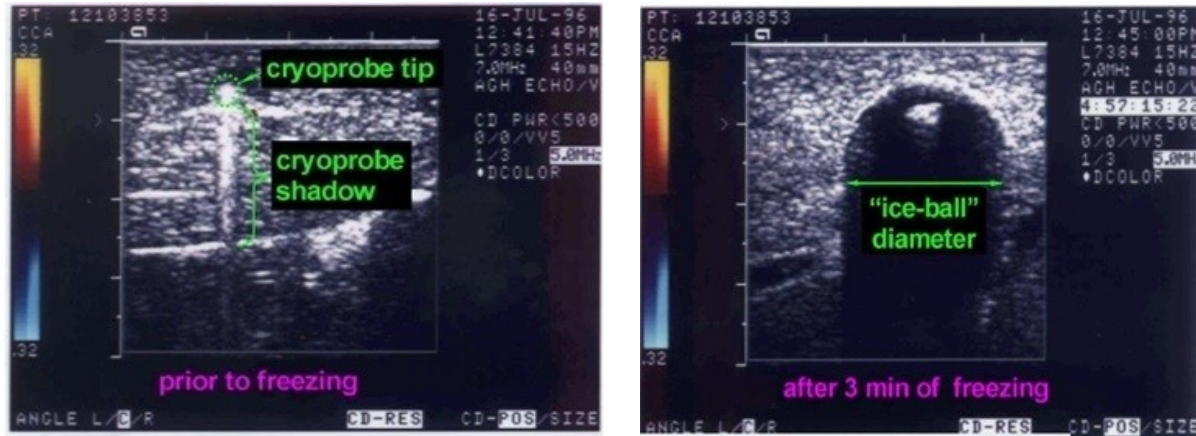


Figure 7.1: The figure shows an ultrasound snapshot of tissue before and after onset of freezing [courtesy of Prof. Yoed Rabin]

Ultrasound images generally use the Digital Imaging Communication in Medicine (DICOM) standard for storing and exchanging of images and related information. The DICOM standard can be thought of as having several levels of support, such as the support for image exchange for both senders and receivers, the underlying information model and information management services. Thus using the protocols specified in the DICOM standard, a sub-routine to parse the US image in real time would have to be developed. The parsed image would be mapped to the volume to tissue being treated and used as input for the established unified framework.

7.3 Optimization of Potential Field Analogy Method

As described in Chapter 3, one of the assumptions made about PFAM is that the cryoprobes in the procedure being modeled are identical in behavior. This is a good first order approximation as shown by the experimental verification performed on 2D sections. However, in actual procedure, the cryoprobes may have behavior distinct from each other. This might impact the performance PFAM especially when used in 3D cases. The effect of variable cryoprobe behavior needs to be explored using numerical simulations.

7.4 Experimental Validation in 3D

In Chapter3, a 2D experimental validation of numerical methods (TFRM, PFAM and Hybrid method) is presented. While the results of this validation are promising, a full-scale 3D

validation of the framework would be far more applicable in the context of real-world clinical practice. The 2D study presented in this thesis only validated planning on a single prostate cross-section. Commercially available three-dimensional prostate phantom models are used for the purpose of training cryosurgeons. Such a model could be used for validation purposes.

7.5 Sensor Placement Strategies

An initial study on sensor-placement strategies is presented in Chapter 2. Results of this study indicate that reconstructed temperature field is sensitive to the location of the sensors. To better formulate sensor placement strategies, the distribution of cancer tumors in the prostate could serve as a guide. It has been observed that 68% of cancer tumors are found in the peripheral zone of the prostate, which correlates with about 70% of prostate total volume [71]. Peripheral-zone cancer tumors typically tend to grow along the nerve branches [71]. Therefore, emphasis in sensors placement can be paid to those areas of high likelihood of tumor growth, in order to ensure that their temperatures are below the lethal temperature (-45°C). Furthermore, the likelihood of cancer developing in the urethral wall is low, while the temperature distribution between the urethral wall and its surrounding cryoprobes is fairly easy to predict [16]. Thus, sensors in the area surrounding the urethra are of low priority.

Additional parameters which may affect the sensors placement are the contour of the target region shape, and the expected location of strategically targeted isotherms, such as the lethal isotherm and the freezing front. Denser sensors distribution may be chosen in areas of critical significance to prevent cryoinjury. Finally, it was concluded in Chapter 2 that the mismatch between the benchmark and the reconstructed temperature field is higher in areas with steep temperature gradients. A strategy which analyzes the temperature gradient field and place higher weight on areas of significant changes could decrease the overall number of sensors to be used while preserving the quality of the solution.

LIST OF PUBLICATION

1. Thaokar, C., & Rabin, Y. (2011, June). Temperature field reconstruction for the application of wireless implantable temperature sensors in cryosurgery. In *ASME 2011 Summer Bioengineering Conference* (pp. 41-42). American Society of Mechanical Engineers.
2. Rabin, Y., Paramesh, J., Fedder, G., Khairi, A., Thaokar, C. (2011): Developing new means for thermal therapy monitoring and control: a miniature wireless implantable temperature sensor and a temperature-field reconstruction technique. Society for Thermal Medicine Annual Meeting, New Orleans, LA (April 29-May 2)
3. Rabin, Y., Paramesh, J., Fedder, G., Khairi, A., Thaokar, C. (2011): Developing means to improve cryosurgery monitoring: a miniature wireless implantable temperature sensor and a temperature-field reconstruction technique. CRYO2011-the 48th Annual Meeting of the Society for Cryobiology, Corvallis, OR. *Cryobiology* 63(3):315
4. Thaokar, C., & Rabin, Y. (2012). Temperature field reconstruction for minimally invasive cryosurgery with application to wireless implantable temperature sensors and/or medical imaging. *Cryobiology*, 65(3), 270-277
5. Rabin, Y., Feig, J. S., Williams, A. C., Lin, C. C., & Thaokar, C. (2012, June). Cryomacroscopy in 3D: a device prototype for the study of cryopreservation. In *ASME 2012 Summer Bioengineering Conference* (pp. 27-28). American Society of Mechanical Engineers
6. Thaokar, C. V., & Rabin, Y. (2012, March). Temperature-field reconstruction for the application of prostate cryosurgery. In *Bioengineering Conference (NEBEC), 2012 38th Annual Northeast* (pp. 73-74). IEEE.
7. Thaokar, C., & Rabin, Y. (2013): Temperature-field reconstruction in 3D for minimally invasive cryosurgery based on medical imaging and/or wireless implantable temperature sensors. CRYO2013-the 50th Annual Meeting of the Society for Cryobiology, N. Bethesda, DC (July 28-31). *Cryobiology*, 67(3):426 (Student Award)
8. Khairi, A., Thaokar, C., Fedder, G., Paramesh, J., & Rabin, Y. (2014). Characterization of a CMOS sensing core for ultra-miniature wireless implantable temperature sensors with application to cryomedicine. *Medical engineering & physics*, 36(9), 1191-1196.

9. Thaokar, C., Rossi, M. R., & Rabin, Y. (2015). A new method for temperature-field reconstruction during ultrasound-monitored cryosurgery using potential-field analogy. *Cryobiology*, *in press*, DOI:10.1016/j.cryobiol.2015.10.153

REFERENCES

- [1] J. Arnott, "Practical illustrations of the remedial efficacy of a very low or anaesthetic temperature," *Lancet*, vol. 2, pp. 257-259, 1850.
- [2] L. Cailletet, "Recherches sur la liquefaction des gaz," *Ann Chimie Physique*, vol. 15, pp. 132-144, 1878.
- [3] A. C. White, "Liquid air: its application in medicine and surgery," *Med. Rec.*, vol. 56, pp. 109-112, 1899.
- [4] H. G. Irvine and D. D. Turnacliffe, "Liquid oxygen in dermatology," *Archives of Dermatology and Syphilology*, vol. 19, no. 2, pp. 270-280, 1929.
- [5] T. Fay, "Early experiences with local and generalized refrigeration of the human brain," *J. Neurosurg*, vol. 16, pp. 239-260, 1959.
- [6] I. Cooper and A. Lee, "Cryostatic congelation: A system for producing a limited controlled region of cooling or freezing of biological tissue," *Journal of Nervous & Mental Disease*, vol. 133, pp. 259-263, 1961.
- [7] G. Onik, J. Gilbert, W. Hoddick, R. Filly, P. Callen, B. Rubinsky and L. Farrel, "Sonographic monitoring of hepatic cryosurgery in an experimental animal model," *AJR American Journal of Roentgenology*, vol. 144, no. 5, pp. 1043-1047, 1985.
- [8] G. Onik, C. Cobb, J. Cohen, J. Zabkar and B. Porterfield, "US characteristics of frozen prostate," *Radiology*, vol. 168, no. 3, pp. 629-631, 1988.
- [9] J. G. Baust and Z. Chang, "Underlying mechanisms of damage and new concepts in cryosurgical instrumentation," in *Cryosurgery: Mechanism and Applications*, Paris, International Institute of Refrigeration, 1995, pp. 21-36.
- [10] Z. Chang, J. J. Finkelstein, H. Ma and J. Baust, "Development of a high-performance multiprobe cryosurgical device," *Biomedical instrumentation & technology*, vol. 28, no. 5, pp. 383-390, 1993.
- [11] K. R. Han, J. K. Cohen, R. J. Miller, A. J. Pantuck, D. G. Freitas, C. A. Cuevas, H. L. Kim, J. Lugg, S. J. Childs, B. Shuman, M. A. Jayson, N. D. Shore, Y. Moore, A. Zisman, J. Y. Lee, R. Ugarte, L. A. Mynderse, T. M. Wilson, S. D. Sweat, H. Zincke and A. S. Belldegrun, "Treatment of organ defined prostate cancer with third generation cryosurgery: preliminary multicenter experience," *The Journal of Urology*, vol. 170, pp. 1126-1130, 2003.

- [12] J. D. Schmidt, "Transperineal Ultrasound-Guided Prostate Cryosurgery," *Journal of surgical oncology*, vol. 65, no. 3, pp. 228-229, 1997.
- [13] G. M. Onik, J. K. Cohen, G. D. Reyes, B. Rubinsky, Z. H. Chang and J. Baust, "Transrectal ultrasound-guided percutaneous radical cryosurgical ablation of the prostate," *Cancer*, vol. 72, no. 4, pp. 1291-1299, 1993.
- [14] W. F. Whitmore III, W. E. Barzell and R. F. Wilson, "Sterile disposable template grid system". US Patent 6036632, 14 March 2000.
- [15] M. R. Rossi and Y. Rabin, "Experimental verification of numerical simulations of cryosurgery with application to computerized planning," *Physics in Medicine and Biology*, vol. 52, pp. 4553-4567, 2007.
- [16] Y. Rabin and T. F. Stahovich, "The thermal effect of urethral warming during cryosurgery," *CryoLetters*, vol. 23, no. 6, pp. 361-374, 2002.
- [17] R. D. Cespedes, L. L. Pisters, A. C. von Eschenbach and E. J. McGuire, "Long-term followup of incontinence and obstruction after salvage cryosurgical ablation of the prostate: results in 143 patients," *The Journal of urology*, vol. 157, no. 1, pp. 237-240, 1997.
- [18] J. K. Cohen, R. J. Miller and B. A. Shuman, "Urethral warming catheter for use during cryoablation of the prostate," *Urology*, vol. 45, no. 5, pp. 861-864, 1995.
- [19] J. C. Gilbert, B. Rubinsky, S. Wong, G. R. Pease, P. P. Leung and K. M. Brennan, "Temperature determination in the frozen region during cryosurgery in rabbit liver using MR image analysis," *Magnetic Resonance Imaging*, vol. 15, no. 6, pp. 657-667, 1997.
- [20] B. Rubinsky, J. C. Gilbert, G. M. Onik, M. S. Roos, S. Wong and K. M. Brennan, "Monitoring cryosurgery in the brain and the prostate with proton NMR," *Cryobiology*, vol. 30, pp. 191-199, 1993.
- [21] G. A. Sandison, M. P. Loye, J. C. Rewcastle, J. C. Hahn, J. C. Saliken, J. G. McKinnon and B. J. Donnelly, "X-ray CT monitoring of ice-ball growth and thermal distribution during cryosurgery," *Physics in medicine and biology*, vol. 43, no. 11, p. 3309, 1998.
- [22] G. M. Onik, "Image Guided Prostate Cryosurgery: State of the Art," *Cancer Control: Journal of the Moffit Cancer Center*, vol. 8, no. 6, pp. 522-531, 2001.
- [23] A. A. Gage and J. G. Baust, "Cryosurgery-a review of recent advances and current issues," *CryoLetters*, vol. 23, no. 2, pp. 69-78, 2002.

- [24] A. A. Gage and J. Baust, "Mechanics of tissue injury in cryosurgery," *Cryobiology*, vol. 37, pp. 171-186, 1998.
- [25] D. Tanaka, K. Shimada and Y. Rabin, "Two-phase computerized planning of cryosurgery using bubble-packing and force-field analogy," *ASME Journal of Biomechanical Engineering*, vol. 128, no. 1, pp. 49-58, 2006.
- [26] D. Tanaka, K. Shimada, M. R. Rossi and Y. Rabin, "Cryosurgery planning using bubble packing in 3D," *Computer Methods in Biomechanics and Biomedical Engineering*, vol. 11, no. 2, pp. 113-121, 2008.
- [27] A. Sehrawat, R. Keelan, D. M. Wilfong, J. T. McCormick and Y. Rabin, "Simulation-based cryosurgery intelligent tutoring system (ITS) prototype," *Technology in Cancer Research and Treatment*, p. in press, 2015.
- [28] J. G. Baust, A. A. Gage, D. Klossner, D. Clarke, R. Miller, J. Cohen, A. Katz, T. Polascik, H. Clarke and J. M. Baust, "Issues critical to the successful application of cryosurgical ablation of the prostate," *Technology in Cancer Research and Treatment*, vol. 6, no. 2, pp. 97-109, 2007.
- [29] American Urological Association, "Best Practice Policy Statement on Cryosurgery for the Treatment of Localized Prostate," [Online]. Available: www.auanet.org. [Accessed 15 1 2012].
- [30] A. A. Gage, "Cryosurgery in the treatment of cancer," *Surgery, Gynecology & Obstetrics*, vol. 174, pp. 73-92, 1992.
- [31] B. Rubinsky, "Annual Review of Biomedical Engineering," *Cryosurgery*, vol. 2, pp. 157-187, 2000.
- [32] J. C. Saliken, B. J. Donnelly, P. Brasher, N. Ali-Ridha, S. Ernst and J. Robinson, "Outcome and Safety of Transrectal US-guided Percutaneous Cryotherapy for Localized Prostate Cancer," *Journal of Vascular and Interventional Radiology*, vol. 10, no. 2, pp. 199-208, 1999.
- [33] W. S. Wong, D. O. Chinn, M. Chinn, J. Chinn and W. L. Tom, "Cryosurgery as a Treatment for Prostate Carcinoma," *Cancer*, vol. 79, no. 5, pp. 963-974, 1997.
- [34] C. Thaokar and Y. Rabin, "Temperature field reconstruction for the application of wireless implantable temperature sensors in cryosurgery," *Cryobiology*, vol. 65, no. 3, pp. 270-277, 2012.

- [35] Y. Rabin and A. Shitzer, "Combined solution to the inverse Stefan problem for successive freezing/thawing in non-ideal biological tissues," *ASME Journal of Biochemical Engineering*, vol. 119, no. 2, pp. 146-152, 1997.
- [36] Y. Rabin and A. Shitzer, "Exact solution to the one dimensional inverse stefan problem in non-ideal biological tissues," *ASME Journal of Heat Transfer*, vol. 117, no. 2, pp. 425-431, 1995.
- [37] J. Hadamard, *Lectures on Cauchy's Problem in Linear Differential Equations*, New Haven, CT: Yale University Press, 1923.
- [38] M. Alifanov, *Inverse Heat Transfer Problems*, New York: Springer-Verlag, 1994.
- [39] N. Ozisik, *Inverse Heat Transfer*, CRC Press, 2000.
- [40] J. Hou, S. Abudayyeh and Y. Shaib, "Treatment of chronic radiation proctitis with cryoablation," *Gastrointestinal endoscopy*, vol. 73, no. 2, pp. 383-389, 2011.
- [41] B. Han and J. C. Bischof, "Effect of thermal properties on heat transfer in cryopreservation and cryosurgery," *ASME 2002 International Mechanical Engineering Congress and Exposition*, pp. 7-15, January 2002.
- [42] A. Khairi, S. C. Hung, J. Paramesh, G. Fedder and Y. Rabin, "Ultra-miniature wireless temperature sensor for thermal medicine applications. Energy-based Treatment of Tissue and Assessment VI," in *SPIE – BiOS 2011*, San Francisco, CA, USA, January 22-27, 2011.
- [43] J. C. Saliken, J. G. McKinnon and R. Gray, "CT for monitoring cryotherapy," *American Journal of Roentgenology*, vol. 166, pp. 853-855, 1996.
- [44] H. H. Pennes, "Analysis of tissue and arterial blood temperature in the resting human forearm," *Journal of Applied Physiology*, vol. 1, pp. 93-122, 1948.
- [45] V. R. Voller, "A heat balance integral based on the enthalpy formulation," *International Journal of Heat and Mass Transfer*, vol. 30, pp. 604-606, 1986.
- [46] Y. Rabin and A. Shitzer, "Numerical solution of the multidimensional freezing problem during cryosurgery," *ASME Journal of Biomechanical Engineering*, vol. 120, no. 1, pp. 32-37, 1998.
- [47] K. C. Charny, "Mathematical models of bioheat transfer," 1992.
- [48] K. R. Diller, "Modeling of bioheat transfer processes at high and low temperatures,"

Advances in Heat Transfer, pp. 157-358, 1992.

- [49] Y. Rabin, "A general model for the propagation of uncertainty in measurements into heat transfer simulations and its application to cryobiology," *Cryobiology*, vol. 46, no. 2, pp. 109-120, 2003.
- [50] R. Keelan, K. Shimada and Y. Rabin, "Developing a framework for computerized training of cryosurgery based on finite elements analysis," in *ASME 2011 Summer Bioengineering Conference - SBC 2011*, Farmington, PA, Jun 22-25, 2011.
- [51] M. R. Rossi, D. Tanaka, K. Shimada and Y. Rabin, "An efficient numerical technique for bioheat simulations and its applications to cryosurgery planning," *Computer Methods and Programs in Biomedicine*, vol. 85, no. 1, pp. 41-50, 2006.
- [52] Y. Rabin, R. Coleman, D. Mordohovich, R. Ber and A. Shitzer, "A new cryosurgical device for controlled freezing , Part II: in vivo experiments on rabbits' hind thighs," *Cryobiology*, vol. 33, pp. 93-105, 1996.
- [53] M. R. Rossi, D. Tanaka, K. Shimada and Y. Rabin, "Computerized planning of cryosurgery using bubble packing: an experimental validation on a phantom material," *The International Journal of Heat and Mass transfer*, vol. 51, pp. 5671-5678, 2008.
- [54] M. R. Rossi and Y. Rabin, "Analysis of a numerical scheme for bioheat simulations of cryosurgery and its experimental validation on a phantom material," in *MSV'07- The 2007 International Conference on Modeling, Simulation and Visualization Methods*, Las Vegas, Nevada, USA, June 25-28, 2007.
- [55] Y. H. Lee, *Introduction to Engineering Electromagnetics*, Springer, 2013.
- [56] Y. Rabin, D. C. Lung and T. F. Stahovich, "Computerized planning of cryosurgery using cryoprobes and cryoheaters," *Technology in Cancer Research and Treatment*, vol. 3, no. 3, pp. 229-243, 2004.
- [57] R. Pohle and K. Toennis, "Segmentation of medical images using adaptive region growing," *Proceedings of SPIE Medical Imaging*, vol. 4322, pp. 1337-1346, 2001.
- [58] Y. L. Chang and X. Li, "Adaptive image region growing," *IEEE Transactions on Image Processing*, vol. 3, no. 6, pp. 868-872, 1994.
- [59] J. Serra, *Image Analysis and Mathematical Morphology*, London: Academic Press, 1982.
- [60] V. Chalana and Y. Kim, "A methodology for evaluation of boundary detection algorithms

- on medical images," *IEEE Transactions of Medical Imaging*, vol. 16, no. 5, pp. 642-652, 1997.
- [61] E. Belogay, C. Molter and R. Shonkwiler, "Calculating the Hausdorff distance between curves," *Information Processing Letters*, vol. 64, no. 1, pp. 17-22, 1997.
- [62] D. P. Huttonlochar, G. A. Klanderman and W. J. Rucklidge, "Comparing Images Using the Hausdorff Distance," *IEEE Transactions on Pattern Analysis and Machine Intelligence*, vol. 15, no. 9, pp. 850-863, 1993.
- [63] G. Rote, "Computing the minimum Hausdorff distance between two point sets on a line under translation," *Information Processing Letters*, vol. 38, pp. 123-127, 1991.
- [64] M. Dubuisson and A. K. Jain, "A Modified Hausdorff Distance for Object Matching," in *Proceedings of International Conference on Pattern Recognition*, Jerusalem, 1994.
- [65] T. Furuhashi, I. Song, Y. Rabin and K. Shimada, "Interactive prostate shape reconstruction from 3D TRUS images," *Journal of Computation Design and Engineering*, vol. 1, no. 4, pp. 272-288, 2014.
- [66] R. Keelan, H. Zhang, K. Shimada and Y. Rabin, "GPU-based bioheat simulation to facilitate rapid decision making associated with cryosurgery training," *Technology in Cancer Research and Treatment*, p. in press, 2015.
- [67] "Sparse matrix wiki," [Online]. Available: https://en.wikipedia.org/wiki/Sparse_matrix. [Accessed 12 09 2015].
- [68] M. Inc, "mldivide," [Online]. Available: <http://www.mathworks.com/help/matlab/ref/mldivide.html>. [Accessed 12 10 2015].
- [69] A. Khairi, C. Thaokar, G. Fedder, J. Paramesh and Y. Rabin, "Characterization of a CMOS sensing core for ultra-miniature wireless implantable temperature sensors with application to cryomedicine," *Medical Engineering and Physics*, vol. 36, no. 9, pp. 1191-1196, 2014.
- [70] B. Razavi, Design of analog CMOS integrated circuits, New York: McGraw-Hill, 2001.
- [71] A. Sehrawat, K. Shimada and Y. Rabin, "Generating prostate models by means of geometric deformation for the application of computerized training of cryosurgery," *International Journal of Computer Assisted Radiology and Surgery*, vol. 8, no. 2, pp. 301-312, 2012.
- [72] D. Tanaka, M. R. Rossi, K. Shimada and Y. Rabin, "Towards intra-operative computerized

- planning of prostate cryosurgery," *The International Journal of Medical Robotics and Computer Assisted Surgery*, vol. 3, pp. 10-19, 2007.
- [73] D. Tanaka, K. Shimada, M. R. Rossi and Y. Rabin, "Computerized planning of prostate cryosurgery with pullback procedure," *Computer Aided Surgery*, vol. 13, no. 1, pp. 1-13, 2008.
- [74] Y. C. Shih, T. Shen and B. P. Otis, "A 2.3 micro-W wireless intraocular pressure/temperature monitor," *IEEE Solid-State Circuits*, vol. 46, no. 11, pp. 2592-601, 2011.
- [75] Y. Rabin, "Imaging of breast cryosurgery," in *Atlas of cryosurgery*, Vienna, Springer-Verlag, 2001, pp. 344-53.
- [76] Y. Rabin, J. Paramesh, G. Fedder, A. Khairi and C. Thaokar, "Developing new means for thermal therapy monitoring and control: a miniature wireless implantable temperature sensor and a temperature-field reconstruction technique," in *Society for Thermal Medicine Annual Meeting*, New Orleans, LA, April 29 - May 2, 2011.
- [77] Y. Rabin and E. Korin, "An efficient numerical solution for the multidimensional solidification (or melting) problem using a microcomputer," *International Journal of Heat and Mass Transfer*, vol. 36, no. 3, pp. 673-683, 1993.
- [78] W. A. Pusey, "The use of carbon dioxide snow in the treatment of nevi and other lesions of the skin," *Journal of the American Medical Association*, vol. 49, no. 16, pp. 1354-1356, 1907.
- [79] G. R. Pease, S. T. Wong, M. S. Roos and B. Rubinsky, "MR image-guided control of cryosurgery," *Journal of Magnetic Resonance Imaging*, vol. 5, pp. 753-60, 1995.
- [80] R. Matsumoto, K. Oshio and F. A. Jolesz, "Monitoring of laser- and freezing-induced ablation in the liver with T1-weighted MR imaging," *Journal of Magnetic Resonance Imaging*, vol. 2, pp. 555-62, 1992.
- [81] S. Cytron, A. Paz, S. Kravchick, D. Shumalinski and J. Moore, "Active Rectal Wall Protection Using Direct Transperineal Cryo-Needles for Histologically Proven Prostate Adenocarcinomas," *European Urology*, vol. 44, pp. 315-321, 2003.
- [82] J. G. Baust and A. A. Gage, "The Molecular Basis of Cryosurgery," *BJU international*, vol. 95, no. 9, pp. 1187-1191, 2005.
- [83] C. Thaokar, M. R. Rossi and Y. Rabin, "A new method for temperature-field reconstruction

- during ultrasound-monitored cryosurgery using potential-field analogy," *Cryobiology*, p. in press, 2015.
- [84] Y. C. Shih, T. Shen and B. P. Otis, "A 2.3 microW wireless intraocular pressure/temperature monitor," *IEEE Journal of Solid-State Circuits*, vol. 46, no. 11, pp. 2592-2601, 2011.
- [85] A. Khairi, S.-C. Hung, J. Paramesh, G. Fedder and Y. Rabin, "Ultra-miniature wireless temperature sensor for thermal medicine applications," in *SPIE-BIOS*, San Francisco, 2011 (Jan 22-27).
- [86] V. Chalasani, L. Gardi, C. H. Martinez, D. B. Downey, A. Fenster and J. Chin, "Contemporary technique of intraoperative 3-dimensional ultrasonography-guided transperineal prostate cryotherapy," *Canadian Urological Association Journal*, vol. 3, no. 2, pp. 136-141, 2009.
- [87] A. Fenster, J. Bax, H. Neshat, D. Cool, N. Kakani and C. Romagnoli, "3D ultrasound imaging in image-guided intervention," *36th Annual International Conference of the IEEE*, pp. 6151-6154, August 2014.